10-31-2014

# Analysis of Advanced Supercritical Carbon Dioxide Power Cycles for Concentrated Solar Power Applications

Saeb Mostaghim Besarati
*University of South Florida*, sbesarati@mail.usf.edu

# Analysis of Advanced Supercritical Carbon Dioxide Power Cycles for Concentrated Solar Power Applications

by

Saeb M. Besarati

A dissertation submitted in partial fulfillment
of the requirements for the degree of
Doctor of Philosophy
Department of Chemical and Biomedical Engineering
College of Engineering
University of South Florida

Co-Major Professor: D. Yogi Goswami, Ph.D.
Co-Major Professor: Elias K. Stefanakos, Ph.D.
Venkat R. Bhethanabotla, Ph.D.
Babu Joseph, Ph.D.
George P. Philippidis, Ph.D.

Date of Approval:
October 31, 2014

Keywords: Thermodynamic Cycles, Central Receiver, Solar Field, Compact Heat Exchangers, Optimization

## DEDICATION

I dedicate this dissertation to my parents, wife, and sister for their love, endless support, and encouragement.

**ACKNOWLEDGMENTS**

I would like to thank my advisor Dr. D. Yogi Goswami, who gave me insight into the field of solar energy engineering and provided me with the opportunity to acquire knowledge and skills that I believe will benefit my future career endeavors. I would also like to thank Dr. Elias Stefanakos for his valued suggestions through my studies. He was always present to help me when I needed assistance.

I would like to thank my friends in Clean Energy Research Center (CERC), Ricardo Vasquez Padilla, Gokmen Demirkaya, Huijuan Chen, Chennan Li, Philip Myers, Jamie Trahan, Yanyang Zhang , Tanvir Alam, Abhinav Bhardwajh, Chatura Wickramaratne and Rajeev Kamal. I would like especially to thank Antiono Ramos, and Mehdi Zeyghami. I am also grateful to Mr. Charles Garretson, Mrs. Barbara Graham, and Mrs. Ginny Cosmides who helped me in the course of my stay in CERC.

I would like to give my special thanks to my parents and sister for their unconditional support throughout my life. Last but not the least, I would like to acknowledge my wife, Forough, for her patience, understanding and encouragement throughout my studies.

**TABLE OF CONTENTS**

## LIST OF TABLES

## LIST OF FIGURES

## ABSTRACT

Solar power tower technology can achieve higher temperatures than the most common commercial technology using parabolic troughs. In order to take advantage of higher temperatures, new power cycles are needed for generating power at higher efficiencies. Supercritical carbon dioxide (S-$CO_2$) power cycle is one of the alternatives that have been proposed for the future concentrated solar power (CSP) plants due to its high efficiency. On the other hand, carbon dioxide can also be a replacement for current heat transfer fluids (HTFs), i.e. oil, molten salt, and steam. The main disadvantages of the current HTFs are maximum operating temperature limit, required freeze protection units, and complex control systems. However, the main challenge about utilizing s-$CO_2$ as the HTF is to design a receiver that can operate at high operating pressure (about 20 MPa) while maintaining excellent thermal performance. The existing tubular and windowed receivers are not suitable for this application; therefore, an innovative design is required to provide appropriate performance as well as mechanical strength.

This research investigates the application of s-$CO_2$ in solar power tower plants. First, a computationally efficient method is developed for designing the heliostat field in a solar power tower plant. Then, an innovative numerical approach is introduced to distribute the heat flux uniformly on the receiver surface. Next, different power cycles utilizing s-$CO_2$ as the working fluid are analyzed. It is shown that including an appropriate bottoming cycle can further increase the power cycle efficiency. In the next step, a thermal receiver is designed based on compact heat exchanger (CHE) technology utilizing s-$CO_2$ as the HTF. Finally, a 3$MW_{th}$ cavity receiver is

designed using the CHE receivers as individual panels receiving solar flux from the heliostat field. Convective and radiative heat transfer models are employed to calculate bulk fluid and surface temperatures. The receiver efficiency is obtained as 80%, which can be further improved by optimizing the geometry of the cavity.

# CHAPTER 1 INTRODUCTION

The world demand for energy has continuously increased over the last century in step with the industrial development and population growth. The International Energy Agency (IEA) projects the global energy demand to grow by more than one-third by 2035, with China, India and Middle East accounting for 60% of the increase [1]. Presently, 80% of the world's energy is supplied by fossil fuels including coal, oil, and natural gas, which are non-renewable resources [2]. Since the fossil fuel resources are finite, they will eventually run out.

In addition, burning fossil fuels releases carbon dioxide, which is mainly responsible for global warming. According to the National Oceanic and Atmosphere administration, the concentration of $CO_2$ in the atmosphere in May 2013 reached a daily average of 400 parts per million (ppm), the highest level for at least 800,000 years [3]. The limited sources of fossil fuels and environmental concerns associated with burning fossil fuels have necessitated a greater effort in transforming the present energy systems to a more sustainable basis.

Of all the renewable energy resources which are directly or indirectly derived from the sun (except geothermal energy), solar energy is expected to have a significant contribution to the world's energy supply in the future. Figure 1-1 shows the current and projected global energy mix based on the analysis carried out by German Advisory Council on Global Change (WBGU) [4]. As can be seen from the figure, it is expected that solar energy will begin to increase its share in the future and rapidly become the primary world energy source by the end of the century. By 2100, fossil fuels and nuclear will supply below 15% of world's energy needs while solar energy will provide about 70%.

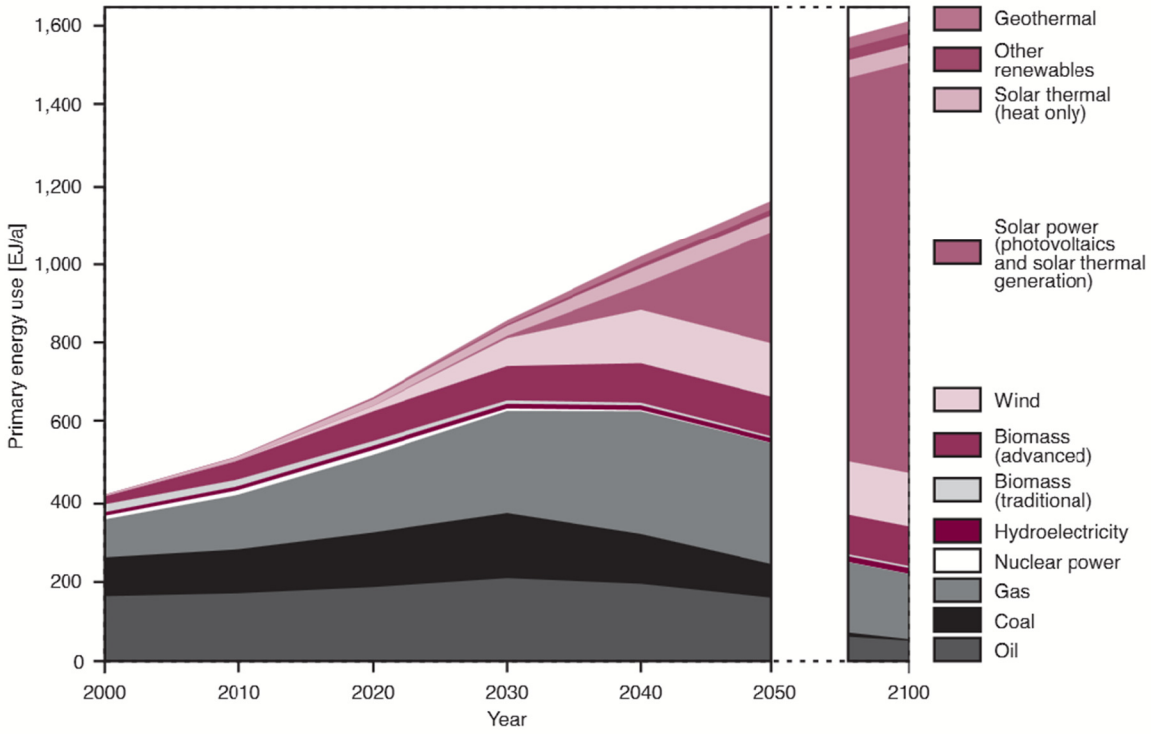


Figure 1-1 Current and projected global energy mix [4]

Solar energy can be converted into electricity using photovoltaic (PV) panels or thermal power plants. PV panels deploy semi-conductor technology to convert sunlight directly into electricity. On the other hand, solar thermal power plants use reflective mirrors to concentrate sunlight and convert the sun's energy into heat. Then, the generated heat is utilized to run a power cycle which produces electricity. Advantages of solar thermal over PV technology can be summarized as:

(1) Solar thermal technology can be integrated with conventional thermal power plants.

(2) Thermal storage is more cost-effective and viable compared with electrochemical storage using batteries.

(3) Solar thermal power plants can reach higher solar to electric efficiencies.

(4) The heat generated by solar thermal power plants can also be utilized as process heat.

There are four technologies that are currently employed in solar thermal power plants: Power Tower or Central Receiver, Parabolic Trough, Linear Fresnel, and Parabolic Dish.

### 1.1 Power Tower (Central Receiver)

In power tower technology (Figure 1-2), the sun's rays are reflected and concentrated by a number of mirrors that are collectively called the heliostat field. The concentrated rays are focused onto a receiver, which is mounted on the top of a tower. The receiver plays the role of a heat exchanger, where the thermal energy is transferred to a working fluid. After transporting the heat to a thermal storage tank, if the thermal storage unit exists, the same or a secondary working fluid is used to run a turbine to produce power. Central receivers can achieve temperatures of the order of 1000°C; therefore, a central receiver concentrator is suitable for thermal electric production in the range of 10-1000 MW.

Figure 1-2 Aerial view of Gemasolar power plant [5]

### 1.2 Parabolic Trough

This technology employs parabolic trough-shaped reflectors to concentrate direct solar radiation onto a receiver tube which is located in the focal line of the parabola. The typical operating temperature is 150-400°C. The collectors rotate around one axis to track the sun from east to west

Figure 1-3 Parabolic trough solar collectors [6]

and continuously provide energy to heat the HTF inside the receiver. After gaining heat, the HTF goes through a series of heat exchangers and transfers heat to the working fluid in the power cycle. Figure 1-3 depicts parabolic trough collectors in a solar thermal power plant.

**1.3 Linear Fresnel**

Similar to parabolic trough collectors, linear Fresnel is a line-focusing technology. However, instead of parabolic-shaped reflectors, a series of long flat or slightly curved ground-mounted mirrors are employed.

Figure 1-4 Linear Fresnel mirrors at the Plataforma Solar de Almeria, Spain [7]

The main advantage of linear Fresnel over parabolic trough is the lower cost associated with the construction of the mirrors and the receiver. On the other hand, the maximum operating temperature is lower, which results in lower solar to electricity conversion efficiency in comparison with parabolic trough technology. Figure 1-4 depicts linear Fresnel mirrors at the Plataforma Solar de Almeria.

### 1.4 Parabolic Dish

Parabolic dish concentrator is a point-focusing technology, which consists of a two axes tracking parabolic dish that reflects and concentrates the normal insolation onto a receiver (Figure 1-5). The advantages of this technology can be summarized as high efficiency, modularity, autonomous operation and inherent hybrid capability [8] while the main disadvantage is high capital and maintenance costs [9].

Figure 1-5 Parabolic dish concentrators [7]

### 1.5 Comparison Among the Technologies

Figure 1-6 depicts the operational solar thermal power plants in the world by country and technology as of March 2011. As can be seen, a majority of the power plants, i.e. 96.3%, use parabolic trough technology to convert solar energy into heat. Most of these power plants are located

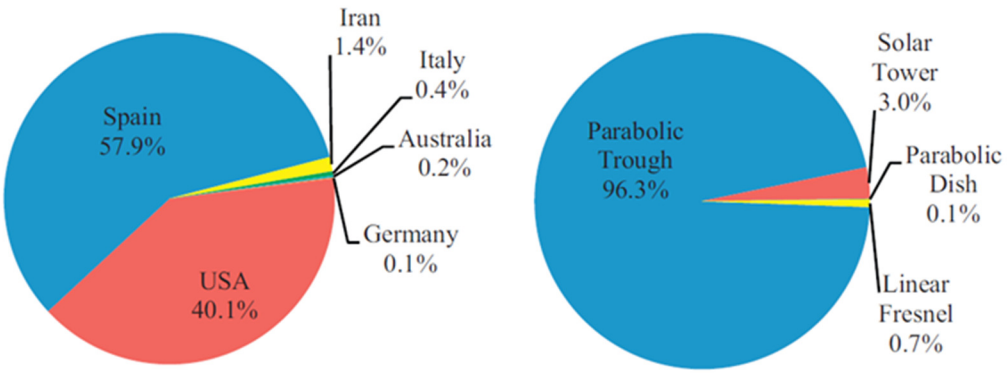


Figure 1-6 Worldwide operational solar thermal power plants (March 2011). Left: installed power by country. Right: installed power by technology [10]

in Spain and USA. On the other hand, there has been a surge of interest in developing solar tower type power plants over the last few years. Such interest is mainly associated with the ability to achieve high operating temperatures, resulting in greater solar to electric efficiency. Table 1-1 compares different key parameters among the CSP technologies [11]. Although the relative cost of solar tower is still high, its outlook of improvement is very significant. Parabolic dish also performs very efficiently, but the relative cost is still very high and not competitive with other technologies.

Several solar tower projects have been initiated and completed over the last few years including Ivanpah Solar Electric Generating System, the largest solar thermal power plant in the world. The power plant is located in California, and the gross capacity is planned as 392 megawatts

Table 1-1 Comparison among different solar technologies (adapted from [11])

| | Relative cost | Land occupancy | Thermodynamic efficiency | Solar concentration ratio | Outlook for improvements |
|---|---|---|---|---|---|
| Parabolic trough | Low | Large | Low | 15-45 | Limited |
| Linear Fresnel | Very low | Medium | Low | 10-40 | Significant |
| Solar tower | High | Medium | High | 150-1500 | Very significant |
| Parabolic dish | Very high | Small | High | 100-1000 | High potential through mass production |

Figure 1-7 A solar power tower plant in California, Mojave Desert [12]

(MW). It employs 173,500 mirrors to concentrate sunlight, and water is used as the heat transfer fluid.

### 1.6 Principles of Solar Tower Power Plants

Figure 1-7 shows the Solar Two power plant in California. Three main components of the plant are a heliostat field, receiver, and power block. Thermal energy storage can extend the power production beyond the sunshine hours. Schematic of the Solar Two plant is also shown in Figure 1-8.

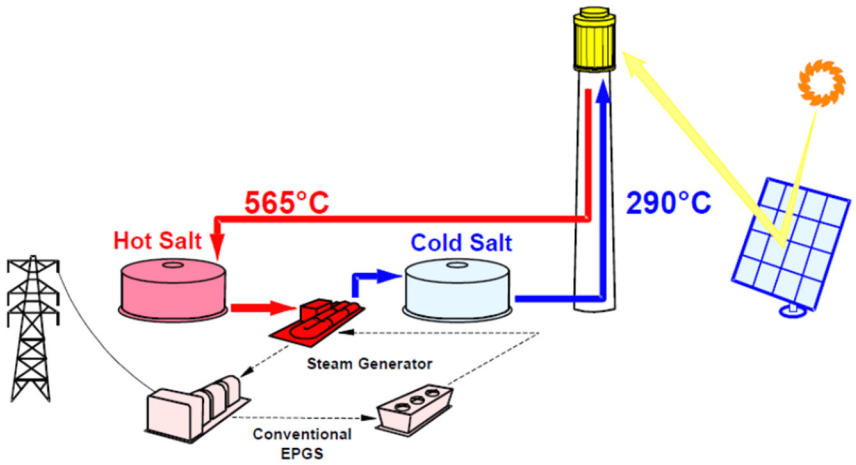


Figure 1-8 Schematic of the Solar Two Power Plant [13]

The heliostats reflect solar radiation onto the receiver where the thermal energy is transferred to the heat transfer fluid, i.e. molten salt. Two tank thermal storage is used in this power plant. The hot molten salt goes through the heat exchangers where it transfers heat to pressurized water to generate steam. The cold molten salt leaving the heat exchanger enters the cold tank before gaining heat in the receiver. The generated steam runs a steam turbine and produces power.

Although solar tower technology seems very promising because of the high temperatures that can be achieved, the associated cost is still high and is not competitive with fossil fuels. Figure 1-9 depicts the cost breakdown of PS10, 11 $MW_e$ power tower plant that is located near Seville, Spain. In this power plant, 624 heliostats are used to reflect and concentrate solar radiation onto the top of a 115 meter tower where the water is directly heated, and steam is generated.

As can be seen from the figure, almost 42% of the cost is associated with the heliostat field. Therefore, reducing the cost of the heliostats can have a profound effect on the levelized cost of electricity (LCOE). Moreover, close to 40% of the energy received from the sun is usually lost

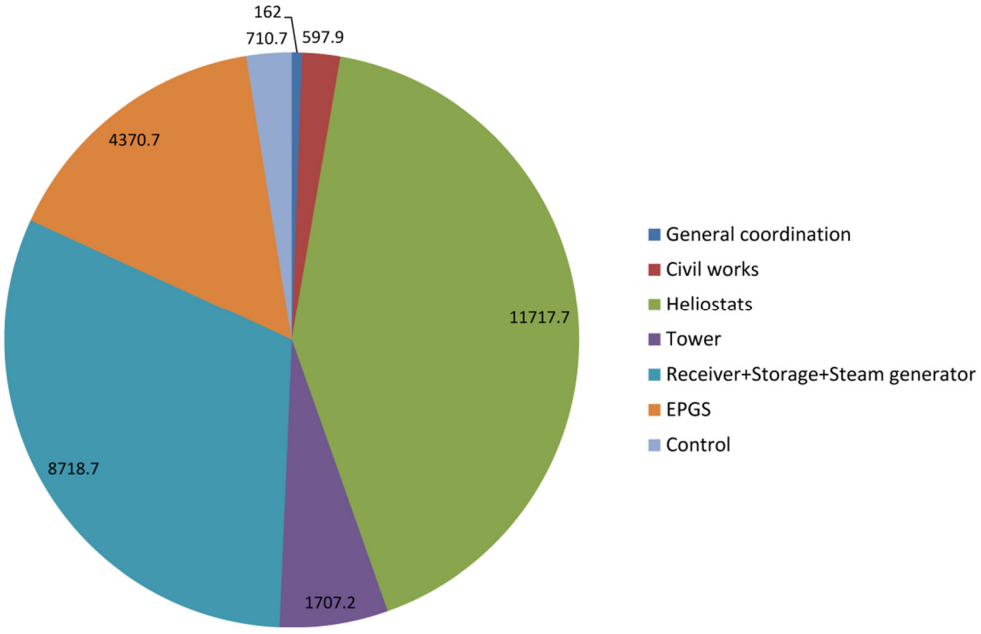


Figure 1-9 Cost breakdown of PS10 power tower plant (number are given in thousand $) [14]

before reaching the receiver [15]. Therefore, increasing the optical efficiency of the field and designing an efficient solar field is of great importance.

Turchi et al. [16] carried out a comprehensive analysis on predicting the future price of molten salt solar power tower in the U.S market. The main factors that can alleviate the cost were summarized as: Reducing the cost of the heliostats, increasing the operating temperature and employing more efficient power cycles, and including thermal storage with the systems to increase the capacity factor. By taking all these factors into consideration, the LCOE of this technology is expected to drop to 10-13 cents/kWh over the next ten years (Figure 1-10), and it becomes competitive with natural gas combined cycle systems. In Figure 1-10, the capacity factors less than 30% represent the power plants without storage.

In an attempt to make CSP price competitive with conventional power, the U.S. Department of Energy (DOE) announced an initiative that aimed at reducing the total costs and reaching the target cost of 6 cents/kWh by 2020. Besides revolutionary improvements in numerous aspects of the

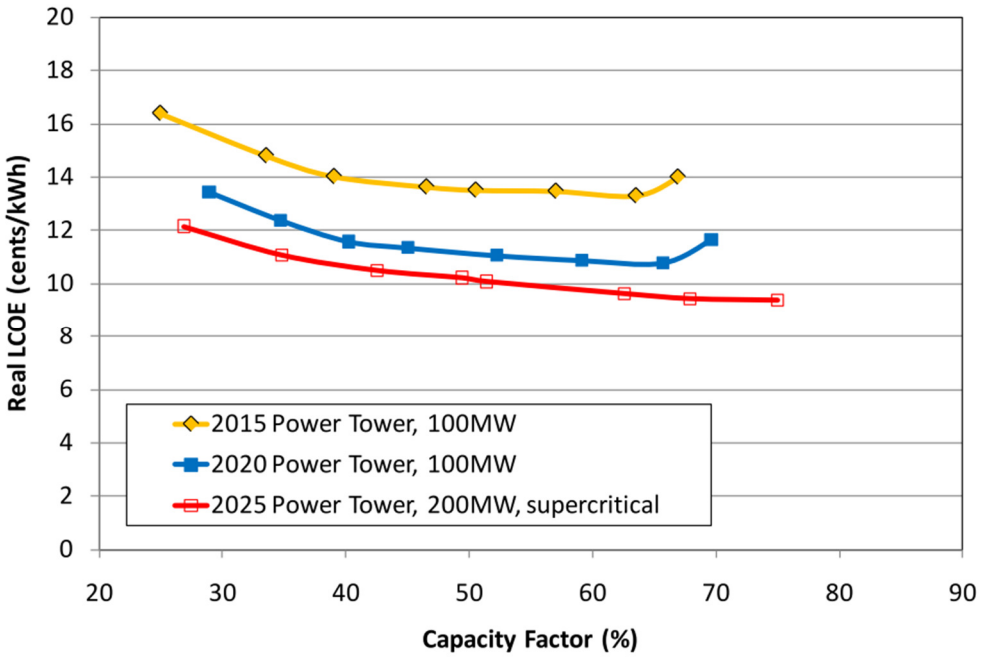


Figure 1-10 Future cost of molten salt solar tower system in the U.S market [16]

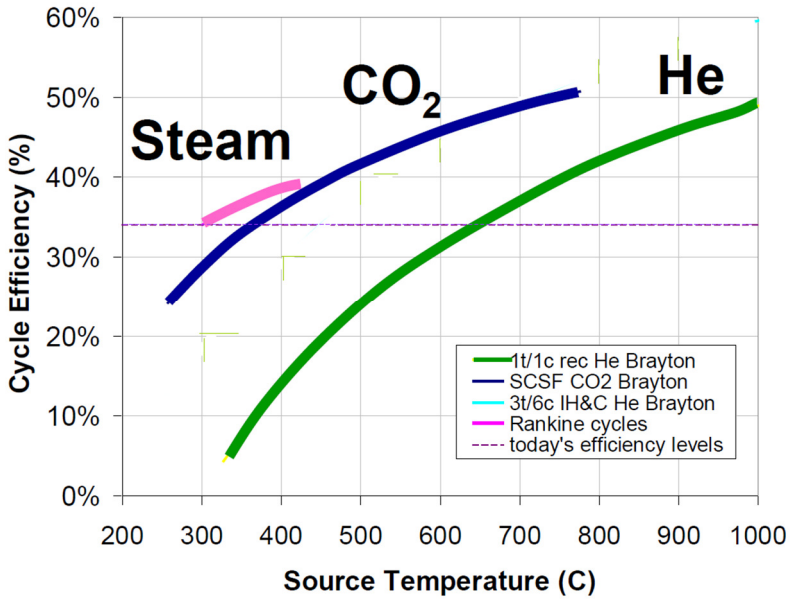


Figure 1-11 Thermal efficiency of different power cycles [17]

solar power tower plants, new generations of power cycles are required to generate power at higher efficiencies, and lower costs compared with conventional steam cycles in order to meet this target. Supercritical carbon dioxide (S-$CO_2$) power cycle is one of the alternatives that have been proposed for the future CSP plants.

Figure 1-11 compares the performance of the s-$CO_2$ cycle with the steam Rankine and helium Brayton cycles [17]. As can be seen, s-$CO_2$ cycle has efficiency benefit over steam when the heat source temperature is greater than 420℃. In addition, the s-$CO_2$ cycle can reach 50% efficiency at a much lower heat source temperature compared to helium. The high efficiency of the cycle is due to low compression work, as the density of $CO_2$ increases substantially around the critical point. The density of $CO_2$ around the critical point is comparable with the liquids, which requires low pumping power.

On the other hand, higher density of the working fluid means smaller power conversion components. Figure 1-12 compares the size of a s-$CO_2$ turbine with a helium and a steam turbine.

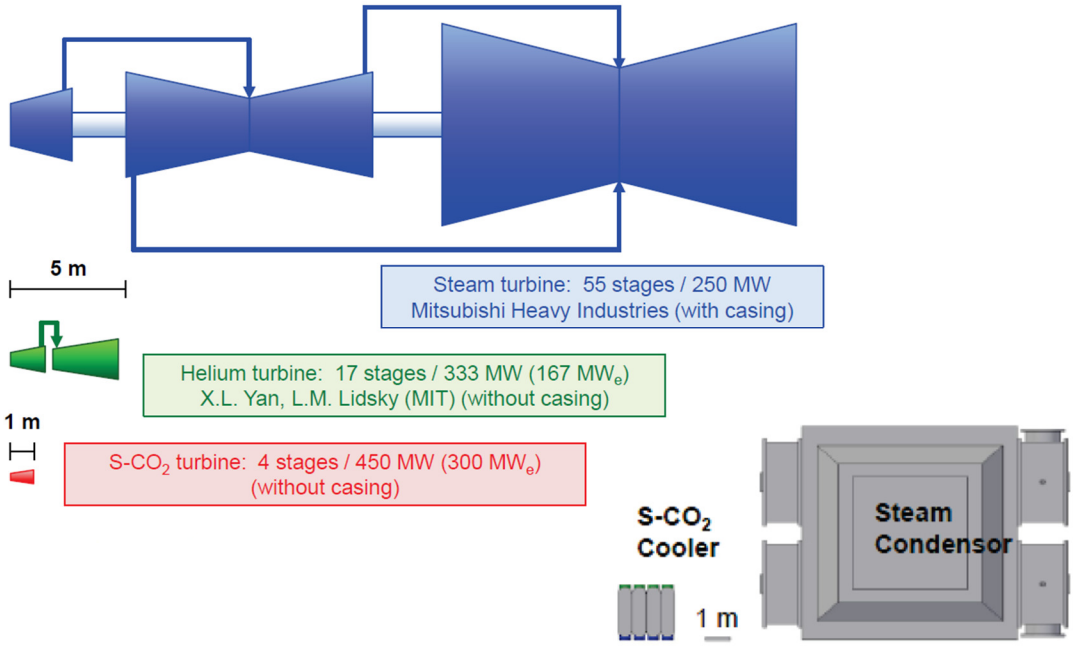


Figure 1-12 Relative size of the components in s-$CO_2$, helium and steam power cycles [17] [18]

The size of a s-$CO_2$ cooler and a steam condenser are also compared in this figure. As can be clearly seen, the sizes of the components of the s-$CO_2$ cycle are much smaller than the other cycles.

Figure 1-13 compares the critical properties of a number of fluids that are used in the power cycles. According to the figure, carbon dioxide has moderate critical properties which make it adaptable to most source and sink temperatures. Therefore, the s-$CO_2$ power cycle can be utilized in fossil fuel, CSP, geothermal, and nuclear power plants.

Figure 1-14 shows the ranges of operating temperature for each of these power plants and the efficiencies that can be obtained using s-$CO_2$ cycle. According to the figure, in CSP plants efficiencies in the range of 43% to 54% are obtainable under wet cooling conditions. However, CSP plants are usually located in the areas where water resources are limited; therefore, dry cooling may be preferred over wet cooling. Under dry cooling conditions, close to 50% efficiency is still achievable, which is consistent with the framework of the DOE SunShot program.

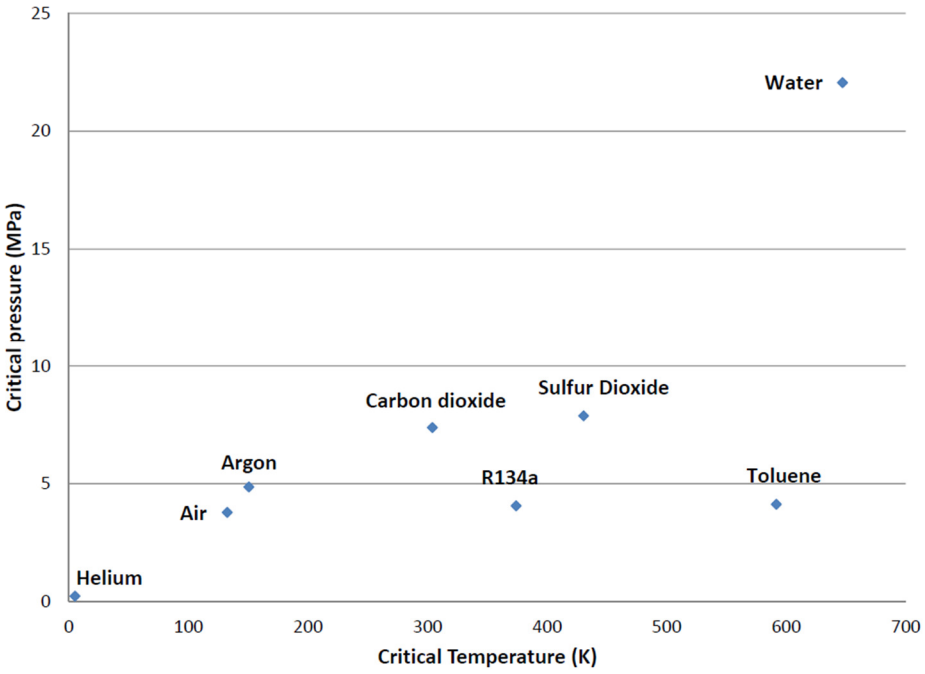


Figure 1-13 Critical properties of some fluids

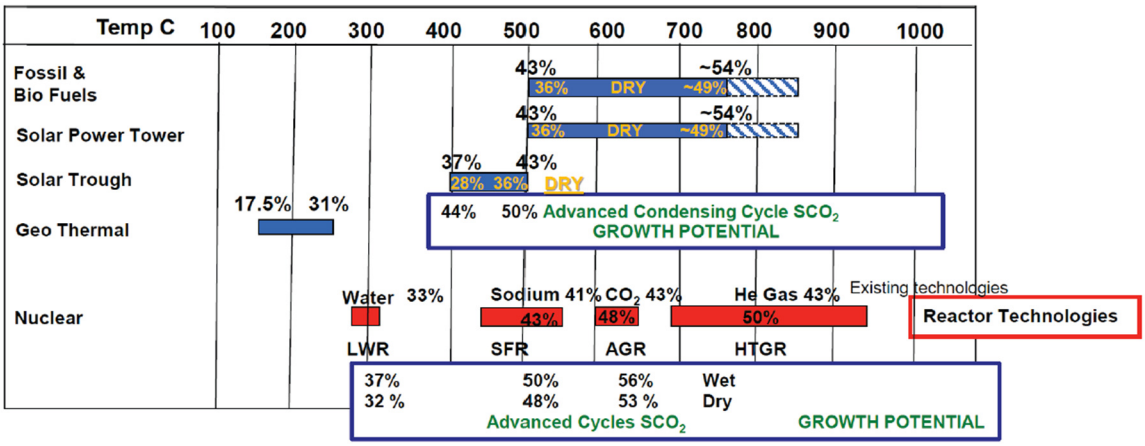


Figure 1-14 Expected s-$CO_2$ cycle efficiencies in different power plants [15]

Figure 1-15 shows the current status of different power cycles that can be used in the CSP plants. Despite lower operating temperatures compared with others, steam Rankine cycle is the only power cycle that is used in all the commercial power plants. S-$CO_2$ cycle is still under development for pilot studies. S-$CO_2$ combined cycle (CC) is another alternative that is considered in this dissertation.

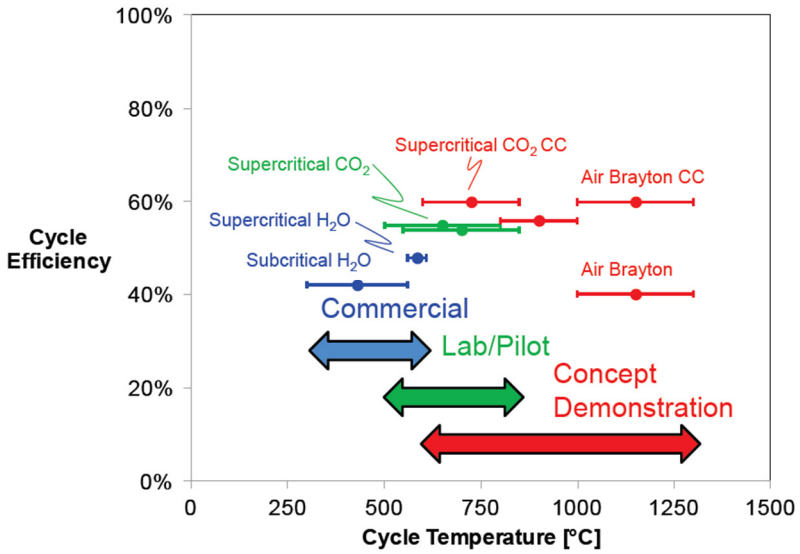


Figure 1-15 Current status of different power cycles to be used in CSP plants [18]

Carbon dioxide has also been proposed to be used as the HTF in the CSP plants. Regular CSP plants use oil, molten salt, or steam to absorb solar thermal energy in the receiver and transfer it to the working fluid in the power block. The maximum operating temperature of synthetic oil is 400℃, which limits the performance of the power plant. Molten salt can be used at higher temperatures (around 560℃); however, freeze protection systems are required. Direct steam generation requires complex control systems due to the phase change in the receiver and the storage capacity is limited. On the other hand, $CO_2$ does not have an upper-temperature limit and is non-toxic, inexpensive, and non-flammable. Moreover, it can be directly used in a Brayton cycle to generate power, which eliminates the heat exchanger between the HTF and the working fluid.

Figure 1-16 shows a CSP plant using s-$CO_2$ as the HTF and the working fluid with a single-tank thermal storage system. Considering the compact size of s-$CO_2$ turbomachinery, modular power generation in the receiver without energy storage has recently been proposed [19]. Table 1-2 shows the turbine size, shaft speed, and $CO_2$ mass flow rate for power ratings of 0.3, 3 and 300 MW. As

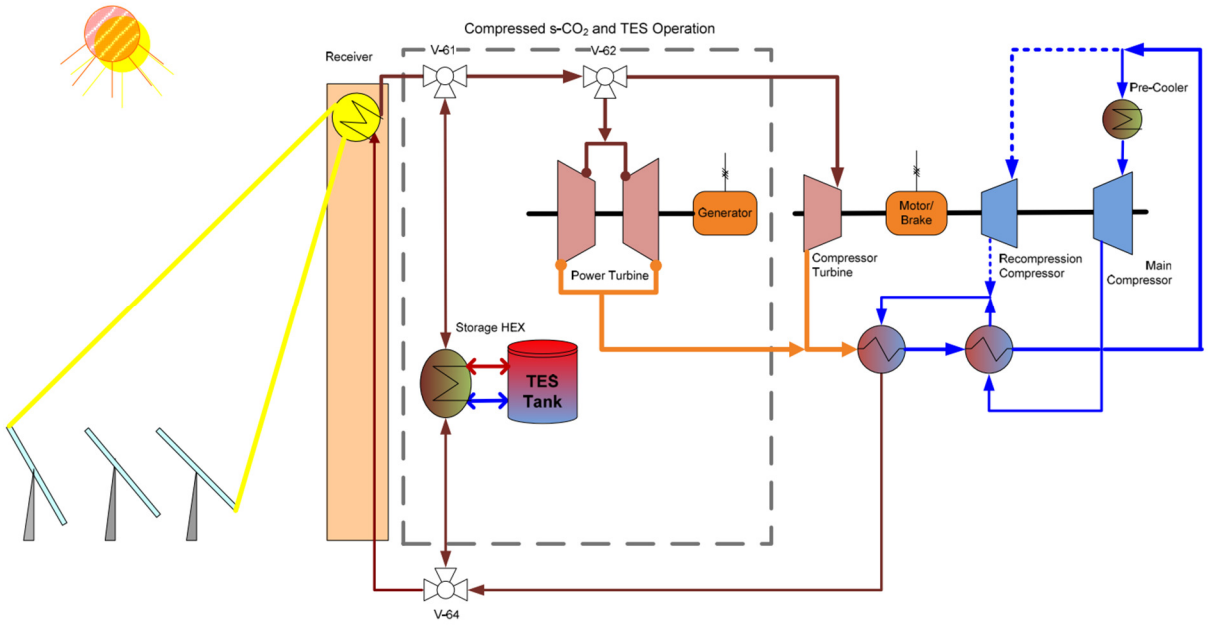


Figure 1-16 Direct s-$CO_2$ concept in SPT plant with thermal storage [20]

can be seen, at the 3MW power rate, the turbine wheel diameter is only 15 cm with a speed of 50,000 rpm. Therefore, it is possible to place the power cycle inside the tower (Figure 1-17). In other words, using this technology the power can be generated inside the tower right after the receiver and the fluid does not need to flow through long pipes. Hence, the system is more compact, and the pressure drop and heat loss are less, which consequently leads to higher efficiency and lower cost.

Despite all the positive aspects mentioned in this introduction, there are some uncertainties about utilization of s-$CO_2$ in the CSP plants. The main concerns are the high pressure of the fluid and lack of experience in operating closed loop Brayton cycles. This dissertation mainly focuses on the application of s-$CO_2$ in solar power tower plants, which requires the combined expertise of solar

Table 1-2 $CO_2$ turbine size at different power rates [19]

| Power Rate (MW) | Turbine Wheel diameter (m) | Desired Shaft Speed (RPM) | $CO_2$ Flow (kg/sec) |
|---|---|---|---|
| 0.3 | 0.04 | 125,000 | 3.5 |
| 3 | 0.15 | 50,000 | 35 |
| 300 | 1.5 | 3,600 | 3500 |

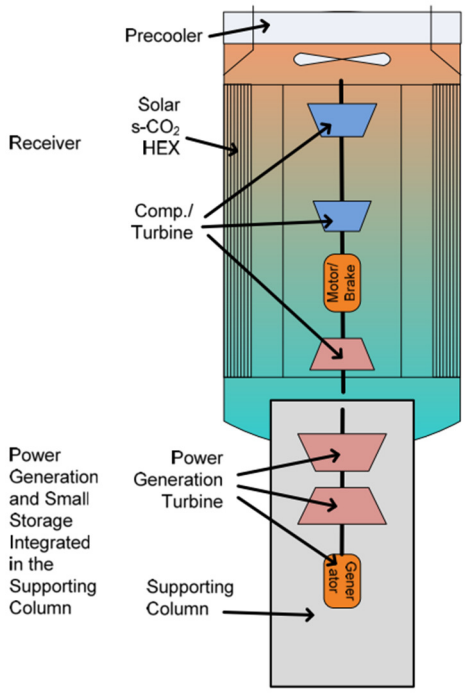


Figure 1-17 Schematic of modular tower concept using s-$CO_2$ [19]

thermal power and thermodynamics. Therefore, some parts of this dissertation are closely related to s-$CO_2$ applications while the other parts investigate the performance of power tower plants regardless to the heat transfer and the working fluids.

**1.7 Research Objectives**

The research objectives of this dissertation are:

(1) Analyzing the performance of s-$CO_2$ power cycles in CSP plants.

(2) Developing a computationally efficient method for the design of a heliostat field for a solar power tower plant.

(3) Developing an aiming strategy for uniform distribution of heat flux on the receiver surface.

(4) Developing a receiver model using s-$CO_2$ as the HTF.

(5) Modeling the thermal performance of a direct s-$CO_2$ receiver in a solar tower power plant.

# CHAPTER 2 DESIGN OF THE HELIOSTAT FIELD FOR SOLAR POWER TOWER PLANT[1]

## 2.1 Introduction

Solar power tower technology is deemed advantageous over other CSP technologies due to its ability to achieve high operating temperatures, resulting in greater power cycle efficiency. In these systems, the sun's rays are reflected and concentrated by a number of mirrors that are collectively called the heliostat field. The concentrated rays are focused onto a receiver that absorbs the radiation and transfers the thermal energy to a fluid. The thermal energy is then converted into power using conventional power cycles [14].

Optimal design of the heliostat field is of great importance and has been the subject of many studies because it typically accounts for approximately 50% of the total cost of the plant [21] and 40% of the energy losses [15]. Since the 1970s, several codes have been developed for this purpose, some of which are described in [22]. All of these codes use different approaches to maximizing the overall field efficiency which is defined as:

$$\eta = \eta_{cos} \times \eta_{att} \times \eta_{int} \times \eta_{s\&b} \times \eta_{ref} \tag{2-1}$$

where $\eta_{cos}$ represents the cosine effect efficiency, $\eta_{att}$ is the atmospheric attenuation efficiency,$\eta_{int}$ is the interception efficiency which accounts for the fraction of the reflected rays that hit the target, $\eta_{s\&b}$ is the shading and blocking efficiency, and $\eta_{ref}$ is the reflectivity of the heliostats. Of all the factors included in the equation, the shading and blocking factor is the most

[1] This chapter has been previously published (Besarati, Saeb M., and D. Yogi Goswami. "A computationally efficient method for the design of the heliostat field for solar power tower plant." *Renewable Energy* 69 (2014): 226-232.)

computationally intensive parameter because it not only depends on the sun's position and the heliostat locations, but is also a function of the location of the neighboring heliostats. During the optimization process, the relative position of each heliostat with respect to others is varied in order to maximize the overall efficiency, which requires significant computational time.

A number of methods have recently been proposed to reduce the time required to calculate the shading and blocking factor. Belhomme et al. [23] derived a method from known procedures of the collision analysis to identify the potential shading and blocking heliostats. In this method, all of the heliostats are represented by bounding spheres and possible collisions are evaluated by projecting the spheres onto the plane that is perpendicular to the sun vector (for the shading calculation). If the projections of the two bounding spheres overlap each other, the shading must be checked. Computational time is considerably reduced by using this method, as unnecessary calculations are avoided.

Noone et al. [24] used the same method and provided a model that is based on discretization of the heliostats and claimed that with a relatively coarse discretization of the heliostat surface, the method is sufficiently fast and accurate.

Collado et al. [25] divided the whole field into a number of sectors. In each sector, the relative position of the potentially shadowing heliostats with respect to a heliostat was first determined for the densest layout and minimum sun elevation of 15°. The relative positions remain the same over each sector. This was done specifically for PSA in Almería, Spain and it was shown that seven sectors, each containing three potential shadowing heliostats, can be used. However, the drawback of this method is that for other geographical locations and other limits of the sun elevation, the number and relative positions of the potential shadowing heliostats may change.

In this chapter, the methods used to evaluate the efficiency terms in equation (2-1) are described. A new and simple method is then proposed to identify the heliostats with the highest potential of shading and blocking with respect to a heliostat. Using this method, unnecessary calculations for heliostats that are incapable of shading or blocking are prevented, which improves the computational time. The method is based on a graphical approach that is applicable to both north-side and surrounding fields. The results are compared with the literature and very good agreement is obtained. In the next step, an optimization is performed to determine the optimal layout of the field for a 50 $MW_{th}$ power tower plant in Daggett, California, using genetic algorithms. This is done as a case study to demonstrate the optimization algorithm used in this study. Yearly insolation weighted efficiency is considered as the objective function where two parameters of the prophylaxis pattern proposed by Noone et al. [24] are the selected design variables, which control the shape of the field. The optimization algorithm and the physical constraints are explained in detail and the optimal field layout is presented.

**2.2 Model Description**

As previously mentioned, the instantaneous overall efficiency of the field is the product of the five efficiency terms. Having the instantaneous overall efficiency, one can calculate the yearly insolation weighted efficiency as [24]:

$$\eta_{year,w} = \frac{\sum_{day=1}^{365} \int_{sunrise}^{sunset} I_{bN}(t)\, \eta(t) dt}{\sum_{day=1}^{365} \int_{sunrise}^{sunset} I_{bN}(t)\, dt} \tag{2-2}$$

In order to compare the model with the available data in the literature, the yearly unweighted efficiency is obtained by:

$$\eta_{year} = \frac{\sum_{day=1}^{365} \int_{sunrise}^{sunset} \eta(t) dt}{\sum_{day=1}^{365} \int_{sunrise}^{sunset} dt} \tag{2-3}$$

2.2.1 Solar Time and Angles

The first step in calculating the efficiency of the field is finding the position of the sun which can be defined by two angles, i.e. the altitude and azimuth angles. The solar altitude angle, ($\alpha$), is given as [26]:

$$\sin\alpha = \sin L \sin\delta_s + \cos L \cos\delta_s \cos h_s \tag{2-4}$$

where L is the latitude of the location, $\delta_s$ is the declination angle, and $h_s$ is the hour angle. The declination angle is a function of the day number and can be found by:

$$\delta_s = 23.45° \sin\left[\frac{360(284+n)}{365°}\right] \tag{2-5}$$

where n is the day number during a year with January 1 being n=1. Hour angle is calculated by:

$$h_s = 15° \times (\text{hours from local solar noon}) \tag{2-6}$$

where morning values are negative. The azimuth angle is given as:

$$\sin a_s = \frac{\cos\delta_s \sin h_s}{\cos\alpha} \tag{2-7}$$

The hour angles for sunrise and sunset can be found by:

$$h_{ss} \text{ or } h_{sr} = \pm\cos^{-1}(-\tan L \tan\delta_s) \tag{2-8}$$

2.2.2 Solar Insolation

The ASHRAE Clear-SKY Radiation Model is used to estimate the solar insolation. The model is dependent on two monthly parameters and the relative air mass [27]. The air mass can be calculated by:

$$m = \frac{1}{\sin\alpha + 0.50572\,(6.07995+\alpha)^{-1.6364}} \tag{2-9}$$

where $\alpha$ is expressed in degrees. The beam normal radiation is given as:

$$I_{bN} = I \exp(-\tau_b m^b) \quad (2\text{-}10)$$

where

$$b = 1.219 - 0.043\tau_b - 0.151\tau_d - 0.204\ \tau_b\ \tau_d \quad (2\text{-}11)$$

$I$ is the extraterrestrial normal irradiance which is obtained by:

$$I = I_0(1 + 0.034\cos(\frac{360\ n}{365.25}) \quad (2\text{-}12)$$

where $I_0$ is equal to 1366.1 $\frac{W}{m^2}$ and n is the day number. Moreover, $\tau_b$ and $\tau_d$ are location specific and vary during the year. For Daggett, CA, they are given as [27]:

$$\tau_b = [0.310,0.332,0.345,0.368,0.395,0.397,0.497,0.484,0.398,0.377,0.324,0.303] \quad (2\text{-}13)$$

$$\tau_d = [2.470,2.320,2.297,2.196,2.127,2.145,1.821,1.868,2.157,2.154,2.400,2.490] \quad (2\text{-}14)$$

2.2.3 Cosine Efficiency

The most significant loss in the heliostat field is due to the angle between the incident solar beam radiation and a vector normal to the surface of the heliostat which is called the cosine effect [28]. Therefore, it depends on both sun and heliostat positions. As shown in Figure 2-1, for a field located in the northern hemisphere a heliostat situated in the south field has a higher incidence angle and, consequently, less effective reflector area and cosine factor.

Before evaluating the normal vector of the heliostat surface, two other vectors need to be defined, i.e. the vectors from the center of the heliostat to the sun and to the desired image location on the receiver surface.

If $\vec{S}$ and $\vec{t}$ are the unit vectors pointing to the sun and the receiver surface, respectively, the unit normal of the surface of the heliostat can be defined as:

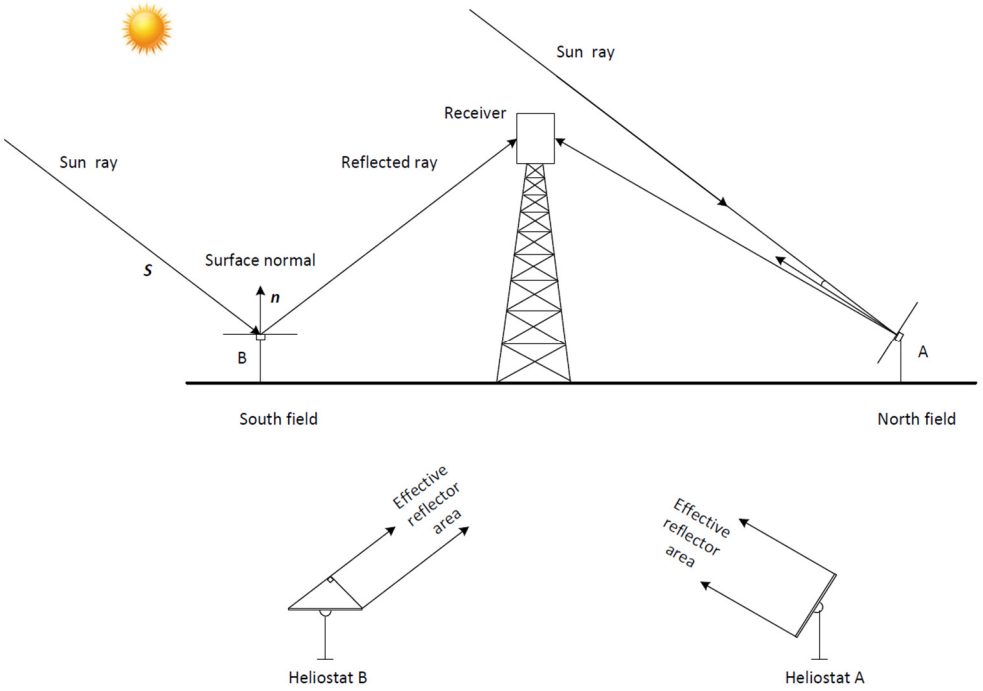


Figure 2-1 The cosine effect for a heliostat field located at the northern hemisphere [29]

$$\vec{n} = \frac{\vec{S} + \vec{t}}{|\vec{S} + \vec{t}\,|} \tag{2-15}$$

Then:

$$\eta_{cos} = \vec{n}.\vec{S} \tag{2-16}$$

2.2.4 Atmospheric Attenuation Efficiency

The reflected beam radiation from the surface of the heliostat may be scattered, depending on the distance between the heliostat and the receiver. This atmospheric attenuation efficiency can be calculated by [30]:

$$\eta_{att} = 0.99321 - 0.000176d + 1.97 \times 10^{-8} D^2 \quad D \leq 1000\ m \tag{2-17}$$

$$\eta_{att} = \exp(-0.0001106D) \qquad D > 1000m \tag{2-18}$$

where $D$ is the distance between heliostat and receiver. This formula is approximated for a visual range of 40 km.

2.2.5 Interception Efficiency

A portion of the reflected image may fail to intercept the receiver due to several factors such as tracking precision, shape of the sun, and non-uniformity of mirror surface, etc [28]. There are two general approaches to calculate the interception efficiency (spillage factor), i.e. ray tracing methods and analytical integration of the image shape produced by the mirror over the receiver domain.

Two well-known analytic flux density models that are used to evaluate the interception efficiency are the UNIZAR model from Universidad de Zaragoza [31] [32] and the HFLCAL model from the German Aerospace Center (DLR) [33].

According to [34], both of these models are appropriate tools though HFLCAL is much simpler and slightly more accurate than UNIZAR. Employing the HFLCAL model, the flux distribution along the receiver aperture plane is integrated to get the intercepted power at a certain point in time. The interception efficiency is then [33]:

$$\eta_{int} = \frac{1}{2\pi\sigma_{tot}^2}\int_x\int_y \exp\left(-\frac{x^2+y^2}{2\sigma_{tot}^2}\right)dy\,dx \tag{2-19}$$

where $\sigma_{tot}$ is the total dispersion of the flux distribution. According to [34], the total dispersion can be calculated as:

$$\sigma_{HF} = \frac{\sqrt{D^2(\sigma_{sun}^2+\sigma_{bq}^2+\sigma_{ast}^2+\sigma_t^2)}}{\sqrt{\cos rec}} \tag{2-20}$$

where $\sigma_{sun}, \sigma_{bq}, \sigma_{ast}, \sigma_t$ are the standard deviations due to sunshape error, mirror slope error, astigmatic effect and tracking error, respectively. Moreover, $D$ represents the actual distance between the heliostat surface center and the aim point, while $\cos rec$ is the incidence cosine of the reflected central ray from the heliostat on the receiver surface.

2.2.6 Shading and Blocking Efficiency

The shading and blocking factor not only depends on the sun's position and the individual location of the analyzed heliostat, but is also a function of the location of neighboring heliostats. Shading occurs when the incoming solar radiation is obstructed by a neighboring heliostat. On the other hand, blocking occurs when the reflected image from a heliostat is partially blocked by an adjacent heliostat from reaching the receiver (Figure 2-2). The shading and blocking factor of a heliostat is defined as the area not shaded or blocked divided by the total heliostat area.

The shading and blocking loss can be minimized by increasing the distance between the heliostats. On the other hand, increasing the size of the field leads to other consequences such as higher atmospheric attenuation and higher land costs. Therefore, an optimization study needs to be

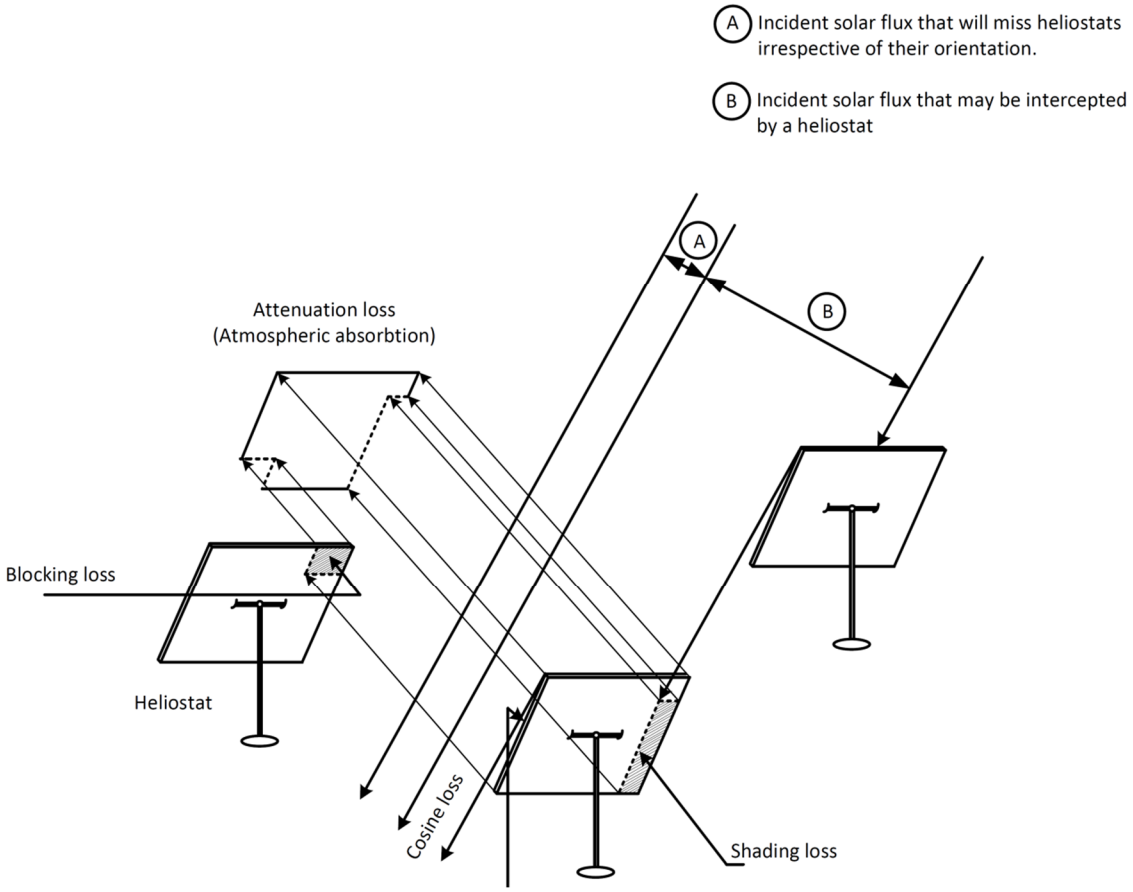


Figure 2-2 Shading and blocking losses in a heliostat field (adapted from [29])

carried out to find the optimal field layout. A number of codes have been developed for this purpose which are well documented in [22].

The required time for calculating the shading and blocking efficiency is usually high as it is dependent on the sun position, individual location of the analyzed heliostat, and the locations of the neighboring heliostats. However, the computational time can be significantly reduced by considering only a subset of the heliostats with high potential of shading or blocking. In order to do so, a novel approach is used in this project which is applicable to both surrounding and north field designs. The procedure is summarized in the following steps with the aid of Figure 2-3:

(1) The sun ray that intersects the center of the analyzed heliostat is projected onto the field.

(2) A line perpendicular to the projected sun ray is drawn as the red dashed line in Figure 2-3.

(3) A circle is drawn with its center at the center of the analyzed heliostat. A discussion on the size of the circle is provided later.

(4) The heliostats that are located in the half-circle that is closer to the sun have the potential to shade the analyzed heliostat.

(5) Out of the heliostats that are situated in the half-circle, those with the lowest perpendicular distance to the projected sun ray have the highest potential to shade the analyzed heliostat.

In our calculation, the first three heliostats with the highest potential for shading (red circles in Figure 2-3) were selected for further investigation, however, one can select more. The size of the circle that was drawn in step 3 is a function of the size of the heliostats and the separation distance between the adjacent heliostats. The characteristic diameter of each heliostat (DM) as shown in Figure 2-4, which includes both of these parameters, was defined in [25] as:

$$DM = DH + dsep \tag{2-21}$$

where

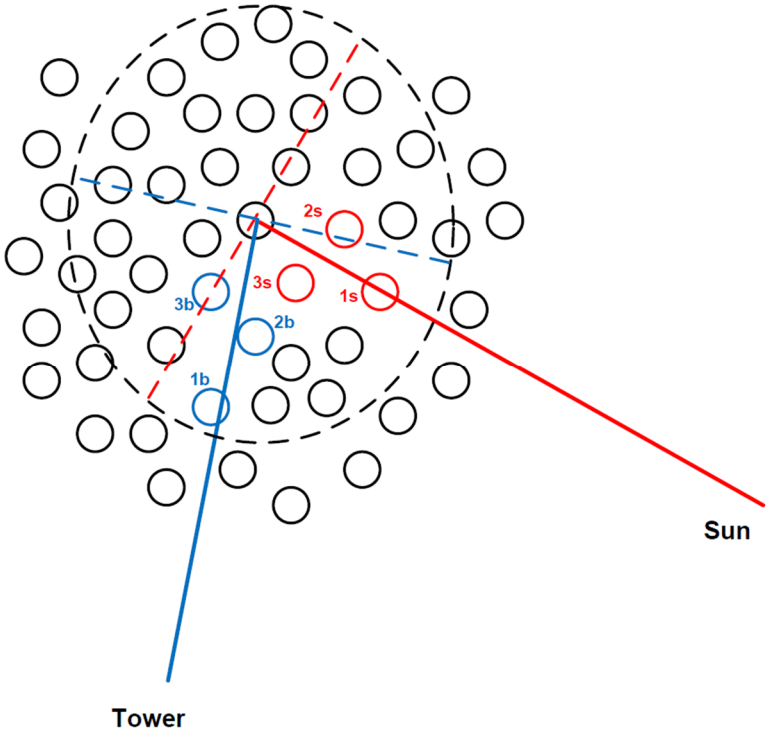


Figure 2-3 A diagram to identify the potential shadowing and blocking heliostats. The heliostats that can potentially shade are shown with "s" while those that can block the reflected rays are represented by "b". The lines perpendicular to the sun ray or the reflected ray are dashed.

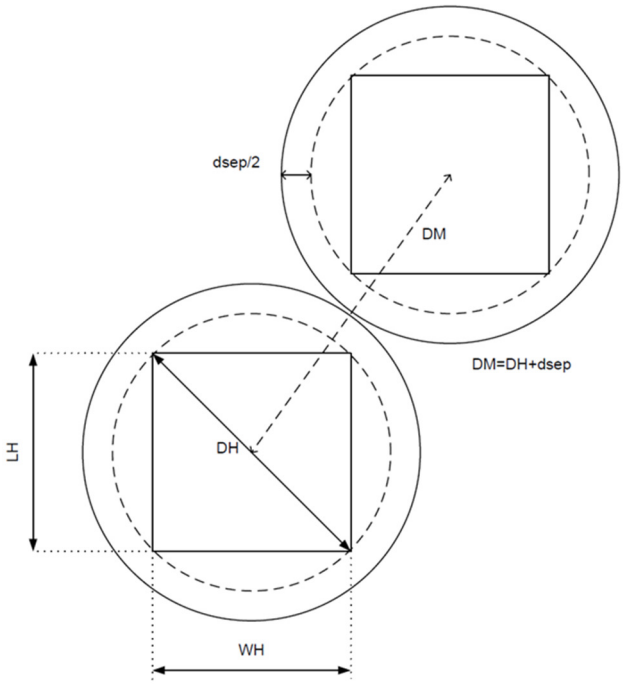


Figure 2-4 Minimum distance between the adjacent heliostats

$$DH = \sqrt{L_H^2 + W_H^2}$$

where for the densest field layout dsep=0. After many tests, it was found that R=2.5DM can be considered as an appropriate radius for the circle mentioned in step 3, however, one may alter and check other values for the new locations and layouts. Though the above steps are specifically for identifying the shading heliostats, the blocking heliostats can be obtained in the same manner by using the reflected ray (solid blue line in Figure 2-3) instead of the sun's ray. With regard to blocking in the radial-staggered layout, the above method is not required since the blocking heliostats are easily identified as the two closest heliostats in the row next to the analyzed heliostat and the one that is two rows over and directly in front (on the same radial axis) of the analyzed heliostat [25]. On the other hand, if another layout such as the phyllotaxis pattern is applied [24], the above approach can be used.

After identifying the shadowing and blocking heliostats, the method proposed by Sassi [35] is used to calculate the shading and blocking efficiency for each heliostat. According to this method, the surface of each heliostat is divided into several vertical strips. The surfaces of the potential shadowing and blocking heliostats are projected onto the surface of the analyzed heliostat. Among all the shading and blocking projections, the maximum height is selected for each strip. Dividing the heliostat surface that is not affected by shading and blocking by its total surface area gives the shading and blocking efficiency.

In order to ensure that the model can correctly identify the potential shadowing and blocking heliostats, all of the cases that were studied in [25] and its supplementary material are investigated using the new algorithm. Figure 2-5 compares the shading and blocking efficiency maps obtained by the new method and given in [25]. The calculations are done for 345$^{th}$ of the year at 9:00 AM.

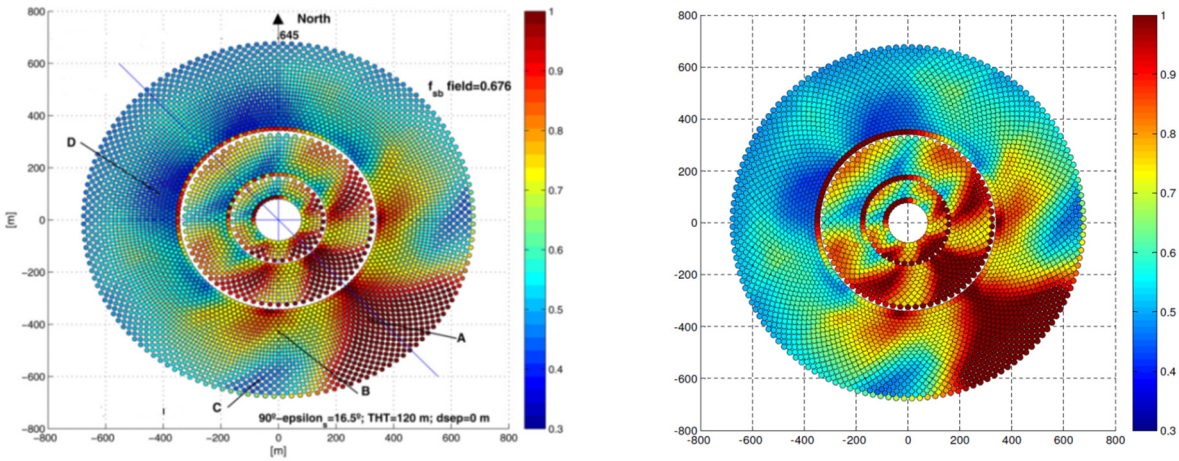


Figure 2-5 Left) Map of shading and blocking efficiency for a field layout by Collado et al. [25]; Right) The shading and blocking map obtained by the proposed method

Table 2-1 The breakdown of heliostat field efficiency terms for PS10. Comparison between the proposed model and the model presented by Noone et al. [24]

| Yearly unweighted efficiency | Noone et al. [24] | New Model |
|---|---|---|
| $\eta_{cos}$ | 0.8283 | 0.8315 |
| $\eta_{s\&b}$ | 0.9255 | 0.9161 |
| $\eta_{int}$ | 0.9926 | 0.9931 |
| $\eta_{att}$ | 0.9498 | 0.9498 |
| $\eta_{ref}$ | 0.88 | 0.88 |
| $\eta_{year}$ | 0.6338 | 0.6379 |

The results show that the new method is able to calculate the shadowing and blocking factor very accurately. The mean shadowing and blocking factor using the new method obtained as 0.678 which is very close to 0.676 given in the paper. The modeling results by Noone et al. [24] for the PS10 11 $MW_e$ power tower plant located in Spain are used to validate the proposed model (Table 2-1). The field parameters of PS10 are taken from [36]. As can be seen, the results are very close to the published data and the yearly unweighted efficiency error is only 0.0041.

### 2.3 Optimization of Heliostat Field Layout

Optimization of the heliostat field layout is of great importance, as it is the most expensive part of the plant. Moreover, close to 40% percent of energy losses in the plant are due to the losses

Table 2-2 Field parameters

| | |
|---|---|
| Heliostats | |
| Width | 12.84 m |
| Height | 9.45 m |
| Reflectivity | 0.88 |
| | |
| Receiver | |
| Tower height | 115 m |
| Tilt angle of the aperture | 12.5° |
| Aperture width | 13.78 m |
| Aperture height | 12 m |

in the heliostat field. It is for this reason that optimization algorithms are incorporated with almost all the available software for the heliostat field design. There are usually three main parameters to be optimized, i.e. energy efficiency, cost, and field density. Some codes optimize only one of these functions, such as MIRVAL, which maximizes the provided energy by the field [22] . On the other hand, some codes combine two functions in a single function to be optimized, for instance, total system cost/annual MWh [37] or field density ×annual efficiency [38]. Multi-objective optimization is an alternative approach which was used by Zhang et. al [39]. Specific energy cost and investment cost were considered as the objective functions to be minimized, however, the cost data were taken from [40], which is not up to date. In this research, yearly insolation weighted efficiency is selected as the objective function, however, rather than calculating the efficiency in every single day of the year, the 21$^{st}$ of each month is selected. As a case study, a 50 MWth heliostat field located in Daggett, California is considered. The field parameters are similar to PS10 and are provided in Table 2-2. Moreover, it is assumed that $\sigma_{sunshape}$ is 2.51 mrad, $\sigma_{optical}$ is 2.9 mrad, the facet canting is on-axis parabolic, and the minimum distance to the tower is 0.75×Tower height.

Although the radial-staggered model is known as the most common layout to be used in heliostat field design, a new pattern has recently been proposed by Noone et al. [24], which is inspired from spiral patterns of the phyllotaxis disc. It was shown in the paper that replacing the

radial-staggered layout with the new pattern increases the overall efficiency while considerably reducing the land area. The required equations for the pattern are given as [24]:

$$\theta_k = 2\pi\varphi^{-2}k \tag{2-22}$$

$$r_k = ak^b \tag{2-23}$$

where *a* and *b* have to be determined by employing an optimization algorithm. The range of values of *a* and *b* are considered as [2,8] and [0.45,0.7], respectively.

Before performing the optimization study on the field, the physical constraints need to be defined. It is very likely that mathematical optimization leads to a layout which is not physically viable. An important constraint of the field is related to the acceptance angle of the cavity receiver. The optimization program tends to select the heliostats with the minimum distance from the tower, however, some of those may be located in places where the incidence angle of the reflected ray is greater than the acceptance angle of the receiver. This problem does not exist in cylindrical receivers which accept the reflected rays from any azimuth angle.

In this study, the acceptance angle of a cavity receiver is considered by defining an angle dependent transmissivity function. The function calculates the (real or virtual) transmissivity of an aperture as a function of the incident angle from each heliostat. The advantage of defining a transmissivity function over considering a single acceptance angle is that the transmissivity function is continuous and there is a smooth selection rather than a sharp behavior. Figure 2-6 depicts the transmissivity function used in this study. The explanation about how this function is incorporated into the program is given later.

Another important constraint that needs to be addressed is the minimum distance between the adjacent heliostats. According to Figure 2-4, this distance is defined as the sum of the heliostat

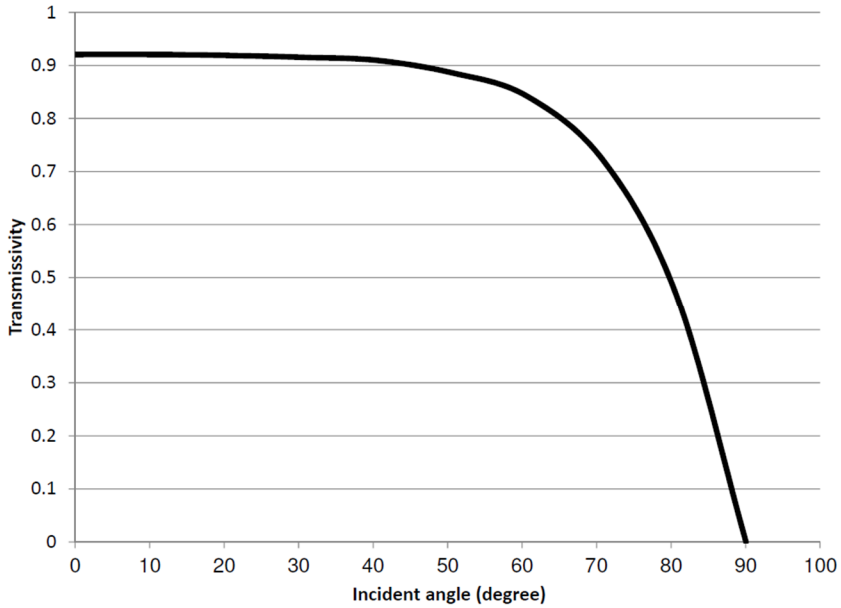


Figure 2-6 Transmissivity of aperture as a function of incident angle

characteristic diameter and an additional separation distance (equation (2-21)). The program is written in a way that during each iteration the distance of each heliostat from its neighbors is checked to ensure that the minimum distance constraint is not violated.

An optimization code is developed based on genetic algorithms to handle the required optimization tasks in this study [41] [42]. The evolutionary process of optimum selection of the design variables to obtain the maximum yearly insolation weighted efficiency is used with a population size of 40, crossover probability of 0.9, and mutation probability of 0.1. The general algorithm used in this study can be summarized as follows:

(1) Considering the ranges that have already been defined for the design variables, the optimization program assigns random values to $a$ and $b$ in the range of $[2 \leq a \leq 8]$ and $[0.45 \leq b \leq 0.7]$.

(2) A much larger pattern than the expected size of the field is generated using equations (2-22) and (2-23). In this study, 3000 heliostats are generated in this step.

(3) The value of $\eta_{cos} \times \eta_{att} \times \eta_{int} \times$ transmissivity is calculated for each heliostat at noon, March 21st. Including transmissivity in this calculation imposes the first constraint to the problem. Then, all 3000 heliostats are sorted in descending order based on the calculated values.

(4) Power, which is equal to $\eta_{cos} \times \eta_{att} \times \eta_{int} \times \eta_{ref} \times A \times I_{ref}$, is calculated for all the heliostats. $I_{ref}$ is obtained from [27] for Daggett at noon, March 21st as 926 $\frac{W}{m^2}$. Shading and blocking efficiency is not calculated in this step in order to have a quick selection process.

(5) Starting with the first heliostat in the ordered array, the power calculated in step 4 for each heliostat is added until the total required power (50 MWth in this study) is obtained.

(6) The distances between the adjacent heliostats are checked to make sure that the second constraint is not violated.

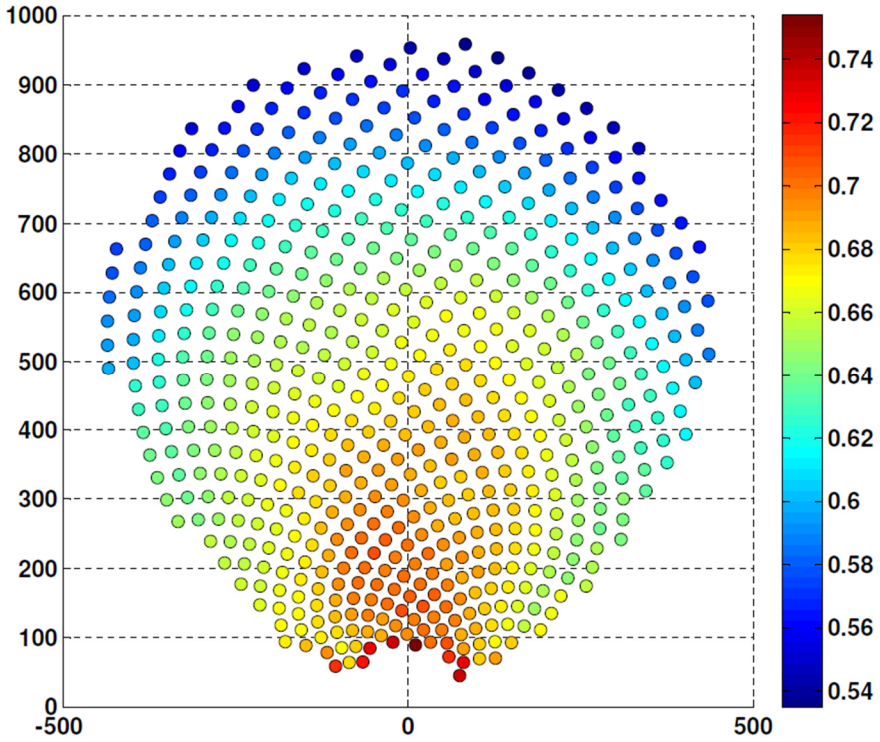


Figure 2-7 Optimal field layout and yearly unweighted efficiency of each heliostat

Table 2-3 The breakdown of heliostat field efficiency terms for the optimal field layout

| Yearly unweighted efficiency | Optimal field layout |
|---|---|
| $\eta_{cos}$ | 0.8267 |
| $\eta_{s\&b}$ | 0.9698 |
| $\eta_{int}$ | 0.9710 |
| $\eta_{att}$ | 0.9383 |
| $\eta_{ref}$ | 0.88 |
| $\eta_{year}$ | 0.6446 |

(7) Having the total number of heliostats, the yearly insolation weighted efficiency (including shading and blocking efficiency) is evaluated. As previously mentioned, rather than calculating the efficiency for every single day of the year, the 21$^{st}$ of each month is selected.

(8) Random generation of the design variables continues (step 1) until the maximum efficiency is achieved using genetic algorithm optimization.

Following the above method for Daggett, it is found that the maximum yearly insolation weighted efficiency of 0.6830 can be achieved. The optimal field layout is shown in Figure 2-7 where the corresponding *a* and *b* parameters are 3.935 and 0.7, respectively. There are 594 heliostats in this layout which covers 72,075$m^2$ of the field area. Figure 2-7 also depicts the yearly unweighted efficiency of each heliostat ranging from 0.5349 to 0.7540. It is noteworthy that these results are obtained assuming the same field parameters as PS10 in Spain which may not be optimal. For example, the receiver size and orientation may need to be changed for the new location which is out of the scope of this dissertation. A summary of the efficiency terms for the optimal field layout is given in Table 2-3.

**2.4 Summary and Concluding Remarks**

A new and simple method is proposed to identify the heliostats with high potential for shadowing and blocking with respect to the analyzed heliostat. Using this method, unnecessary

calculations for heliostats that are incapable of shading or blocking are eliminated which improves the computational time. A comparison with the literature showed that the new method is able to predict the shading and blocking factor accurately. In the next part of the chapter, a 50 MWth heliostat field was designed for Daggett, California using genetic algorithm optimization method. ASHREA clear sky model was used to predict the insolation level. Two parameters which define the shape of the field layout were considered as the design variables while yearly insolation weighted efficiency was selected as the objective function to be maximized. The acceptance angle of the cavity receiver and the distance between the adjacent heliostats were included as the physical constraints in the optimization model. The maximum yearly insolation weighted efficiency was obtained as 0.6830 using 594 heliostats. The breakdown of heliostat field efficiency terms for the optimal field layout was also provided.

# CHAPTER 3 DEVELOPING HELIOSTAT AIMING STRATEGY FOR UNIFORM DISTRIBUTION OF HEAT FLUX ON THE RECEIVER[2]

## 3.1 Introduction

In a solar power tower plant, the receiver plays an important role of intercepting reflected solar radiation from the heliostat field and transferring thermal energy to the heat transfer fluid. The main challenge associated with this process is the high temperature gradient at the receiver surface which may lead to local hot spots, and consequently, degradation and failure of the receiver [43]. The temperature distribution on the receiver surface depends on the design of the receiver, thermophysical properties of the absorber, heat transfer fluid, and the heat flux distribution [44]. Distribution of the heat flux on the receiver surface is the only factor which is closely connected with the performance of the heliostat field. Therefore, it can be controlled by defining several aim points and adjusting the heliostats.

Two aiming techniques were described by Kistler [40]. One technique, which is called one-dimensional smart aiming, is to focus the heliostats along the height of the receiver until the spillage loss starts to increase. The heliostats that are closer to the tower are usually focused at the top or the bottom of the receiver while those which are farther are aimed closer to the center of the receiver surface. The two dimensional smart aiming is similar, except the images are distributed in two dimensions. This technique is usually recommended for rectangular cavity apertures or flat plates, as using other shapes of the receivers may lead to increase in the spillage loss. Although these

[2] This chapter has been previously published (Besarati, Saeb M., D. Yogi Goswami, and Elias K. Stefanakos. "Optimal heliostat aiming strategy for uniform distribution of heat flux on the receiver of a solar power tower plant." *Energy Conversion and Management* 84 (2014): 234-243.)

methods perform well, the technological development of thermal receivers and increasing size of the power plants demand more sophisticated aiming strategies.

In a paper presented by Garcia-Martin et al. [45] an automatic closed-loop control method was developed to optimize the temperature distribution within a volumetric receiver at PSA power plant. The method is based on measuring the temperature at different points on the receiver surface and transferring the power from one area to another by changing the aiming points of the heliostats when the temperature reaches a maximum tolerance value. In another study, Salome et al. [44] presented an open loop approach to control the flux distribution on the surface of a flat plate receiver. In this method, a set of aiming points are defined and a grid is formed on the surface of the receiver. Then, an optimization algorithm called "TABU+ specific neighborhood" is used to find the best aiming point for each heliostat. The objective is to minimize the flux spread, $F_{max} - F_{min}$, while keeping the spillage loss above a predetermined value. At the first step all heliostats are focused on the center of the receiver. At each iteration, one heliostat is selected and its aiming point is changed. If the modification leads to an improvement in the objective function, it will be saved for the next iteration. It was shown in the paper that the spread of the flux density is decreased by 43% with an added spillage loss of 10% using the proposed algorithm.

Optimization in engineering design has always been a subject of interest to engineers. The genetic algorithm (GA), as one of the most popular optimization techniques, has been found very useful in solving complex real-world design optimization problems since it works with a population of candidate solutions, not a single point in the search space. This helps to avoid being trapped in local optima as long as the diversity of the population is well preserved [46].

Over the past decade, genetic algorithm has been extensively used for the optimization of solar thermal systems [47]. Varun and Siddhartha used GA to optimize the thermal performance of a

flat plate solar air heater [48]. Loomans and Visser applied GA for the optimization of a solar water heater system [49]. Godarzi et al. [50] employed GA to optimize the performance of a solar absorption chiller. GA and artificial neural network were used together by Kalogirou [51] to find the optimum combination of the collector area and storage-tank size for a solar industrial process heat system. Baghernejad and Yaghoubi [52] conducted an exergoeconomic analysis and optimization of a 400 MW integrated solar combined cycle system using GA. Ahmadi et al. [53] investigated multi-objective optimization of a solar dish Stirling engine using GA by considering three objective functions, i.e. output power, overall thermal efficiency, and rate of entropy generation. Cabello et al. [54] developed a program based on GA to find the optimal size of the solar collector area, thermal storage and power of the auxiliary system in a direct steam generation power plant.

In this chapter, a new optimization approach based on the principles of GA is proposed to find the optimal flux distribution on the receiver surface of a solar power tower plant. The objective is to minimize the standard deviation of the flux density distribution on the receiver surface by changing the aiming points of individual heliostats. The HFLCAL method [33] is used to find the flux distribution of individual heliostats and is validated against experimental data. After presenting the optimization methodology, the final results are provided and the influences of different parameters are investigated.

**3.2 Flux Density Model**

The flux density on the surface of a receiver can be found numerically or analytically. In the numerical approach, called Monte Carlo ray tracing method, a large number of rays are generated and traced through different optical stages. A flux map on the receiver surface can be generated from the intersection of the reflected rays and the surface. SolTrace software [55], developed by the National Renewable Energy Laboratory (NREL), can be used to predict the flux density distribution

on the receiver surface accurately using the Monte Carlo ray tracing method. Although the numerical method is accurate, it requires large computational time.

Two well-known analytic models that are used to evaluate the flux density and interception efficiency are the UNIZAR model from the Universidad de Zaragoza [32] and the HFLCAL model from DLR (the German Aerospace Center) [33]. According to [34], both of these models are appropriate tools though HFLCAL is simpler and slightly more accurate than UNIZAR. The HFLCAL model is used in this study to evaluate the flux density distribution of each heliostat on the receiver surface. The flux map resulting from the entire field is generated by superimposing the flux densities of the individual heliostats.

3.2.1 HFLCAL Model

In the HFLCAL model a circular normal distribution is used to find the flux density distribution on the receiver surface, given as [44]:

$$F(x,y) = \frac{P_h}{2\pi\sigma_{HF}^2} \exp\left(-\frac{(x-x_t)^2 + (y-y_t)^2}{2\sigma_{HF}^2}\right) \tag{3-1}$$

where $P_h$ is the total power reflected by a heliostat, $\sigma_{HF}$ is the effective deviation, and $(x_t, y_t)$ are the coordinates of the aiming point on the receiver surface. $P_h$ is given as:

$$P_h = I_{bN} \times A \times \eta_{cos} \times \eta_{att} \times \eta_{ref} \tag{3-2}$$

where $I_{bN}$ is the beam normal irradiation , $A$ is the mirror area, $\eta_{cos}$ is the cosine factor of the angle between the sun ray and the normal to the heliostat surface, $\eta_{att}$ is the atmospheric attenuation factor, and $\eta_{ref}$ is the reflectivity of the heliostat.

The effective deviation, $\sigma_{HF}$, is the result of the convolution of the four Gaussian error functions, namely, the sun shape error due to the non-uniform distribution of the solar intensity across the sun disk ($\sigma_{sun}$), the beam quality error due to the mirror slope error $(\sigma_{bq})$, the astigmatic

error representing any extra deformation of the reflected ray if the incident ray is not parallel to the mirror's normal ($\sigma_{ast}$), and the tracking error ($\sigma_t$). $\sigma_{HF}$ is given as [34]:

$$\sigma_{HF} = \frac{\sqrt{D^2(\sigma_{sun}^2 + \sigma_{bq}^2 + \sigma_{ast}^2 + \sigma_t^2)}}{\sqrt{\cos rec}} \tag{3-3}$$

where $D$ is the distance between the center of the heliostat and the aim point, and cos *rec* represents the cosine of the angle between the reflected ray and the normal to the receiver surface. The beam quality error is due to imperfections of the heliostat surface and is related to the slope error by:

$$\sigma_{bq} = (2\sigma_s)^2 \tag{3-4}$$

The standard deviation of the astigmatic error is given as:

$$\sigma_{ast} = \frac{\sqrt{0.5(H_t^2 + W_s^2)}}{4D} \tag{3-5}$$

where $H_t$ and $W_s$ are the image dimensions in the tangential and sagittal plane [56] and are given as:

$$H_t = d\left|\frac{D}{f_d} - \eta_{cos}\right| \tag{3-6}$$

$$W_s = d\left|\frac{D}{f_d}\,\eta_{cos} - 1\right| \tag{3-7}$$

where $f_d$ represents the focal distance and $d$ is a general dimension of the heliostat. In this study, $d$ is equal to the square root of the heliostat area.

The interception efficiency, defined as the fraction of the reflected power that reaches the receiver surface at a certain point in time, is calculated by [33]:

$$\eta_{int} = \frac{1}{2\pi\sigma_{HF}^2}\int_x\int_y \exp\left(-\frac{(x-x_t)^2 + (y-y_t)^2}{2\sigma_{HF}^2}\right)dx\,dy \tag{3-8}$$

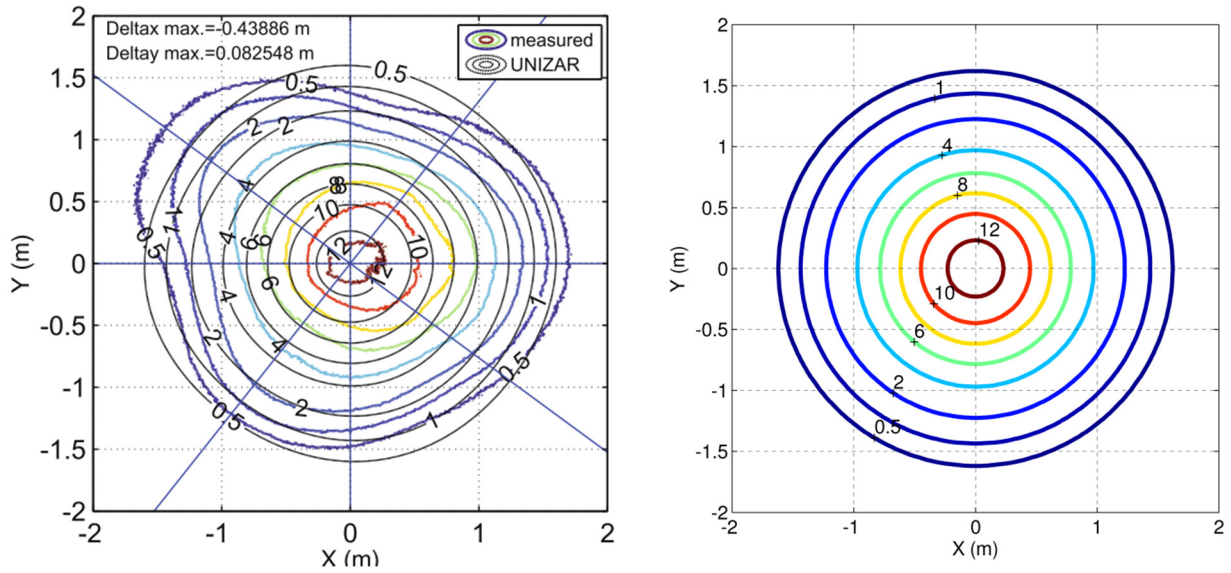


Figure 3-1 Contours of flux densities for a heliostat in the PSA power plant. Left) measured and calculated values using the UNIZAR model [34]; Right) Calculated values using the HFLCAL model

A model is developed in MATLAB based on the HFLCAL method to calculate the flux density at the receiver of a solar power tower plant. The model is validated against the experimental data available from the PSA power plant [17]. Each heliostat used in the experimental study was 6.6778 m wide and 6.819 m high and contained 12 spherical facets (1.105× 3.010 m). However, all the heliostats were modeled as single mirrors in the simulation. The total mirror area of each heliostat was 39.9126 $m^2$. The information about each heliostat including the coordinates, actual distance to the receiver plane, and the focal length are given in [34]. It is assumed that the direct normal irradiation is 1 $kW/m^2$, the mirrors are perfect reflectors, and atmospheric attenuation is negligible. Therefore, the total power reflected by each heliostat is given as:

$$P_h = 39.9126 \times \eta_{cos}(\text{kW}) \tag{3-9}$$

Using equation (3-1) and the information given in [34], the flux densities for the heliostats are obtained. Figure 3-1 depicts the contours of flux densities for one of the heliostats. The left figure shows the measured as well as the simulated values using the UNIZAR model. The right figure

depicts the flux density distribution obtained from the HFLCAL method. As can be clearly seen, analytical methods are not able to exactly predict the real shapes of the flux density contours due to the circular symmetry assumption, however, they are able to predict accurately the flux density levels on the receiver surface. By comparing the two figures, it can be concluded that the HFLCAL method works very well and can be confidently used.

### 3.3 Optimization Algorithm

An optimization algorithm is developed based on the principles of GA. GA belongs to the larger class of evolutionary algorithms that mimic the process of natural evolution in order to find the best solution to an optimization problem [57]. The genetic operators such as mutation and crossover are applied to a population of candidates. The best candidates are selected at the end of each generation by measuring the fitness function. The process is repeated for a number of generations until the best solution is found. The optimization algorithm can be summarized as:

(1) Initial population is randomly generated.

(2) The fitness function is evaluated for each population.

(3) The offsprings are generated by applying genetic operators, i.e. crossover and mutation, to probabilistically selected individuals from the initial population.

(4) The fitness function is evaluated for the offsprings.

(5) New population is selected and the algorithm continues from step 2.

In this chapter, the genetic algorithm is employed to find an aiming strategy for a solar power tower plant in order to distribute the flux uniformly on the receiver surface. The main objective is to minimize the standard deviation of the flux density distribution, which is found by measuring the flux density at multiple points on the receiver surface. The detailed methodology is explained in subsequent sections.

### 3.3.1 Generating Initial Population

In the GA, each candidate is usually represented as a vector containing information about all the design variables. In this problem, each candidate is represented by a matrix where the numbers of columns and rows are equal to the numbers of heliostats and aiming points, respectively. Therefore, for *n* number of aiming points and *m* number of heliostats, the size of the matrix will be $n \times m$, as shown in Figure 3-2. The heliostats are numbered from 1 to *m*. Similarly, the aiming points are numbered from 1 to *n*. The matrix shown in Figure 3-2 indicates that the first heliostat is focused on the first aiming point; the second heliostat is focused on the third aiming point; and the $m^{th}$ heliostat is focused on the $(n\text{-}1)^{th}$ aiming point. The number of matrices that are randomly generated in this step, called the number of initial population, is defined by the user. A MATLAB cell data structure is used for the programming [58].

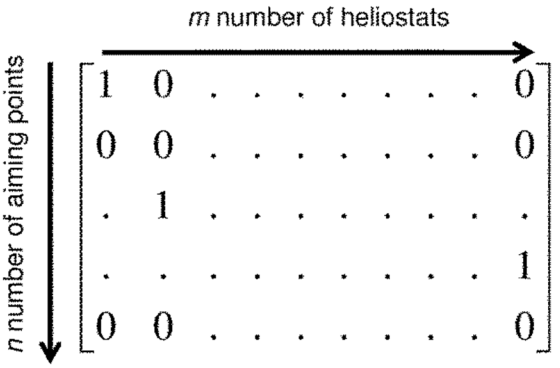


Figure 3-2 A sample form of a candidate solution

### 3.3.2 Crossover Operator

In the crossover process two of the candidate solutions are selected and combined to produce children, which are the new candidate solutions. The crossover probability ($P_c$) is the parameter that controls how often the crossover will be performed, which is defined by the user [57]. The crossover process consists of three main steps as shown in Figure 3-3:

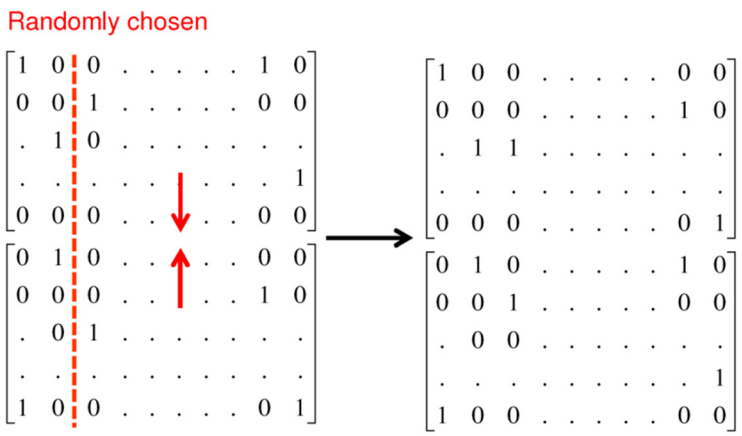


Figure 3-3 Crossover operation on two of the candidate solutions

(1) Two of the candidate solutions are randomly selected.

(2) A column number is randomly selected.

(3) The values are swapped between the two matrices following the selected column number.

The main intention of using crossover is to find new solutions that contain good parts of the old solutions; however, it does not necessarily mean that the offsprings are any better than the parents.

3.3.3 Mutation Operator

Mutation is a genetic operator which helps to avoid being trapped in the local minimum and maintains the diversity in the population [57]. Mutation probability ($P_m$) controls how often the mutation is performed on the old population. The mutation is incorporated into the program as:

(1) A candidate solution from the old population is randomly selected.

(2) One of the columns of the chosen matrix is selected. The element in that column that is equal to 1 is changed to 0.

(3) Another element of that column is randomly selected and is changed from 0 to 1.

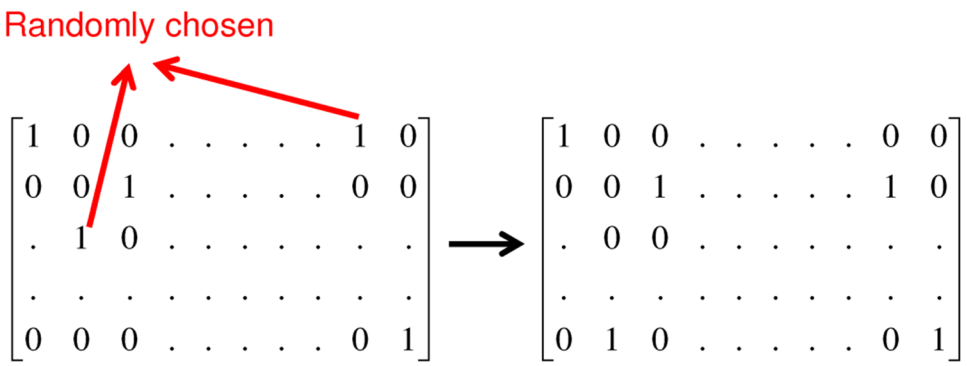


Figure 3-4 Mutation operation on one of the candidate solutions

Considering the physics of the problem, it is expected that performing mutation only on one column will not change the objective function very much. In other words, changing the aiming point of a single heliostat will not affect the overall standard deviation of the flux density distribution significantly. Therefore, the program is written in a way that allows mutation to be performed on multiple columns of the selected matrix. The number of mutations is defined by the second mutation probability ($P_{mm}$). In other words, for each column a random number is generated and mutation will be performed on that column if the random number is less than $P_{mm}$.

Figure 3-4 depicts the mutation operation on a randomly selected matrix. As it can be seen, mutation is performed on the second and $(m\text{-}1)^{th}$ columns, which means that the aiming points of the second and $(m\text{-}1)^{th}$ heliostat are changed.

3.3.4 Selection

The last step is to select the best candidates from the old population and the offsprings for the next generation. Tournament selection strategy is used for this purpose which involves running several tournaments between two randomly chosen candidates. The winner of each tournament is the one with the lowest standard deviation of the flux density distribution on the receiver surface. The tournament competitions continue until the number of the selected candidates equals the number of

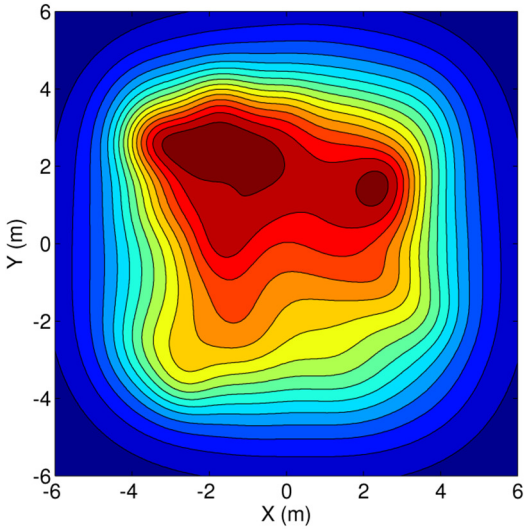


Figure 3-5 Flux density map for a randomly generated binary matrix

initial population. One generation is completed by selecting the new population and the program proceeds to the next generation. The program continues to run until the maximum number of generations defined by the user is reached or some other termination criterion is met.

3.3.5 Self-Modifying Algorithm

As it is already discussed, the optimization algorithm is based on generating random binary matrices. The flux density maps produced by these random matrices do not usually reflect the expected shapes. In other words, the maximum flux density might be located at the corner of the receiver or the contours may not follow a reasonable pattern. This problem is clearly shown in Figure 3-5. Therefore, another algorithm, called self-modifying algorithm, needs to be developed to modify the flux density maps and turn them into more realistic shapes by changing the elements of the random matrices. In this program the ideal map is defined as the one in which the maximum flux density is located as close as possible to the center of the receiver and gradually decreases as it gets closer to the receiver sides. The algorithm developed to handle this task can be explained with the aid of Figure 3-6. The largest square represents the receiver surface and 81 aiming points are

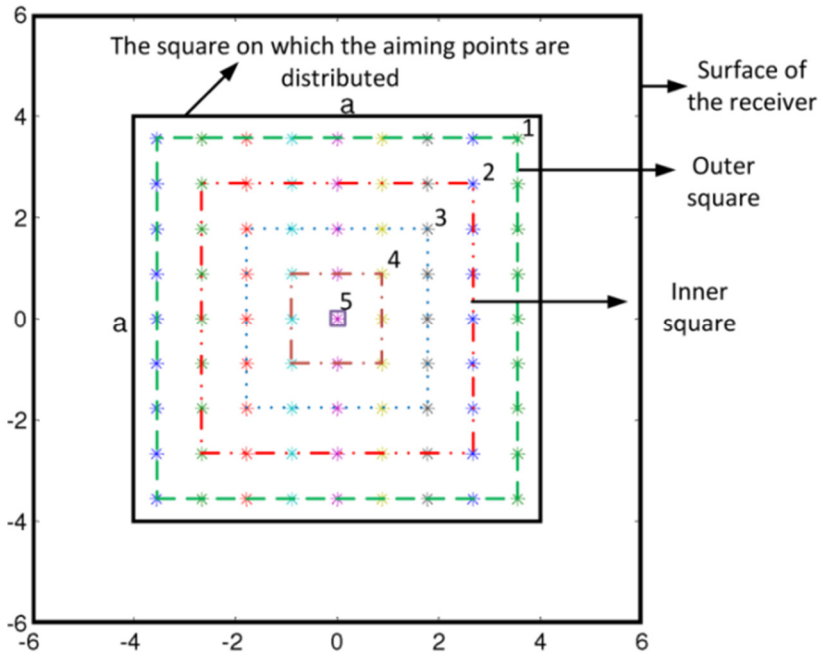


Figure 3-6 The receiver surface, aiming surface, and the generated squares

distributed on a smaller square, which is called aiming surface. The discussion about the size of this surface and the number of aiming points is presented later. As shown in Figure 3-6, the aiming points can be connected to each other to form new squares. Beginning from the squares #1 and #2 as the outer and inner squares, respectively, the flux densities for all the aiming points located on the sides are calculated. The maximum flux on the square #1 should be less than the minimum flux on the square #2. If this constraint is violated, one of the heliostats that are focused on the aiming point representing the maximum of square #1 is repositioned and is focused on the point having the minimum flux density of square #2. This algorithm continues until the flux density at all the points on square #1 becomes less than those on square #2. Next, the outer square is replaced by square #2 and the inner square is represented by square #3 and the process continues.

The flowchart for the algorithm is shown in Figure 3-7. During optimization, all the generated matrices are self-modified by this algorithm. The algorithm is applied to the flux map

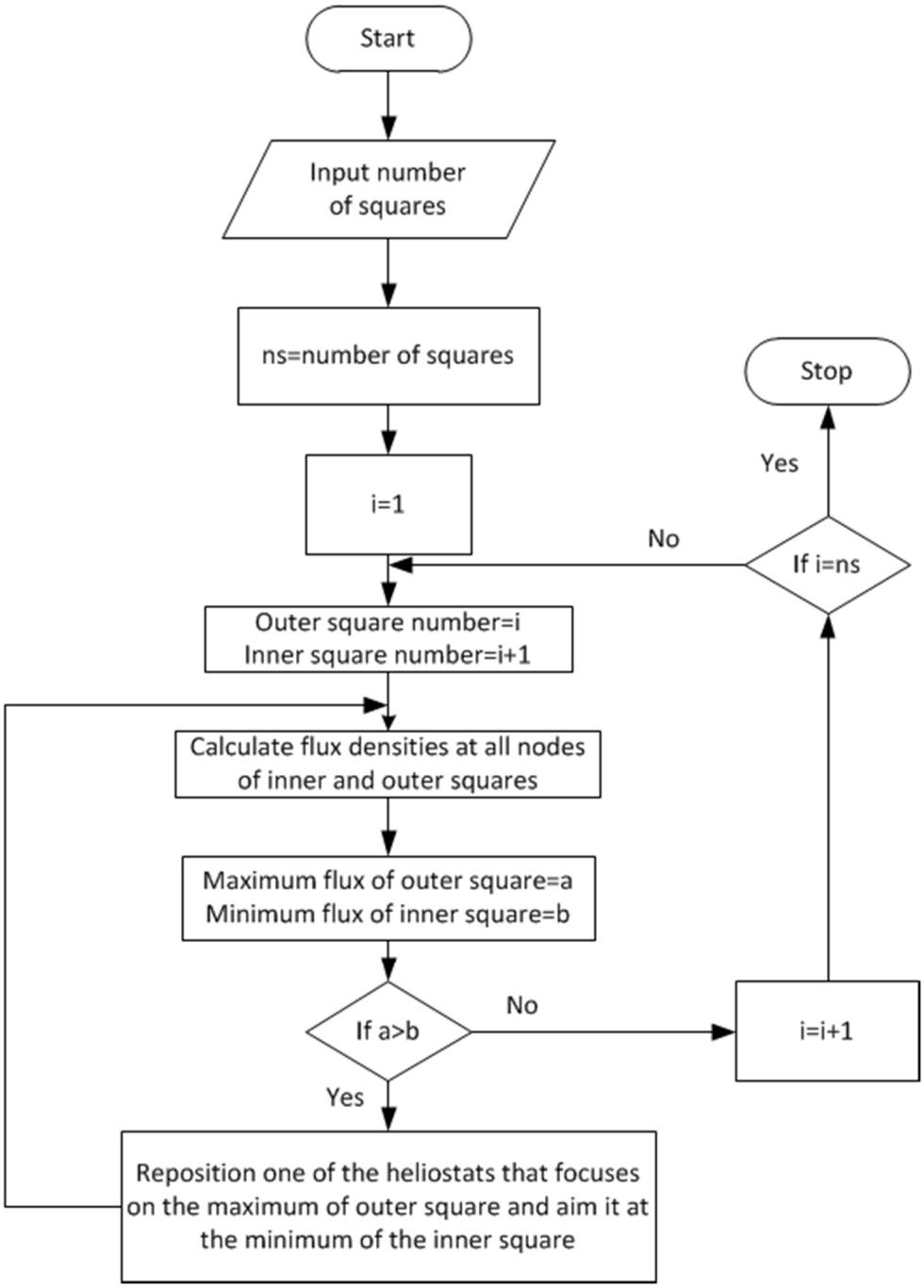


Figure 3-7 Flowchart for the self-modifying algorithm

shown in Figure 3-5. Figure 3-8 depicts how the flux density map is modified with the number of iterations. As can be seen, on the 24$^{th}$ iteration the maximum flux density is located at the center and gradually decreases until it reaches the minimum level close to the sides of the receiver.

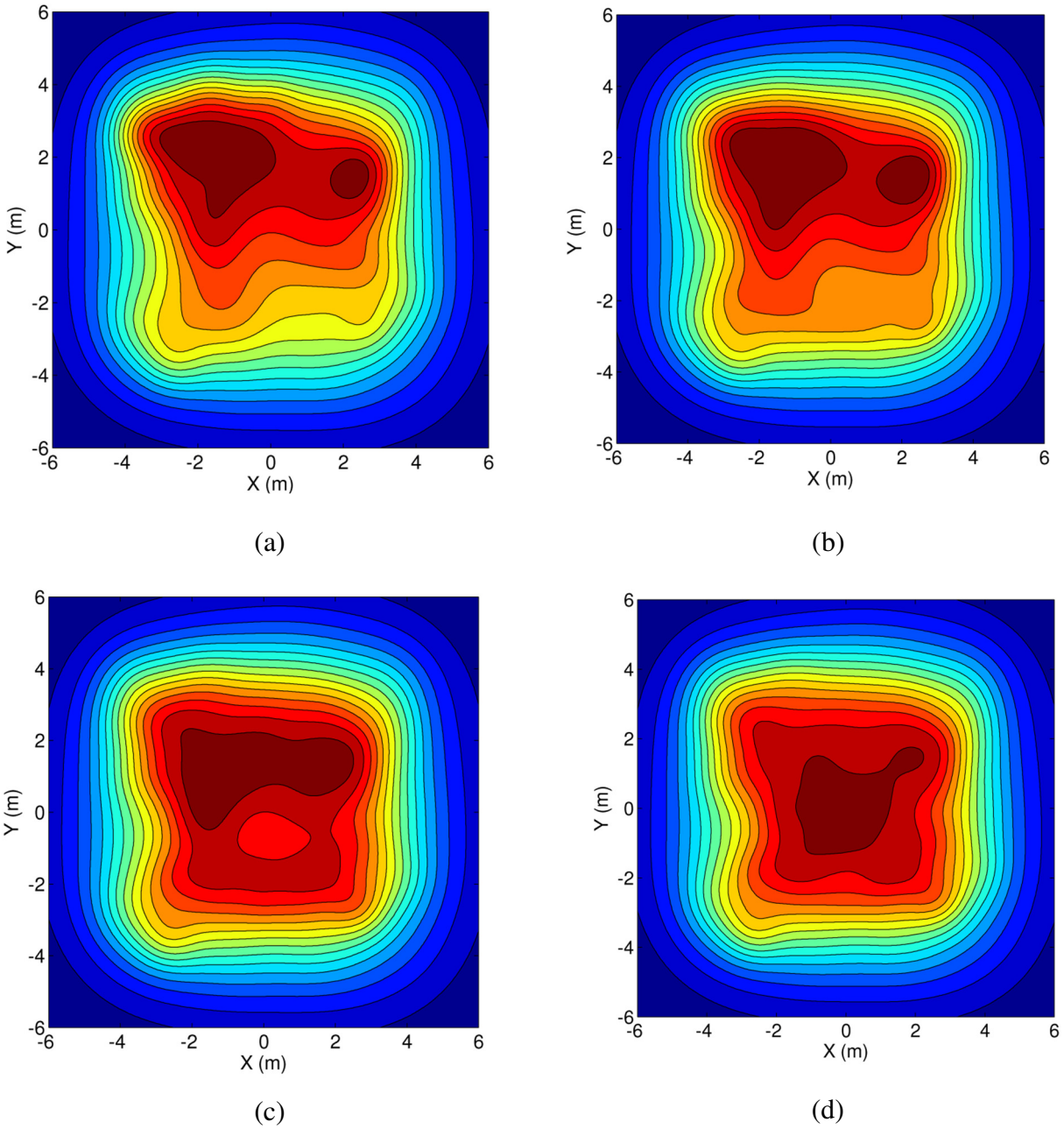


Figure 3-8 Modification of flux density map shown in Figure 3-5. (a) 3rd iteration (b) 8th iteration (c)16th iteration (d) 24th and the last iteration

### 3.4 Results and Discussion

#### 3.4.1 Optimization Results

As a case study, a field layout as shown in Figure 3-9 was designed for a 50$MW_{th}$ system in Daggett, California. There are 580 heliostats which are placed based on the biomimetic layout

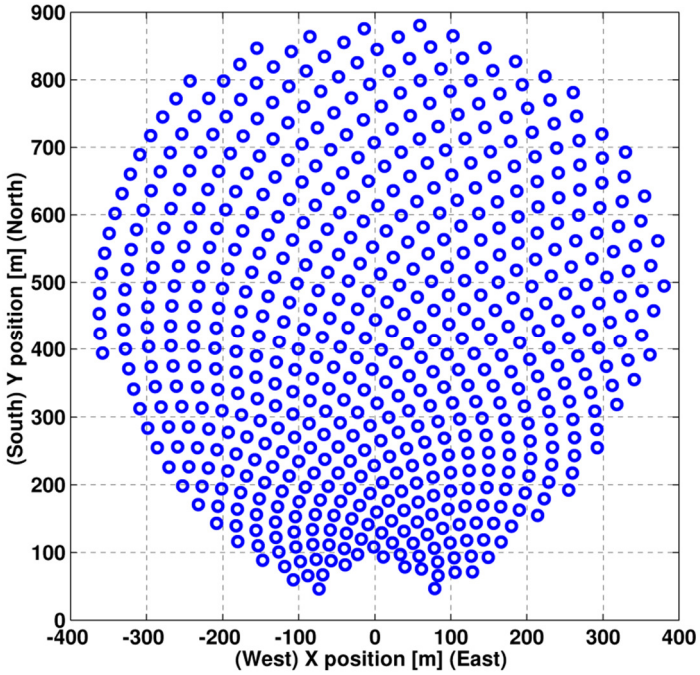


Figure 3-9 Heliostat field for a 50MWth solar power tower plant in Daggett, California

proposed by Noone et al [24]. This field and the methods explained in the preceding sections are employed to find the optimal flux density distribution on the receiver surface. Other field parameters are given in Table 3-1. It is assumed that $\sigma_{sun}$ is $2.51 \times 10^{-3}$mrad, $\sigma_s$ is $10^{-3}$mrad, the tracking error is negligible, and the facet canting is on-axis parabolic.

On March 21st at noon, the direct normal radiation in Daggett is given as 0.926 $\frac{kW}{m^2}$ [27]. Assuming all the heliostats aim at the center of the receiver at this time of the year, the flux density map using the HFLCAL method is shown in Figure 3-10.

As can be seen, the flux density at the center of the receiver is close to 5000 $\frac{\text{kW}}{\text{m}^2}$, which is extremely high. Therefore, an aiming strategy is required to uniformly distribute the flux over the surface. In this regard, a number of aiming points are distributed on the receiver surface, as shown in Figure 3-11. All of these points are located inside a square which is called the aiming surface.

Table 3-1 Solar power tower parameters

| *Heliostats* | |
|---|---|
| Width | 12.84 m |
| Height | 9.45 m |
| Reflectivity | 0.88 |
| *Receiver* | |
| Tower height | 115 m |
| Tilt angle of the aperture | 12.5° |
| Aperture width | 12 m |
| Aperture height | 12 m |

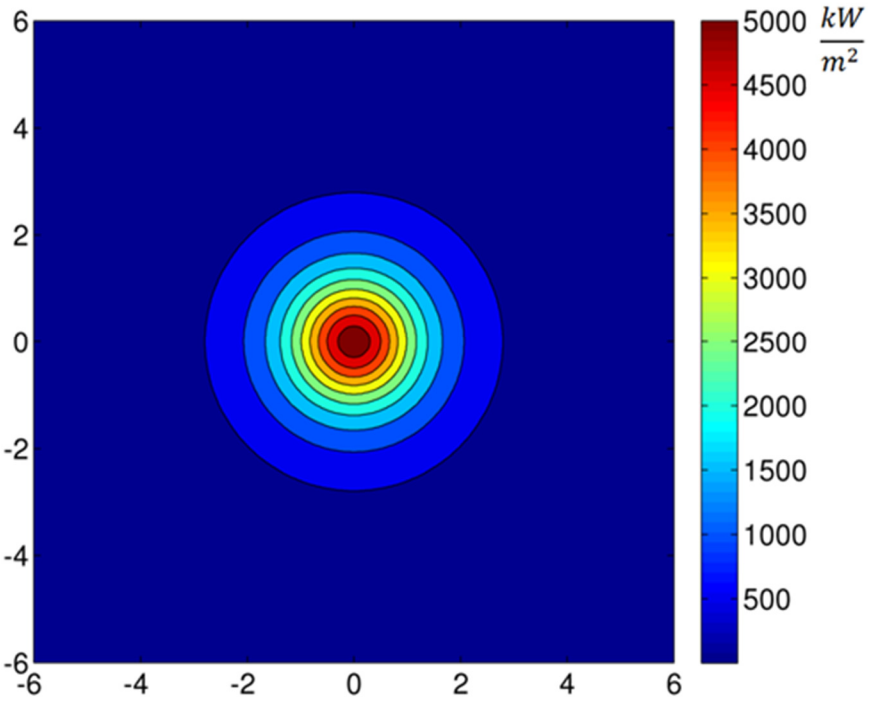


Figure 3-10 Flux density map for the solar power tower plant. All the heliostats are aimed at the center of the receiver.

Optimization algorithm is used to find the appropriate aiming point for each heliostat that leads to the least standard deviation of the flux density distribution on the entire surface. In this study, the aiming surface is a 8 × 8 square on which 81 aiming points are uniformly distributed. The evolutionary process of optimization is accomplished with a population size of 100 with crossover probability, $P_c$, mutation probability,$P_m$, and second mutation probability, $P_{mm}$, of 0.9,

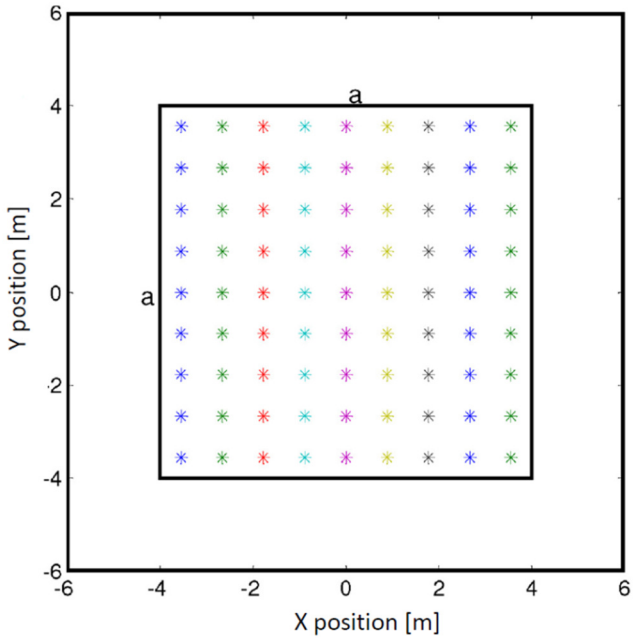


Figure 3-11 Distribution of the aiming points on the receiver surface

0.2, and 0.5 respectively. Figure 3-12 shows the variations of the objective function with the generation number. The optimization algorithm is terminated after 235 generations when the objective function reaches a plateau.

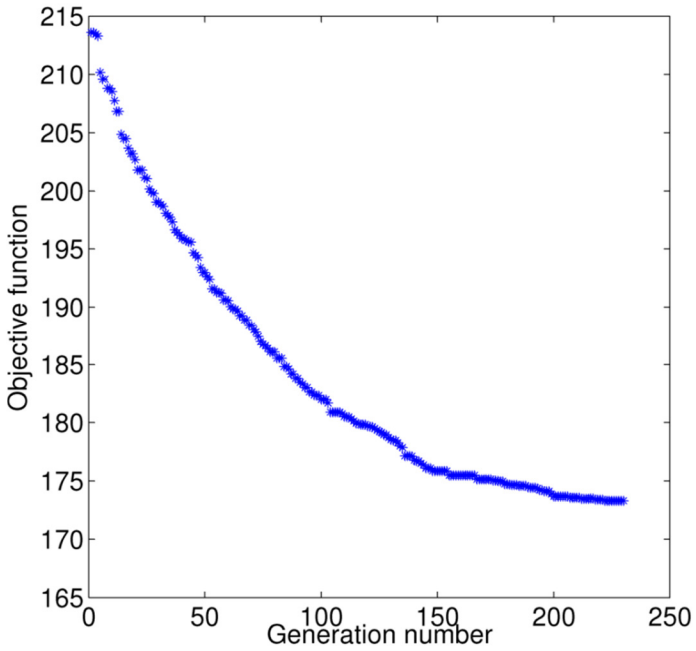


Figure 3-12 Variation of the objective function with the generation number

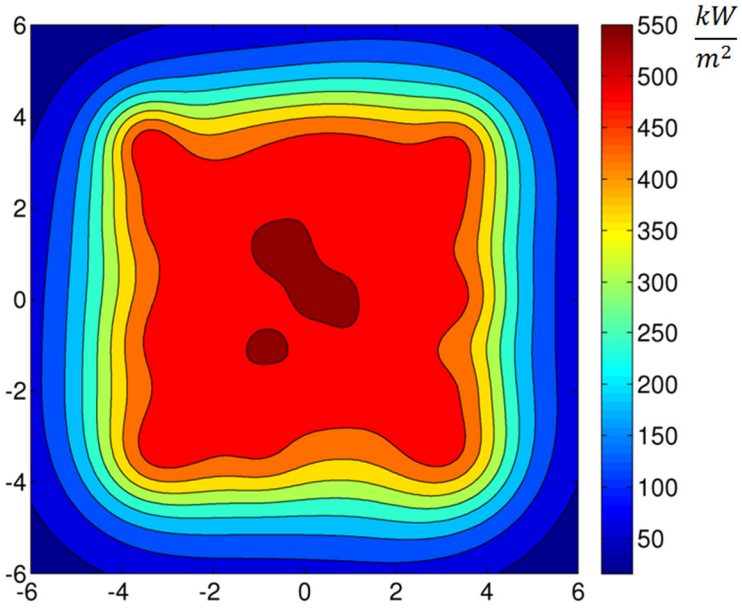


Figure 3-13 Optimal flux density distribution on the receiver surface

Figure 3-13 depicts the optimal flux distribution on the receiver surface. It can be seen that the maximum flux density is 550 $kW/m^2$, which is almost one tenth of the maximum flux when all the heliostats aim at the center of the receiver (Figure 3-10). Therefore, it can be concluded that the new algorithm is able to successfully distribute the flux on the entire surface.

The interception efficiency using the proposed aiming strategy is 0.9214 as opposed to 0.9906 in the original case. According to Figure 3-13 , there is a spot which is shown as dark red and is not located at the center of the surface. The reason is that the self-modifying algorithm is based on calculating and comparing the flux densities only at the aiming points. Therefore, there might be some points in between that cannot be captured by the algorithm. This is not a concern as long as the size of the spot is small. However, increasing the number of the aiming points can fix this problem, which is discussed in the following sections. A map of the heliostat field is presented in Figure 3-14 to show which heliostats were aimed at which points. The numbering for the aiming points begins from the bottom left corner in Figure 3-11 and ends at the top right.

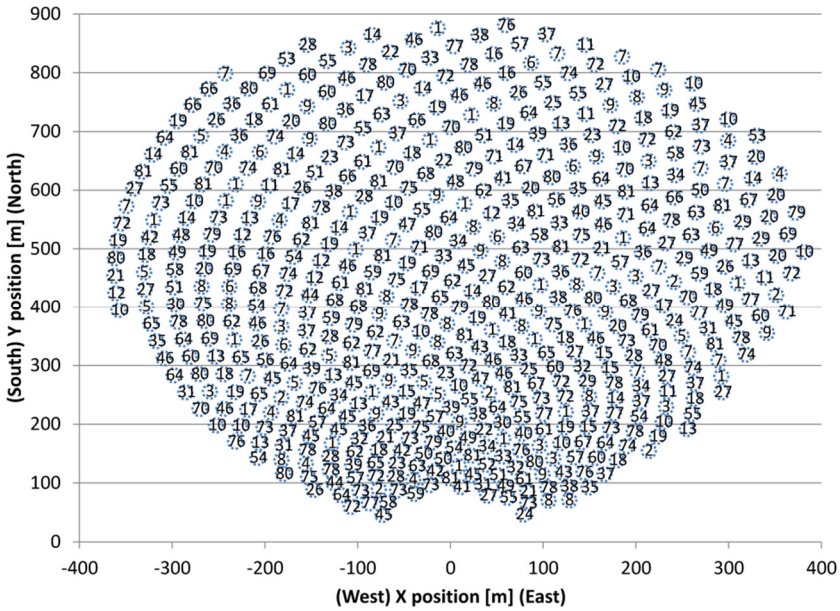


Figure 3-14 A map of the heliostat field with the information about the aiming points

### 3.4.2 Influence of the Aiming Surface Size

The size of the aiming surface is an important parameter which directly affects the flux density distribution as well as the interception efficiency. A smaller aiming surface leads to higher interception efficiency and higher maximum flux density, and vice versa. Figure 3-15 shows the variations of the interception efficiency and the maximum flux density with respect to the size of the aiming surface. In this case, the aiming surface is represented by a square on which 81 aiming points are distributed. The calculations were performed on March 21$^{st}$ for Daggett, California. As can be clearly seen from Figure 3-15, the smallest size of the aiming surface (5m×5m) has the highest interception efficiency and the maximum flux density increases to 1070 $kW/m^2$. As the size of the aiming surface increases to 12m ×12m, the interception efficiency decreases to 0.7533. This means that close to 25 percent of the energy reflected by the heliostats is lost and not intercepted by the receiver. This has a huge impact on the performance of the power plant. Therefore, one has to consider the maximum heat flux density that can be tolerated by the receiver surface and size the

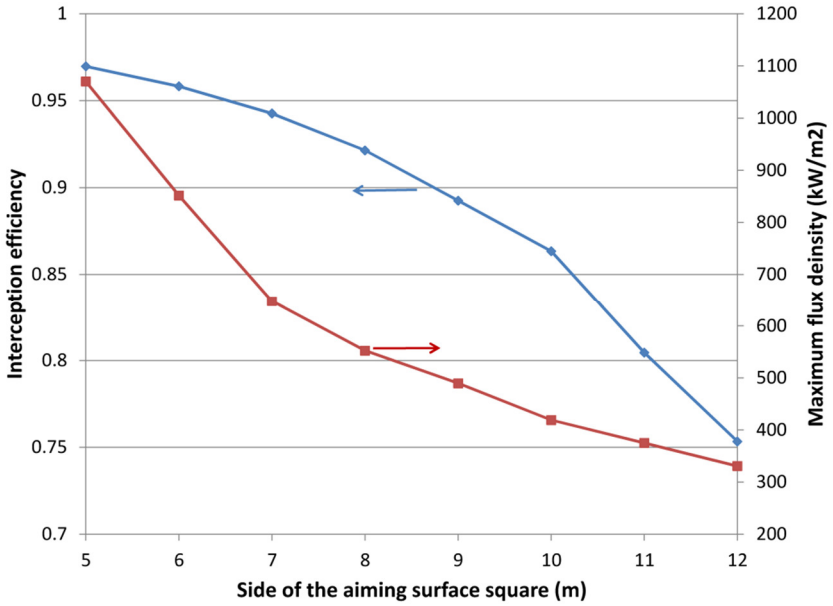


Figure 3-15 Variations of efficiency and flux density with the size of the aiming surface

aiming surface accordingly. It is noteworthy that by decreasing the size of the aiming surface, it might be necessary to decrease the number of aiming points as distributing a large number of aiming points on a small surface can be a challenge from practical point of view.

### 3.4.3 Influence of the Number of Aiming Points

Increasing the number of aiming points leads to a better distribution of the heat flux on the receiver surface. Moreover, the self-modifying algorithm is more efficient when a large number of aiming points is employed. However, in a real power plant the number of aiming points that can be distributed on a surface depends on the size of the surface and uncertainty in aiming the heliostats. Therefore, having a very large number of aiming points on a small receiver may not be practical nor necessary.

Figure 3-16 depicts the flux maps on the receiver surface when 49 and 121 aiming points are considered. All other parameters are same as those used in Figure 3-13. As can be clearly seen from the left plot, when there are 49 aiming points, the maximum flux density is located on the left corner

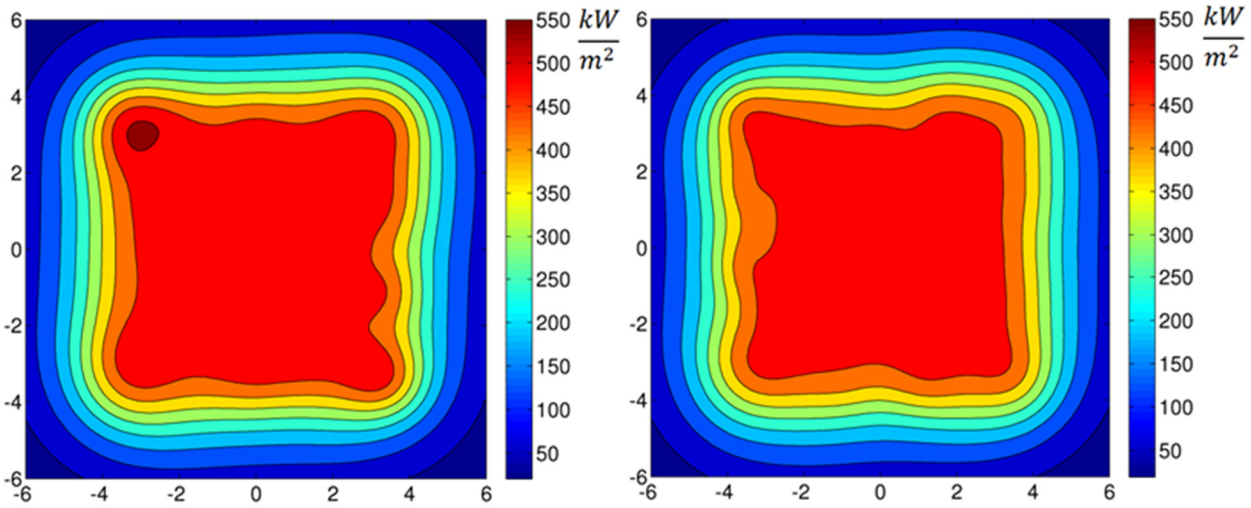


Figure 3-16 Optimal flux density distribution on the receiver surface. Left) 49 aiming points; Right) 121 aiming points

of the square. However, the size of this spot is small and the flux density on this point is not very different from its neighbors. Moreover, the flux density is well-distributed over the entire surface of the receiver. Therefore, it can be concluded that although the number of aiming points has decreased from 81 to 49, the algorithm is still able to distribute the flux very efficiently. The same analysis is carried out for 121 aiming points and the resulting flux map is shown on the right plot. According to the figure, there is no dark spot and the flux density is perfectly distributed on the surface and the maximum flux density is about 500 $\frac{kW}{m^2}$.From the results shown in this section, it can be concluded that it is desirable to have a larger number of aiming points from computational point view, even though the program is still able to distribute the flux efficiently using a smaller number of aiming points. The selection of the number of aiming points depends on the size of the receiver and uncertainties in aiming the heliostat.

### 3.5 Summary and Concluding Remarks

The work in this chapter presents an optimization algorithm that can be used to obtain uniform heat flux density distribution on the receiver surface of a solar power tower plant. The flux

density of individual heliostats was modeled using the HFLCAL method, which was validated against experimental data. The optimization code was developed based on the principles of GA and modified by considering the physics of the problem. The results showed that using the new algorithm the maximum flux density is reduced by a factor of 10, reaching around 500 $\frac{kW}{m^2}$. The analysis has shown that the size of the aiming surface has a huge impact on the interception efficiency and the maximum flux density and should be chosen as small as possible. This, of course, depends on the maximum flux density that the receiver material can tolerate. Moreover, it is shown that the algorithm works very well for different numbers of aiming points, however, it is desirable to increase this number as much as possible. It is noteworthy that in this chapter the heliostats are modeled as single mirrors, but the algorithm would also be applicable if the heliostats were represented by different facets.

# CHAPTER 4 THERMAL ANALYSIS OF CAVITY TYPE SOLAR RECEIVER

## 4.1 Introduction

Thermal receiver is the heart of a solar power plant where the concentrated solar energy received from the solar field is converted into thermal energy and transferred to the HTF. Any heat loss from the receiver reduces the available energy to the HTF and consequently, influences the performance of the power plant.

There are different types of thermal receivers that are well documented in [59]. Among these receivers, external and cavity type receivers have been extensively used in the commercial power plants.

An external receiver consists of vertical panels that form a cylindrical shape and is placed atop a tower (Figure 4-1, left). The panels are exposed to the environment resulting in high convective and radiative heat losses. However, the cylindrical shape of the receiver accommodates a heliostat field with 360° azimuth angle.

On the other hand, in a cavity type receiver the panels are placed inside a cavity in order to reduce the heat losses (Figure 4-1, right). However, geometry of the receiver limits the layout of the field to a portion of the azimuthal angles.

In this dissertation, only a cavity type receiver is studied because of its higher thermal efficiency. In this chapter, a detailed thermal model for a cavity receiver is developed to estimate the heat losses and thermal efficiency. The thermal model consists of convective and radiative heat

Figure 4-1 Left) External receiver of Solar Two plant. Right) Cavity receiver of PS10 plant

transfer mechanisms. The convective model is based on the work introduced by [60] [61] while the radiative model follows the approach presented by [62].

**4.2 Convective Heat Loss**

Convective heat transfer from a cavity receiver to the environment is a complex problem which has been studied for a long time. It can be divided into two mechanisms, i.e. natural and forced convection.

In natural convection, the buoyancy forces, which are due to density differences, induce the flow. On the other hand, in forced convection the flow is generated by external means such as wind [63]. Once the heat transfer coefficients for both mechanisms are known, the combined convective heat transfer coefficient can be found as [64]:

$$h_c = h_{nc} + h_{fc} \tag{4-1}$$

According to a study done by [65] for a cavity receiver with the wall temperatures in the range of 800-1500 K, natural convection is the dominant mechanism when the wind speed is below 5

m/s. Mixed convection has to be considered for wind speeds between 6-20 m/s, while forced convection is the dominant regime when wind speeds exceed 25 m/s.

4.2.1 Natural Convection

Although there are a number of correlations that have been proposed for cavity receivers, most of them are suitable for small dimensions and cannot be confidently used for large cavity receivers. However, the model presented by Clausing [60] [61] has been extensively used in the literature and can be considered as the most-reliable method so far. The model is based on the network resistance model which is shown in Figure 4-2.

The air is stagnant in the upper region of the cavity because of its high relative density; therefore, this area is called stagnant zone and separated from the convective zone by the shear layer. The bulk air temperature is obtained by:

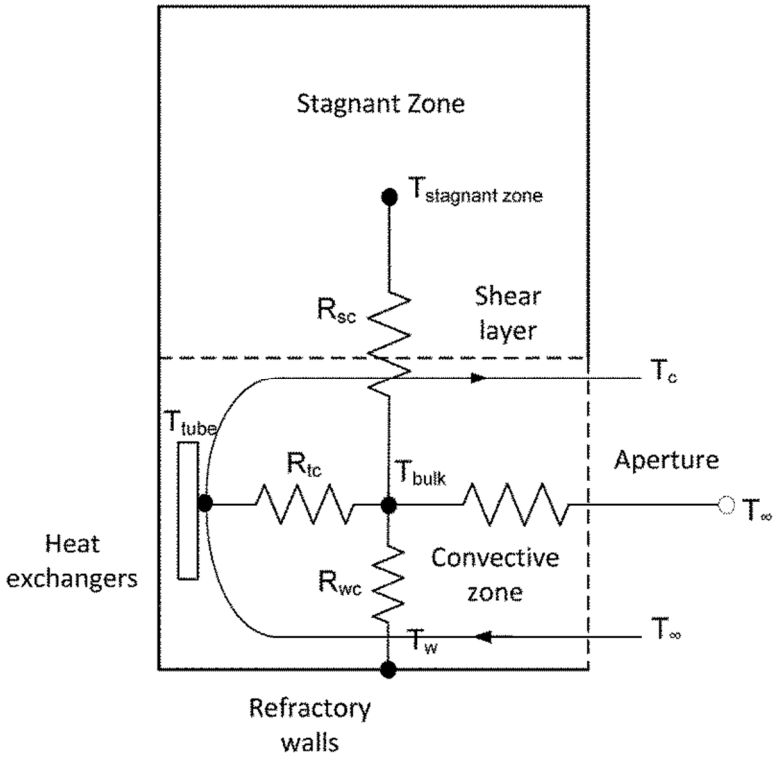


Figure 4-2 Network representation of natural heat loss mechanism (adapted from [60])

$$T_{bulk} = \frac{T_c + T_\infty}{2} \tag{4-2}$$

where $T_c$ is the temperature of the air leaving the cavity, and $T_\infty$ is the ambient temperature.

The convective energy leaving the aperture can be found by:

$$Q_{aperture} = (\rho_\infty V_a A_a) c_p (T_c - T_\infty) \tag{4-3}$$

where $\rho_\infty$ is the density of the air, $A_a$ is the aperture area through which mass flows into the cavity, and $c_p$ is the specific heat. In the above equation, $V_a$ is the average velocity of mass flux that is given by:

$$V_a = 0.5[(C_3 V_b)^2 + (C_4 V_{wind})^2\ ]^{0.5} \tag{4-4}$$

where $V_{wind}$ is the wind velocity and $V_b$ is the characteristic velocity due to buoyancy that can be found by:

$$V_b = [g\ \beta (T_c - T_\infty) L_a]^{0.5} \tag{4-5}$$

In this equation $g$ is the acceleration of gravity, $\beta$ is the volumetric coefficient of expansion, and $L_a$ is the projected height of the aperture in the vertical plane. The coefficients $C_3$ and $C_4$ are taken as 1 and 0.5 in this study [61], unless otherwise noted. Using the resistance network model shown in Figure 4-2, the convective heat loss inside the cavity is given as:

$$Q_{conv} = \frac{T_{tube} - T_{bulk}}{R_{tc}} + \frac{T_w - T_{bulk}}{R_{wc}} + \frac{T_{stagnant\ zone} - T_{bulk}}{R_{sc}} \tag{4-6}$$

This equation can also be written as:

$$Q_{conv} = h_t A_t (T_{tube} - T_{bulk}) + h_w A_w (T_w - T_{bulk}) + h_s A_s (T_{stagnant\ zone} - T_{bulk}) \tag{4-7}$$

It is assumed that all the heat transfer coefficients in this equation are equal and can be estimated by [61]:

$$Nu = 0.082\ Ra^{1/3} \left[ -0.9 + 2.4 \left( \frac{T_w}{T_\infty} \right) - 0.5 \left( \frac{T_w}{T_\infty} \right)^2 \right] z(Z_w) \tag{4-8}$$

Table 4-1 Verifying the program developed for calculating natural convective heat loss

| | Clausing 1981 [60] | This study |
|---|---|---|
| *1 $MW_{th}$ receiver* | | |
| $T_c$(℃) | 151 | 150.26 |
| $h$ ($\frac{W}{m^2K}$) | 5.9 | 5.86 |
| *38 $MW_{th}$ receiver* | | |
| $T_c$(℃) | 103 | 102.44 |
| $h$ ($\frac{W}{m^2K}$) | 7.8 | 7.74 |

$$Ra > 1.6 \times 10^9; 1 < \frac{T_w}{T_\infty} < 2.6$$

where $Ra$ is the Raleigh number, which is the product of Grashof and Prandtl numbers [63]. The properties are calculated at film temperature that is the average of the wall and bulk temperatures. The temperature ratio is recommended to be replaced by the value of 2 when it is higher than 2.6 [61].

In the previous equation, $Z_w$ is the wall zenith angle and $z(Z_w)$ is:

$$z(Z_w) = 1, \quad 0 \leq Z_w \leq 135 \text{ degree}$$

$$z(Z_w) = 2/3\left[1 + (sinZ_w)/\sqrt{2}\,\right], \; Z_w > 135 \text{ degree} \tag{4-9}$$

The set of presented equations needs to be solved to find $Q_{conv}$ and $T_c$. In other words, the objective is to find a value for $T_c$ that leads to $Q_{conv} = Q_{aperture}$.

In order to validate the program developed in this study, the convective heat loss and the other relevant parameters are calculated for the two case studies presented in [60]: a 38 $MW_{th}$ and a 1 $MW_{th}$ receiver with 20 and 0.5 $m^2$ aperture areas, respectively. Table 4-1 compares the results and demonstrates that the program predicts accurate values.

4.2.2 Forced Convection

As it is stated previously, forced convection needs to be taken into account when the wind speed exceeds 5 m/s. The main concern is that there is no correlation in the literature that is widely accepted to estimate forced convection heat transfer coefficient. Teichel [62] suggested the correlation proposed by Kays et. al [66] to approximate the influence of wind on convective losses which is given as:

$$Nu_{forced} = 0.0287\ Re^{0.8}\ Pr^{1/3} \tag{4-10}$$

where all the properties are calculated at the average of the ambient and wall temperatures.

**4.3 Radiative Heat Loss**

Radiative heat transfer is the main source of energy loss in the receivers of solar power tower plants. A part of this loss is associated with the large temperature difference between the receiver walls and ambient while the other part is due to the reflection of solar flux from the absorbing surfaces. The radiation model presented in this chapter is described in [65] [67] and is already employed in TRNSYS [68], a well-known energy simulation software package.

4.3.1 Radiative Heat Transfer Between Black Surfaces

The radiation that leaves a black surface $i$ and impinges directly on surface $j$ is given as [63]:

$$Q_{therm,ij} = F_{ij} A_i \sigma T_i^4 \tag{4-11}$$

where $A_i$ is the surface area, $\sigma$ is the Stefan-Boltzmann constant, and $T$ is the temperature in Kelvin. In this equation $F_{ij}$ is the view factor that is defined as:

$$F_{ij} = \frac{\text{radiation leaving surface } i \text{ that directly hits surface } j}{\text{total radiation leaving surface } i} \tag{4-12}$$

The net radiation between the two surfaces is given as:

$$Q_{net,therm,ij} = F_{ij} A_i \sigma (T_i^4 - T_j^4) \tag{4-13}$$

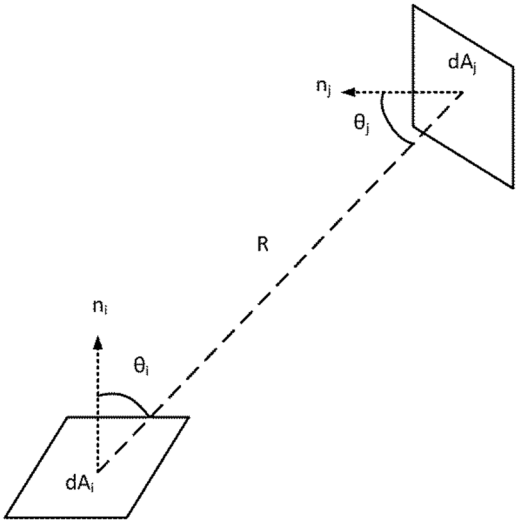


Figure 4-3 Radiation exchange between two surfaces

where:

$$F_{ij}A_i = F_{ji}A_j \tag{4-14}$$

The view factor between two surfaces can be found using analytical and numerical approaches that are described in the subsequent sections.

*4.3.1.1 Analytical Approach for Finding the View Factor*

The view factor between surfaces $i$ and $j$ shown in Figure 4-3 can be obtained by [63]:

$$F_{ij} = \frac{1}{A_i}\int_{A_i}\int_{A_j}\frac{\cos\theta_i \cos\theta_j}{\pi R^2}\, dA_i\, dA_j \tag{4-15}$$

For an enclosure with $N$ surfaces, the summation rule can be applied:

$$\sum_{j=1}^{N} F_{ij} = 1 \tag{4-16}$$

A large number of view factors for two-dimensional and three-dimensional geometries are provided by Siegel and Howell [69]. Gross et al. [70] developed an analytical approach to find the view factor between rectangular surfaces of arbitrary position and size with parallel boundaries, which is given as:

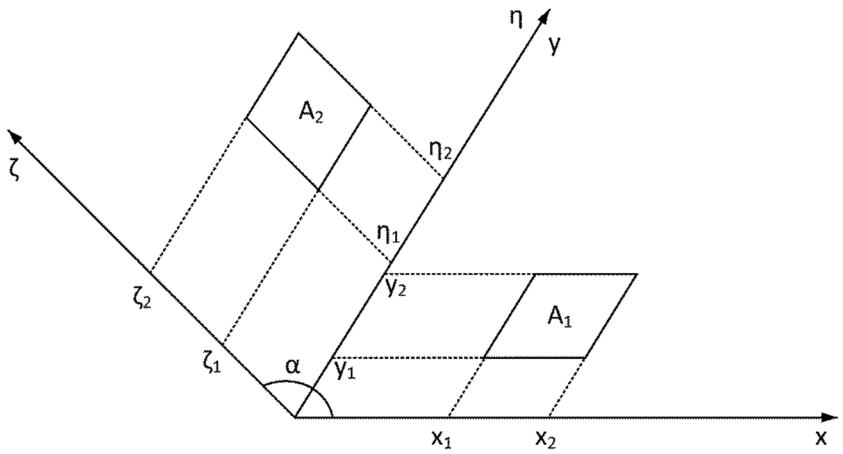


Figure 4-4 Two rectangular surfaces inclined at an arbitrary angle

$$F_{1-2} = \frac{1}{A_1}\sum_{k=1}^{2}\sum_{j=1}^{2}\sum_{i=1}^{2}\left[(-1)^{(i+j+k)}G(x_i, y_i, \eta_k)\right] \tag{4-17}$$

where

$$G = -\frac{\sin^2\alpha\,(\eta - y)}{2\pi}\int_{\zeta}\left[\frac{\cos\alpha\,(x - \zeta\cos\alpha) - \zeta\sin^2\alpha}{\sin^2\alpha\;(x^2 - 2\,x\,\zeta\cos\alpha + \zeta^2)^{\frac{1}{2}}}\tan^{-1}\left[\frac{\eta - y}{(x^2 - 2\,x\,\zeta\cos\alpha + \zeta^2)^{\frac{1}{2}}}\right]\right.$$
$$+\frac{\cos\alpha}{\sin^2\alpha\,(\eta - y)}\left[[\zeta^2\sin^2\alpha + (\eta - y)^2]^{\frac{1}{2}}\tan^{-1}\left[\frac{x - \zeta\cos\alpha}{(\zeta^2\sin^2\alpha + (\eta - y)^2)^{\frac{1}{2}}}\right]\right.$$
$$\left.\left. - \zeta\sin\alpha\tan^{-1}\left[\frac{x - \zeta\cos\alpha}{\sin\alpha}\right]\right]\right.$$
$$\left. + \frac{\zeta}{2\,(\eta - y)}\ln\left[\frac{x^2 - 2x\zeta\cos\alpha + \zeta^2 + (\eta - y)^2}{x^2 - 2x\zeta\cos\alpha + \zeta^2}\right]\right] d\zeta \tag{4-18}$$

These equations can be employed to find the view factors between the rectangular panels, surfaces, and opening inside the cavity.

*4.3.1.2 Numerical Approach for Finding the View Factor*

Depending on the shape and relative position of the surfaces, an analytical solution for finding the view factor may not be possible. In this case, a numerical approach, which is called Monte Carlo Ray Tracing method [67] [71], is applied to find the view factor.

In this method, a large number of rays with random directions is generated from a radiating surface $i$. Each ray is individually tracked and the number of rays that hit the surface $j$ is determined. The view factor, $F_{ij}$, is then determined as:

$$F_{ij} = \frac{\text{number of rays that hit surface } j}{\text{total number of rays generated from surface i}} \tag{4-19}$$

The ray direction is determined using the probability distributions given as [67]:

$$P_\theta = \sin^2 \theta \tag{4-20}$$

$$P_\phi = \frac{\phi}{2\pi} \tag{4-21}$$

where $P_\theta$ and $P_\phi$ are random numbers between 0 and 1. A program is developed in MATLAB to calculate the view factors between the surfaces in a cavity receiver using analytical and Monte Carlo Tracing approaches. The programs are verified against the results provided by Feierabend [71] for a cavity receiver shown in Figure 4-5.

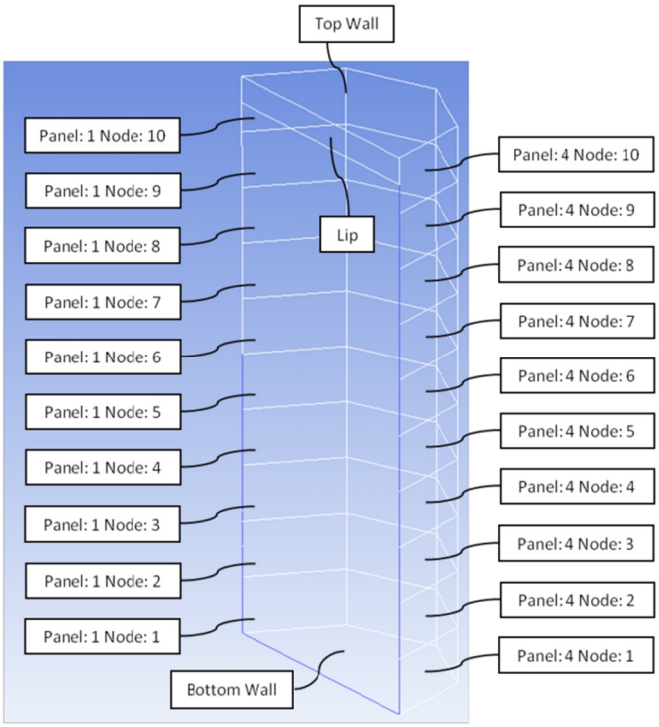


Figure 4-5 Surface description of the receiver configuration developed by Feierabend [71]

Table 4-2 Comparison of the calculated view factors with those given by Feierabend [71]

| Emitting surface | | Target surface | | Feierabend [71] | This study |
|---|---|---|---|---|---|
| Node | Panel | Node | Panel | | |
| Aperture | | Bottom wall | | 0.063 | 0.063 |
| Aperture | | Top wall | | 0.043 | 0.043 |
| Bottom wall | | Top wall | | 0.022 | 0.024 |
| Lip | | Bottom wall | | 0.002 | 0.002 |
| Lip | | Top wall | | 0.391 | 0.391 |
| 10 | 1 | Aperture | | 0.3064 | 0.3060 |
| 10 | 1 | Bottom wall | | 0.0046 | 0.0046 |
| 10 | 1 | Lip | | 0.1396 | 0.1392 |
| 10 | 1 | Top wall | | 0.3048 | 0.3058 |
| 9 | 1 | Aperture | | 0.5163 | 0.5154 |
| 9 | 1 | Bottom wall | | 0.0062 | 0.0061 |
| 9 | 1 | Lip | | 0.0306 | 0.0306 |
| 9 | 1 | Top wall | | 0.1422 | 0.1420 |
| 8 | 1 | Aperture | | 0.5649 | 0.5640 |
| 8 | 1 | Bottom wall | | 0.0085 | 0.0084 |
| 8 | 1 | Lip | | 0.0100 | 0.0100 |
| 8 | 1 | Top wall | | 0.0768 | 0.775 |
| 7 | 1 | Aperture | | 0.5809 | 0.5800 |
| 7 | 1 | Bottom wall | | 0.0123 | 0.0122 |
| 7 | 1 | Lip | | 0.0041 | 0.0041 |
| 7 | 1 | Top wall | | 0.0450 | 0.0447 |
| 6 | 1 | Aperture | | 0.5867 | 0.5858 |
| 6 | 1 | Bottom wall | | 0.0180 | 0.0178 |
| 6 | 1 | Lip | | 0.0019 | 0.0019 |
| 6 | 1 | Top wall | | 0.0279 | 0.0281 |

It can be confidently concluded from the results presented in Table 4-2 that the program can predict accurate values. The numbers in the last column in blue, black, and red are obtained using ray tracing method, analytical integration, and view factor relations, respectively.

### 4.3.2 Radiative Heat Transfer Between Non-Black (Gray) Surfaces

The heat flux that is released from a non-black surface, i.e. gray surface, is less than the radiation that is emitted from a black surface at the same temperature. Therefore emissivity ($\varepsilon$) has to be taken into account, which provides a measure of how efficiently a surface radiates energy relative

to a blackbody. Consequently, the total radiation leaving a gray surface $i$ and directly absorbed by surface $j$ is given as:

$$Q_{therm,ij} = \varepsilon_i F_{ij} A_i \sigma T_i^4 \alpha_j \tag{4-22}$$

where $\alpha$ is the surface absorptivity. The emissivity of a diffuse gray surface, i.e. the surface from which the intensity of radiation emitted is independent of the direction [63], is equal to its absorptivity for a given wavelength:

$$\varepsilon_{i,\lambda} = \alpha_{i,\lambda} \tag{4-23}$$

Moreover,

$$\varepsilon_{i,\lambda} + \rho_{i,\lambda} + \tau_{i,\lambda} = 1 \tag{4-24}$$

where $\rho_{i,\lambda}$ and $\tau_{i,\lambda}$ represent reflectivity and transmissivity of surface $i$ for a given wavelength. For an opaque surface, the transmissivity term is equal to zero.

When the gray surfaces are placed inside an enclosure, the energy can also be indirectly transferred between the surfaces through reflection as shown in Figure 4-6. As can be clearly seen, surface $j$ receives radiation from surface $i$ directly as well as indirectly, through reflection from surfaces $k_1$ and $k_2$. On the other hand, the definition of view factor that is given by equation (4-12) only takes direct radiation between the surfaces into account. Therefore, an alternative parameter

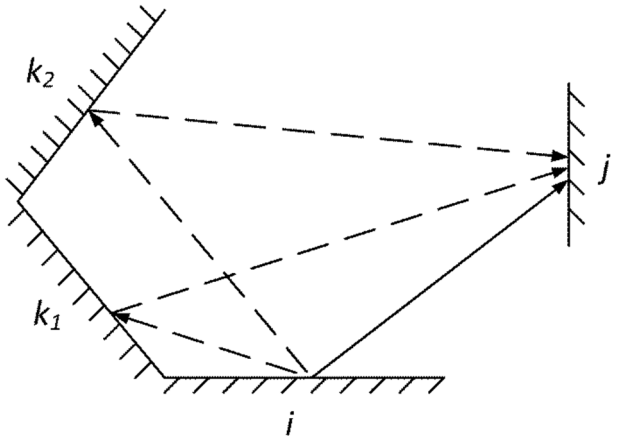


Figure 4-6 Radiative heat transfer between gray surfaces inside an enclosure

needs to be considered for gray surfaces which is called F-hat ($\hat{F}$) factor [67] [72] :

$$\hat{F}_{ij} = \frac{radiation\ leaving\ surface\ i\ that\ directly\ or\ indirectly\ hits\ surface\ j}{total\ radiation\ leaving\ surface\ i} \quad (4\text{-}25)$$

The $\hat{F}$ parameter that is dependent on the reflectivity of surfaces as well as the view factors between all the surfaces can be found as:

$$\hat{F}_{ij,\lambda} = F_{ij} + \sum_{k=1}^{n} F_{ik}\,\rho_{k,\lambda}\,\hat{F}_{kj,\lambda} \quad (4\text{-}26)$$

The first term in the right side of the equation represents the direct radiation between surfaces $i$ and $j$. The second term defines the fraction of the radiation leaving surface $i$ that hits other surfaces, reflected, and finally falls on surface $j$. Therefore, the net radiative heat transfer between the gray surfaces $i$ and $j$ is given as:

$$Q_{net,therm,ij} = \alpha_j\left(\varepsilon_i A_i \hat{F}_{ij}\sigma T_i^4\right) - \alpha_i(\varepsilon_j A_j \hat{F}_{ji}\sigma T_j^4) \quad (4\text{-}27)$$

where $\alpha$ is absorptivity and represents the fraction of the energy that is absorbed by the surface. Applying the reciprocity rule and using equation (4-23) results in:

$$Q_{net,therm,ij} = \varepsilon_i\varepsilon_j A_i \hat{F}_{ij}\sigma\left(T_i^4 - T_j^4\right) \quad (4\text{-}28)$$

4.3.3 Radiative Heat Transfer Inside a Cavity Receiver

As it is stated earlier in this chapter, a part of the radiative heat transfer inside a cavity receiver is associated with the reflection of incoming solar radiation. Assuming that surface $i$ receives a heat flux from the heliostat field, the energy that is received by surface $j$ due to reflection is given as:

$$Q_{solar,ij} = Flux_{solar,i}\,\rho_i\,\hat{F}_{ij}A_i\alpha_j = Flux_{solar,i}\,(1-\varepsilon_i)\,\hat{F}_{ij}A_i\varepsilon_j \quad (4\text{-}29)$$

Therefore, the net radiative heat transfer between surfaces $i$ and $j$ due to the reflected heat flux is obtained as:

$$Q_{net,solar,ij} = Flux_{solar,i}\,(1-\varepsilon_i)\,\hat{F}_{ij}A_i\varepsilon_j - Flux_{solar,j}\,(1-\varepsilon_j)\,\hat{F}_{ij}A_i\varepsilon_i \qquad (4\text{-}30)$$

that can be re-written as:

$$Q_{net,solar,ij} = \hat{F}_{ij}A_i\left(Flux_{solar,i}(1-\varepsilon_i)\varepsilon_j - Flux_{solar,j}(1-\varepsilon_j)\varepsilon_i\right) \qquad (4\text{-}31)$$

Equations(28-4) and (4-31) together represent the overall net radiative heat transfer between two surfaces inside a cavity receiver:

$$Q_{net,ij} = \varepsilon_i\varepsilon_j A_i\hat{F}_{ij}\sigma\left(T_i^4 - T_j^4\right) + \hat{F}_{ij}A_i\left(Flux_{solar,i}(1-\varepsilon_i)\varepsilon_j - Flux_{solar,j}(1-\varepsilon_j)\varepsilon_i\right) \qquad (4\text{-}32)$$

It is noteworthy that for the inactive surfaces, i.e. those that do not receive heat flux directly from the heliostat field, the term $Flux_{solar}$ is equal to zero. The net radiation to surface $i$ can be obtained by summing the equation (4-32) for every surface $j$ in the cavity:

$$Q_{net,i} = \varepsilon_i A_i\sum_{j=1}^{N}\varepsilon_j\hat{F}_{ij}\sigma\left(T_i^4 - T_j^4\right) + A_i\sum_{j=1}^{N}\hat{F}_{ij}\left(Flux_{solar,i}(1-\varepsilon_i)\varepsilon_j - Flux_{solar,j}(1-\varepsilon_j)\varepsilon_i\right) \qquad (4\text{-}33)$$

*4.3.3.1 Semi-gray Surface Model*

The performance of a receiver can be enhanced by applying surface coatings to increase absorptivity in the solar band (short wavelength radiation) and reduce emissivity in the thermal band (long wavelength radiation) [73].

In this dissertation, the two-band approximation model developed by Teichel [72] is employed to simulate the effect of surface coating on radiative heat transfer.

The reduced blackbody emissive power for a given temperature and wavelength can be obtained as:

$$E_{b,reduced} = \frac{C_1\left[\lambda^5\left(\exp(\frac{C_2}{\lambda T}) - 1\right)\right]^{-1}}{\sigma T^4} \qquad (4\text{-}34)$$

where $C_1$ and $C_2$ are 3.742e8 $\mathrm{W}-\mu\mathrm{m}^4/\mathrm{m}^2$ and 14388 $\mu\mathrm{m}-\mathrm{K}$, respectively.

Figure 4-7 depicts variations of this parameter with respect to wavelength for different temperatures. The sun temperature is taken as 5800 $K$. As can be clearly seen, solar energy is considered as short- wavelength radiation while hot objects radiate energy in the long-wavelength

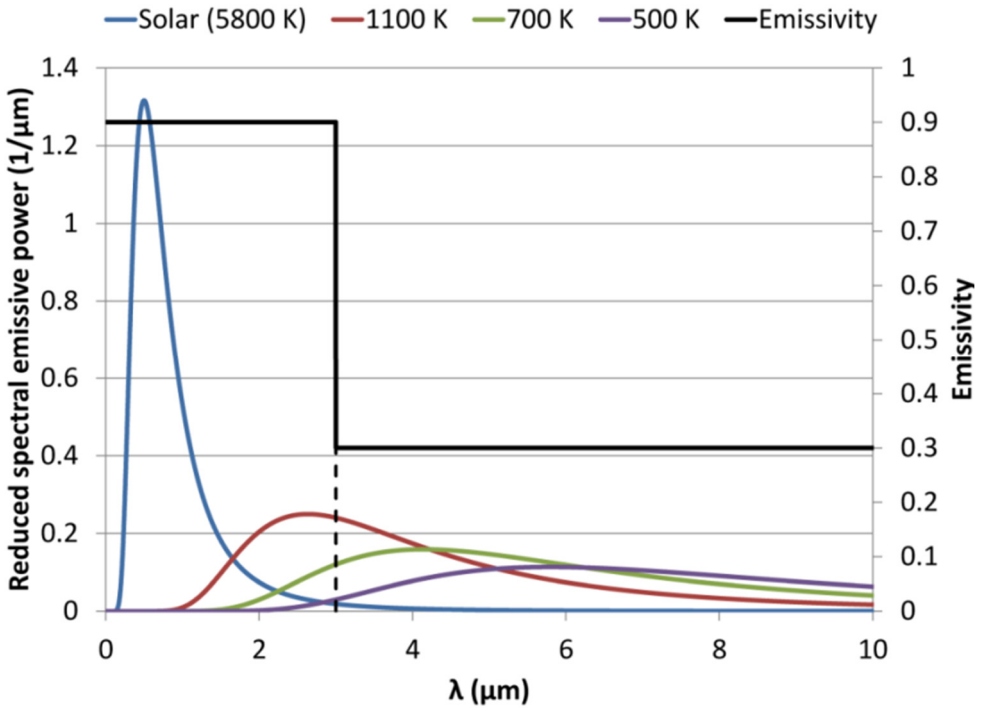


Figure 4-7 Two band model represented by two emissivity values

range. Therefore, thermal performance of the receiver can be improved by applying a coating with high absorptivity at short wavelengths and low emissivity at long wavelengths. In this figure, the emissivity drastically changes at $3\mu m$, but this parameter that is represented by $\lambda_{step}$ in this study can be varied to find the optimum value.

Fraction of radiation in a wavelength band from 0 to $\lambda_{step}$ can be found by [72]:

$$f_{0-\lambda_{step},T} = \int_0^{\lambda_{step}} \frac{C_1}{\sigma T^4 \lambda \left(\exp\left(\frac{C_2}{\lambda T}\right) - 1\right)} d\lambda \tag{4-35}$$

$f_{0-\lambda_{step},T}$ is an important factor to find the fraction of solar or thermal radiation that is associated with the high emissivity. Table 4-3 presents this parameter for the sun as well as other temperatures when $\lambda_{step}$ is taken as $3\mu m$. By considering the two-band model, the net thermal radiation heat transfer between surfaces $i$ and $j$ can be written as:

Table 4-3 Fraction of solar or thermal radiation within a particular wavelength band (0-3$\mu m$)

| | |
|---|---|
| $f_{0-\lambda_{step},T_{sun}}$ | 97.91% |
| $f_{0-\lambda_{step},T_{1100\ K}}$ | 34.01% |
| $f_{0-\lambda_{step},T_{700\ K}}$ | 8.31 % |
| $f_{0-\lambda_{step},T_{500\ K}}$ | 1.28 % |

$$Q_{net,therm,ij} = \left[\left(1 - f_{0-\lambda_{step},T_i}\right)\left(\alpha_{j,therm}\,\varepsilon_{i,therm} A_i \hat{F}_{ij,therm}\sigma T_i^4\right)\right.$$
$$\left. + f_{0-\lambda_{step},T_i}\left(\alpha_{j,solar}\varepsilon_{i,solar} A_i \hat{F}_{ij,solar}\sigma T_i^4\right)\right]$$
$$- \left[\left(1 - f_{0-\lambda_{step},T_j}\right)\left(\alpha_{i,therm}\,\varepsilon_{j,therm} A_j \hat{F}_{ji,therm}\sigma T_j^4\right)\right.$$
$$\left. + f_{0-\lambda_{step},T_j}\left(\alpha_{i,solar}\varepsilon_{j,solar} A_j \hat{F}_{ji,solar}\sigma T_j^4\right)\right] \quad (4\text{-}36)$$

where $\varepsilon_{therm}$ and $\varepsilon_{solar}$ represent the emissivity values at thermal and solar band, respectively. It is noteworthy that there are two different $\hat{F}$ parameters in this equation, i.e. $\hat{F}_{ij,therm}$ and $\hat{F}_{ij,solar}$. This can be explained from equation (4-26), where it is clear that the $\hat{F}$ parameter is dependent on the optical properties of the surfaces; therefore, there should be two sets of $\hat{F}$ parameter, one for solar and one for thermal emissivity. Equation (4-36) can be simplified as:

$$Q_{net,therm,ij} = \varepsilon_{j,therm}\,\varepsilon_{i,therm} A_i \hat{F}_{ij,therm}\sigma\left[\left(1 - f_{0-\lambda_{step},T_i}\right)T_i^4 - \left(1 - f_{0-\lambda_{step},T_j}\right)T_j^4\right]$$
$$+ \varepsilon_{j,solar}\varepsilon_{i,solar} A_i \hat{F}_{ij,solar}\sigma\left[f_{0-\lambda_{step},T_i}T_i^4 - f_{0-\lambda_{step},T_j}T_j^4\right] \quad (4\text{-}37)$$

The solar radiation heat transfer between surfaces $i$ and $j$ can be expressed as:

$$Q_{net,solar,ij} = \left[\left(1 - f_{0-\lambda_{step},T_{sun}}\right)Flux_{solar,i}\,(1 - \varepsilon_{i,therm})\,\hat{F}_{ij,therm} A_i \varepsilon_{j,therm}\right.$$
$$\left. - \left(1 - f_{0-\lambda_{step},T_{sun}}\right)Flux_{solar,j}\,(1 - \varepsilon_{j,therm})\,\hat{F}_{ij,therm} A_i \varepsilon_{i,therm}\right]$$
$$+ \left[f_{0-\lambda_{step},T_{sun}}Flux_{solar,i}\,(1 - \varepsilon_{i,solar})\,\hat{F}_{ij,solar} A_i \varepsilon_{j,solar}\right.$$
$$\left. - f_{0-\lambda_{step},T_{sun}}Flux_{solar,j}\,(1 - \varepsilon_{j,solar})\,\hat{F}_{ij,solar} A_i \varepsilon_{i,solar}\right] \quad (4\text{-}38)$$

which can be simplified as:

$$Q_{net,solar,ij} = \left(1 - f_{0-\lambda_{step},T_{sun}}\right) \hat{F}_{ij,therm} A_i \left[ Flux_{solar,i}(1 - \varepsilon_{i,therm}) \varepsilon_{j,therm} - Flux_{solar,j}(1 - \varepsilon_{j,therm}) \varepsilon_{i,therm} \right] + f_{0-\lambda_{step},T_{sun}} \hat{F}_{ij,solar} A_i \left[ Flux_{solar,i}(1 - \varepsilon_{i,solar}) \varepsilon_{j,solar} - Flux_{solar,j} (1 - \varepsilon_{j,solar}) \varepsilon_{i,solar} \right] \quad (4\text{-}39)$$

The overall radiative heat transfer between surfaces $i$ and $j$ is:

$$Q_{net,ij} = Q_{net,therm,ij} + Q_{net,solar,ij} \quad (4\text{-}40)$$

Net radiation leaving surface $i$ can be obtained by summing the equation (4-40) with respect to $j$:

$$Q_{net,i} = \sum_{j=1}^{N} Q_{net,ij} \quad (4\text{-}41)$$

### 4.4 Summary and Concluding Remarks

In this chapter, a thermal model of cavity type solar receiver was developed. The required correlations for natural and forced convective heat losses were introduced. Moreover, a detailed model for the radiative heat transfer was presented, which is based on the work done by [72]. The analytical and numerical methods for calculating the view factors were explained and validated against the data in the literature. The radiative heat transfer model takes into account the radiative heat transfer between gray surfaces inside an enclosure. In addition, heat transfer equations were derived for the condition that two different emissivity values exist for solar and thermal bands. Using the equations presented in this chapter, one can simulate the thermal performance of the receiver and finds the thermal efficiency, which will be discussed in more detail in the subsequent chapters.

# CHAPTER 5 THERMODYNAMIC ANALYSIS OF S-$CO_2$ POWER CYCLES[3]

## 5.1 Introduction

Carbon dioxide is a non-toxic, abundant, inexpensive, non-flammable and highly stable compound with low critical properties. It has been investigated as a working fluid for thermodynamic power cycles for many years.

Feher [74] designed the first supercritical $CO_2$ cycle in the United States in 1967. While the proposed cycle operates entirely above the critical pressure of $CO_2$, a pump is used for compression of the working fluid in the liquid phase. At the same time, Angelino [75] was working in Italy on designing a liquid phase compression gas turbine. He concluded that the efficiency of the resulting cycle is considerably higher than that of regenerative Brayton cycles and comparable with that of regenerative Rankine cycles. In 1968, he analyzed the thermodynamic performance of several carbon dioxide condensation cycles in which low temperature of the cycle is below the critical temperature, and concluded that a recompression $CO_2$ cycle in which compression is performed while the working fluid is partially in the liquid state achieves high efficiencies [76]. However, since the critical temperature of $CO_2$ is low (30.98°C), it requires low temperature cooling water that is not available at a large number of locations, especially at those with high solar resources. The low temperature cooling water limitation led to studies on the $CO_2$ cycle in the gas state only. In 1969, Angelino [77] considered real gas effects and found higher cycle efficiency mainly due to the

[3] This chapter has been previously published (Besarati, Saeb M., and D. Yogi Goswami. "Analysis of Advanced Supercritical Carbon Dioxide Power Cycles with a Bottoming Cycle for Concentrating Solar Power Applications." *Journal of Solar Energy Engineering* 136.1 (2014): 010904.)

reduction of specific volume and compression work around the critical point. Since then, s-$CO_2$ power cycles have drawn attention for nuclear power generation in gas reactors.

Dostal et al. [78] showed that the s-$CO_2$ cycle has a higher efficiency than the superheated steam cycle at temperatures above 470 ℃, which makes it suitable for nuclear power applications. Sarkar [79] [80] performed a detailed thermodynamic analysis and optimization of the cycle for a high temperature range of 480 ℃ to 750℃, considering a nuclear reactor as the heat source. Moisseytsev et al. [81] investigated alternative layouts for s-$CO_2$ Brayton cycle for a sodium-cooled fast reactor (SFR) including double recompression, intercooling and reheating. Jeong et al. [82] studied the potential improvement of the s-$CO_2$ cycle by mixing $CO_2$ with other gases in a SFR to alter its critical properties. The $CO_2$-He binary mixture showed the highest potential for efficiency improvement.

Although the majority of the studies have considered s-$CO_2$ for nuclear power applications, there is a growing interest in deploying it in CSP plants. The performances of different s-$CO_2$ Brayton cycle configurations for central receiver solar power plants were theoretically evaluated by Turchi et al. [20]. The results show that s-$CO_2$ Brayton cycle can achieve more that 50% efficiency under dry cooling conditions, which is consistent with the framework of the U.S. Department of Energy (DOE) "SunShot Concentrating Solar Power R&D" program [83]. The major advantages of the s-$CO_2$ Brayton cycle can be summarized as high efficiency, high power density, compactness and low cost [20].

This chapter presents the thermodynamic analysis of s-$CO_2$ cycles at temperature conditions appropriate for CSP plants. First, unusual thermodynamic features of $CO_2$ around its critical point are studied. Next, different cycle configurations are simulated and compared with the published data. Then, the effects of including a bottoming cycle on the cycle thermal efficiency are presented.

### 5.2 Characteristics of S-$CO_2$ Around the Critical Point

The critical point of $CO_2$ is 7.38 MPa and 30.98℃ (314.13 K). Around the critical point, $CO_2$ is not an ideal gas, and its behavior is very sensitive to the pressure and temperature. In other words, the fluid properties vary significantly around the critical point. Figure 5-1 shows the density variations of $CO_2$ at different operating conditions. As can be seen, the density is very high close to the critical point and comparable to liquids. Therefore, the compression work is considerably reduced if carbon dioxide enters the compressor close to the critical condition, which is the main advantage of s-$CO_2$ over the air Brayton cycle.

Wright et al. [17] compared the density of s-$CO_2$ in a closed loop Brayton cycle with that of water, as shown in Figure 5-2. At the specified condition, the density of the $CO_2$ at the inlet of the compressor is 60% of the density of water, which results in low compression power requirement.

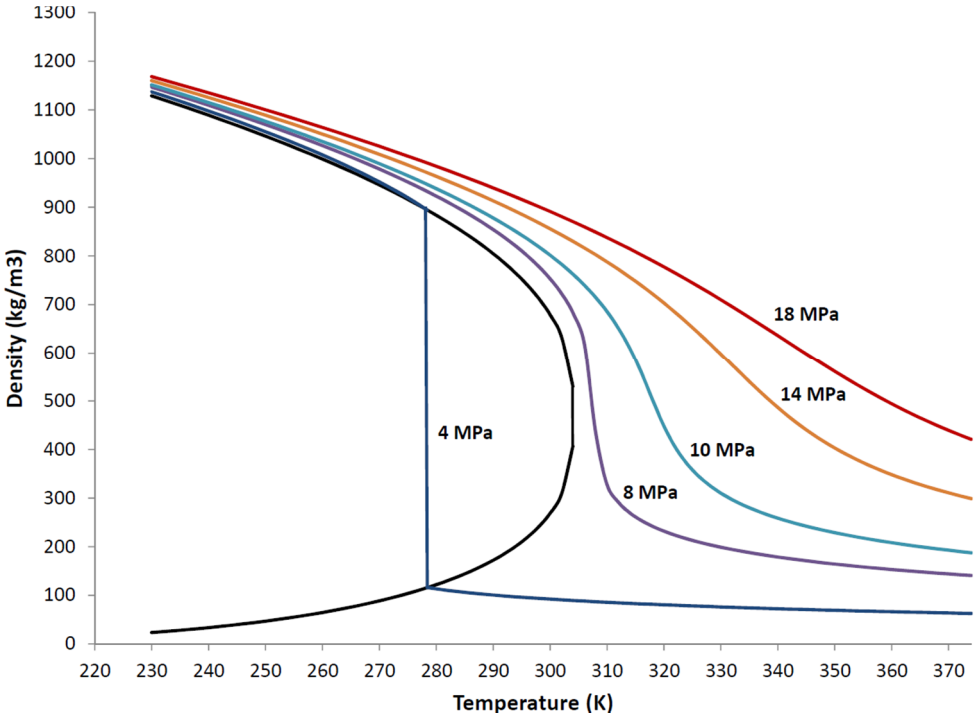


Figure 5-1 Variations of $CO_2$ density at different temperatures and pressures

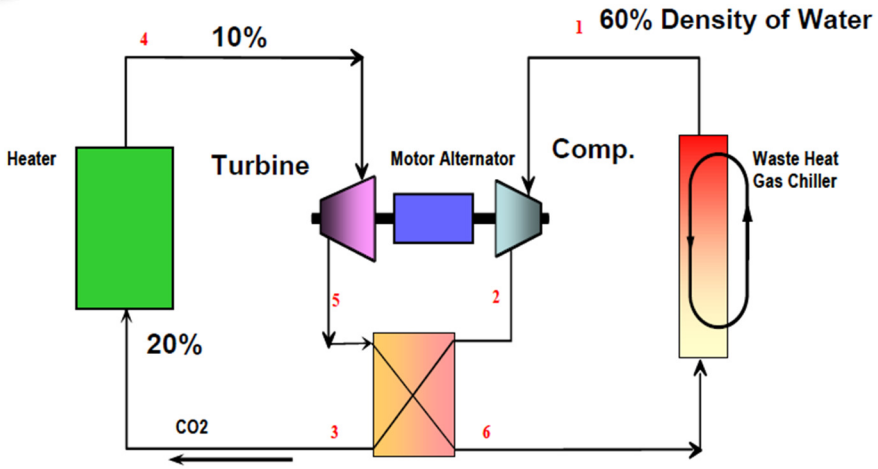


Figure 5-2 Comparison of the density of s-$CO_2$ with water

In addition to the density, other properties of $CO_2$ also change drastically around the critical point. As can be seen from Figure 5-3, the thermal conductivity of $CO_2$ maximizes close to the critical point reaching 148.95 $\frac{\text{m W}}{\text{m}-\text{K}}$ at 305 K. According to Refprop [84], the thermal conductivity of water at 305K is 618.41 $\frac{\text{m W}}{\text{m}-\text{K}}$. At the atmospheric pressure and the same temperature, the thermal conductivity of air is given as 26.355 $\frac{\text{m W}}{\text{m}-\text{K}}$.

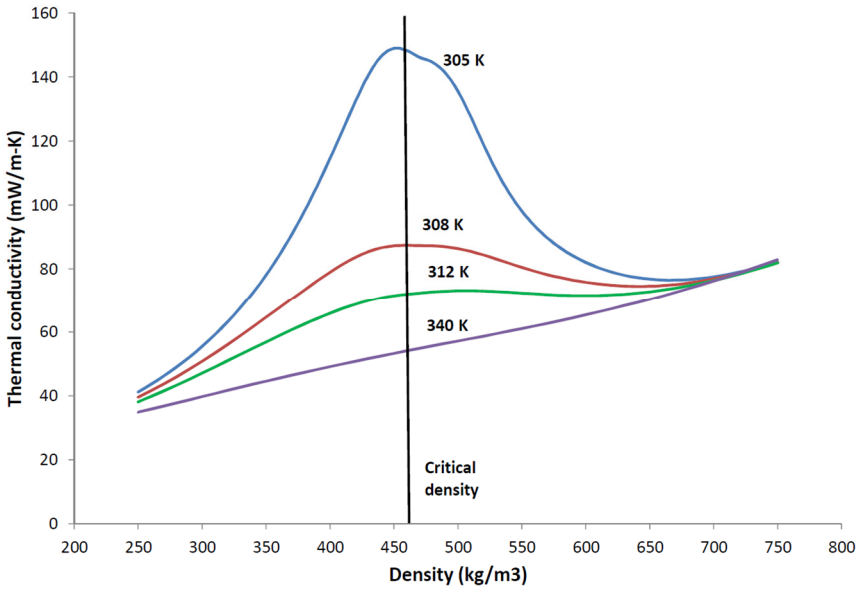


Figure 5-3 Variations of $CO_2$ thermal conductivity at different operating conditions

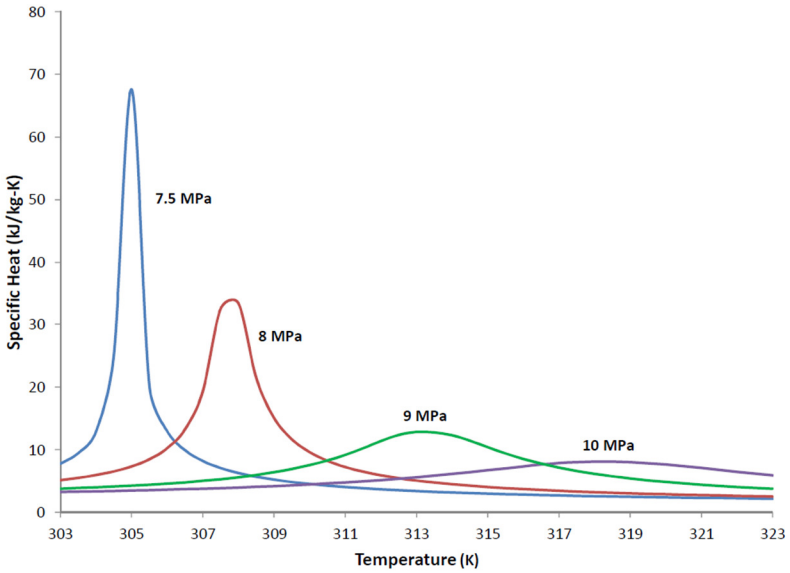


Figure 5-4 Variations of the specific heat close to the critical temperature

Figure 5-4 shows how the specific heat of $CO_2$ changes close to the critical point. The large variations in specific heat affect the recuperator design in the power cycle. It is known that for a certain operating condition, a pinch-point exists in the recuperator. The pinch-point is the location where the temperature difference between the hot and cold streams is the lowest. As the specific heat varies radically with the changes in the pressure and the temperature, the temperature difference between the fluids varies widely within the recuperator. Consequently, the pinch-point location may be found somewhere along the recuperator, not at the inlet or the outlet. Therefore, more detailed analysis of the temperature profiles is necessary to evaluate the performance of the recuperator. Moreover, the recuperator size and efficiency are directly affected by the operating pressure. Therefore, unlike many other recuperators working with ideal gases such as helium where the temperature difference is almost constant and only dependent on the pressure ratio and the temperatures, the operating pressure is also important and has to be optimally determined. In addition, the high specific heat of the $CO_2$ close to the critical point requires high mass flow rate cooling water in the precooler which increases the parasitic losses [85].

## 5.3 S-$CO_2$ Brayton Cycle Configurations

Three configurations are considered in this study, which are named as simple, recompression, and partial cooling Brayton cycles.

### 5.3.1 Simple Cycle

The simple cycle is the one from which the other two configurations are derived, which is shown in Figure 5-5.

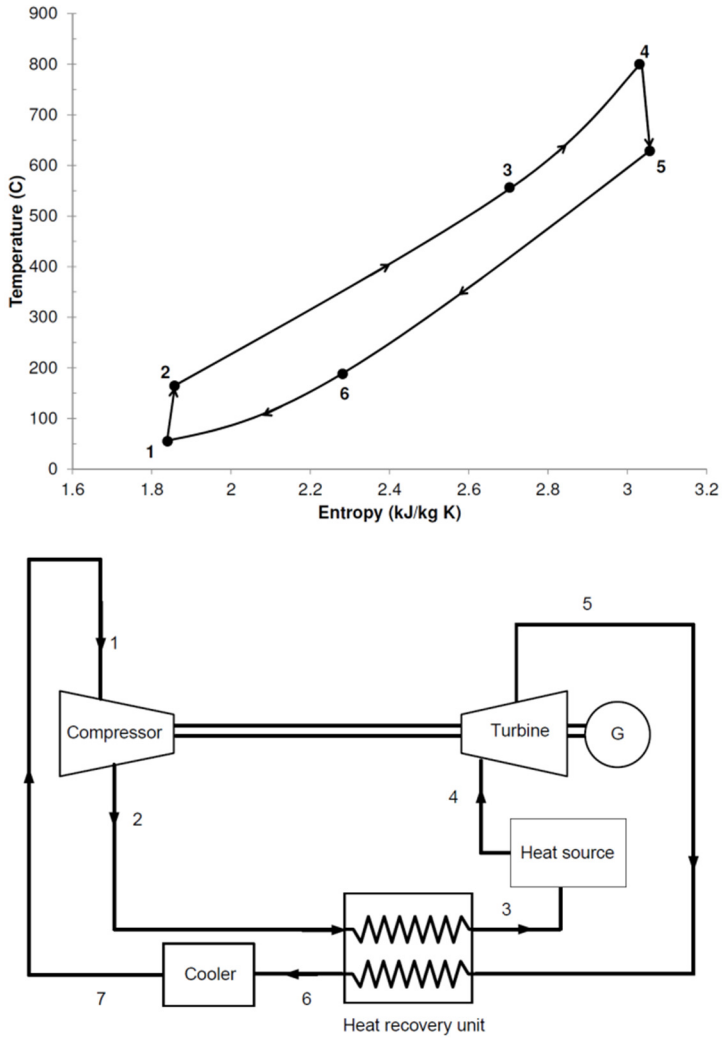


Figure 5-5 Simple s-$CO_2$ Brayton cycle

High temperature s-$CO_2$ enters the turbine where it is expanded to the low pressure of the cycle. Next, it goes through the recuperator and transfers energy to the flow leaving the compressor.

Then, it is cooled by rejecting heat to the cold sink and pressurized by the compressor, respectively. The pressurized s-$CO_2$ gains energy in the recuperator and exits to the heater. The cycle efficiency can be increased by dividing the compression into two-stages and using an intercooler in between. Similarly, using a two stage expansion and a reheater can be beneficial.

### 5.3.2 Recompression Cycle

In recompression Brayton cycle, the flow is divided into two streams after leaving the low temperature recuperator (LTR). A fraction of the flow rejects heat to the cold sink and exits to the main compressor (mc) while the other fraction is pressurized in a recompression compressor (rc) without cooling down (Figure 5-6). The two streams are mixed at point 3, and the mixed stream enters a high temperature recuperator (HTR) and a heater, where thermal energy is added to achieve the required turbine inlet temperature. After expanding in the turbine, the flow is directed into HTR and LTR to preheat the high pressure stream. The main advantage of the recompression cycle over the simple configuration is better heat recovery. Splitting the flow after the LTR decreases the heat capacity of the high pressure side in LTR, which helps to avoid common pinch point problems. The fraction of the flow that enters the cooler and the main compressor is an important parameter which directly affects the cycle performance.

### 5.3.3 Partial Cooling Cycle

This configuration is similar to the recompression cycle; however, one more compressor and cooler are included. The low pressure flow leaving the LTR cools down in a cooler before entering the precompressor (pc) where the pressure increases to an intermediate value (Figure 5-7). Then, the flow is divided into two streams: one entering the main compressor after rejecting heat and the other going through the recompression compressor. The two streams are mixed before entering the HTR and receiving heat.

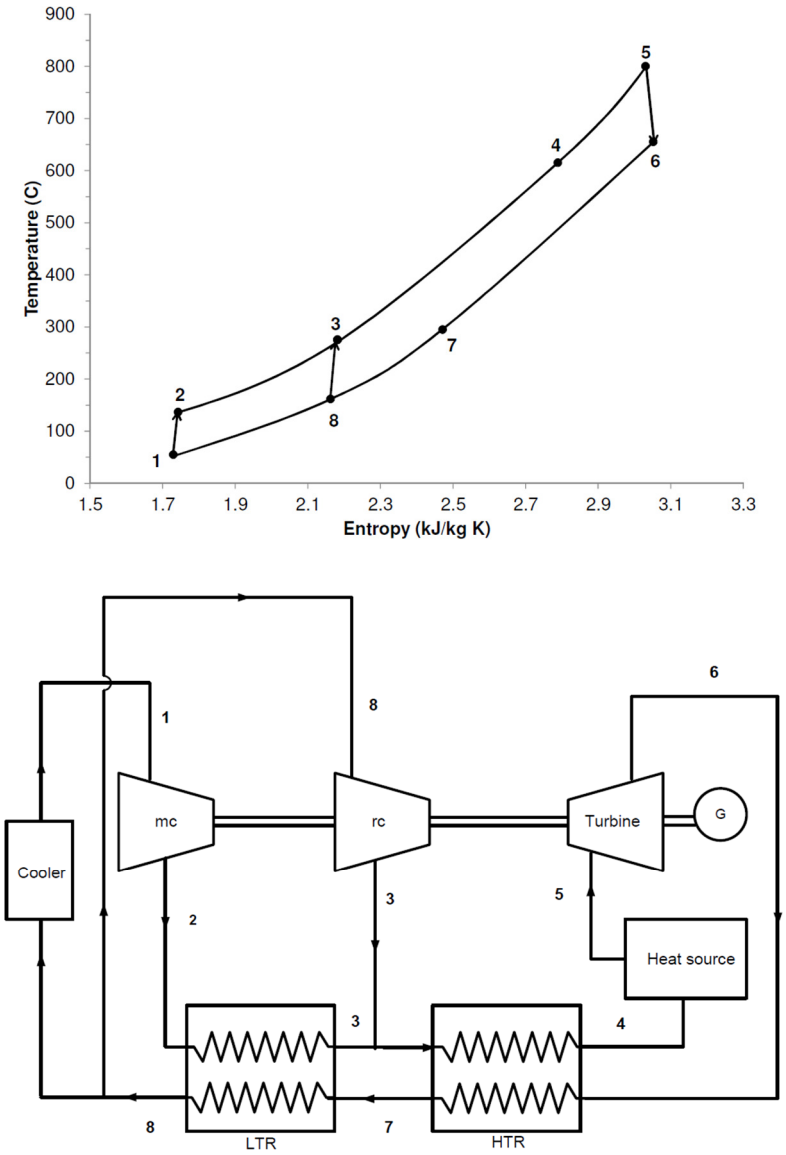


Figure 5-6 Recompression s-$CO_2$ Brayton cycle

In this type of cycle, the compression is done in two stages and temperature of the working fluid at the inlet of the compressors is lower than the recompression configuration. Dostal et al. [86] analyzed this cycle and concluded that its efficiency is higher than the recompression configuration at high turbine inlet temperatures. It is also more robust to the variation of the cycle pressure ratio. The pressure ratio of this cycle is usually more than the recompression cycle, which makes it suitable for reheating [20].

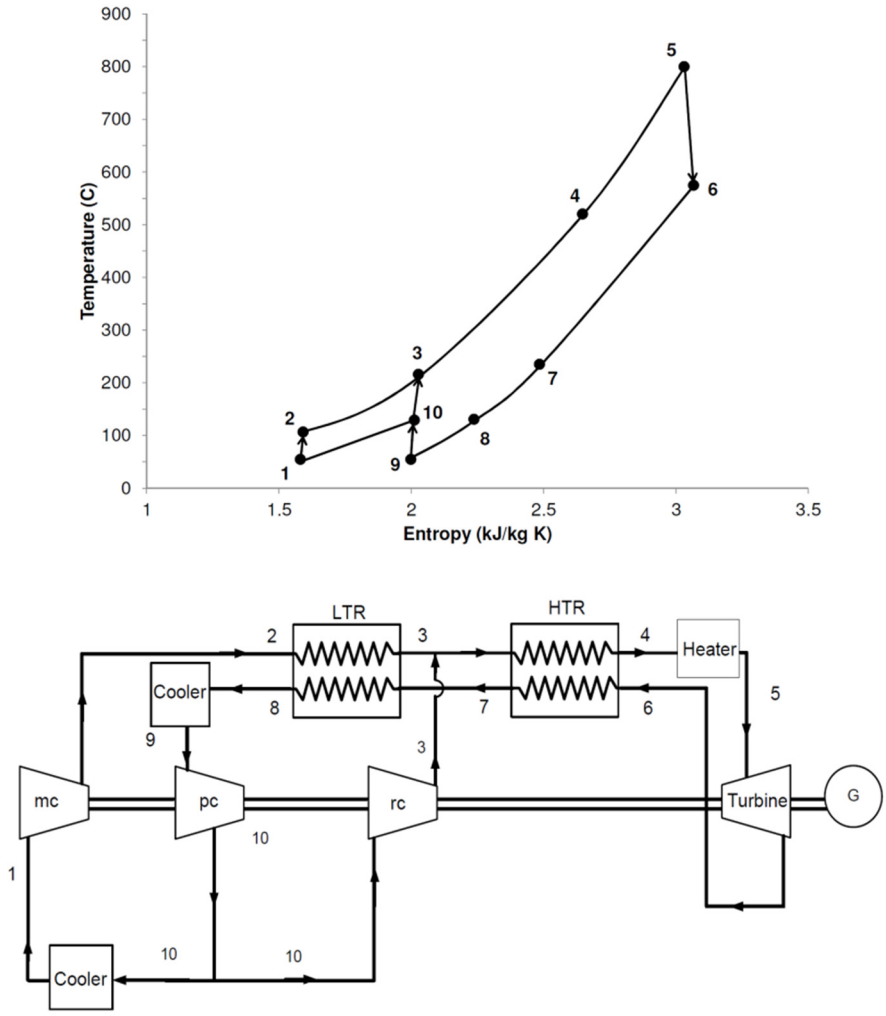


Figure 5-7 Partial cooling s-$CO_2$ Brayton cycle

## 5.4 Modeling Approach

In order to be consistent with the results presented by Turchi et al. [20], same modeling approach is considered. The following assumptions are made for this study:

(1) Pressure losses in the pipes and heat exchangers are negligible.

(2) Heat loss to the ambient is negligible.

(3) Expansion and compression processes are adiabatic.

(4) Working fluid always achieves the specified temperature at the outlet of the cooler and the heater.

(5) All processes attain steady state.

The recuperators are modeled by defining an effectiveness factor. In the recompression and partial cooling cycles, an effectiveness factor is also considered for the total hot stream [20] which is given as:

$$\varepsilon_{hot\ stream} = \frac{h_6 - h_8}{h_6 - h_8(T_2, P_8)} \tag{5-1}$$

In the denominator, the enthalpy at state 8 is calculated based on the assumption that the temperature of the hot fluid leaving LTR reaches the temperature of state 2. Having the enthalpy of the fluid at state 8 using the above formula, the effectiveness of the LTR can be found accordingly. The temperature profiles of the hot and cold streams are obtained by discretizing the heat exchangers along the flow to make sure the minimum temperature difference between the two streams (pinch point) is more than a predetermined value. The output conditions of the compressors and turbines are simply determined by considering a constant isentropic efficiency. The mass fraction of the fluid that goes to LTR in recompression and partial cooling configurations can be found using iteration technique until the temperatures at the outlet of the LTR and recompression compressor (state 3) become almost equal. Refprop [84] is used to find the properties of $CO_2$ at different pressures and temperatures.

In order to validate the model, the results can be compared with the available data in the literature. For a minimum cycle temperature of 32℃, turbine inlet temperature of 550℃, maximum pressure of 25 MPa, heat exchanger effectiveness of 95%, isentropic compressor efficiency of 89%, and isentropic turbine efficiency of 93%, the maximum cycle efficiency for the simple s-$CO_2$ Brayton cycle is found as 40.44%. The pressure ratio is obtained as 3.4 by parametric optimization and setting 5℃ as the minimum temperature difference between the hot and cold streams in the recuperator. The efficiencies given by Dostal [86] and Turchi et al. [20] at the same operating

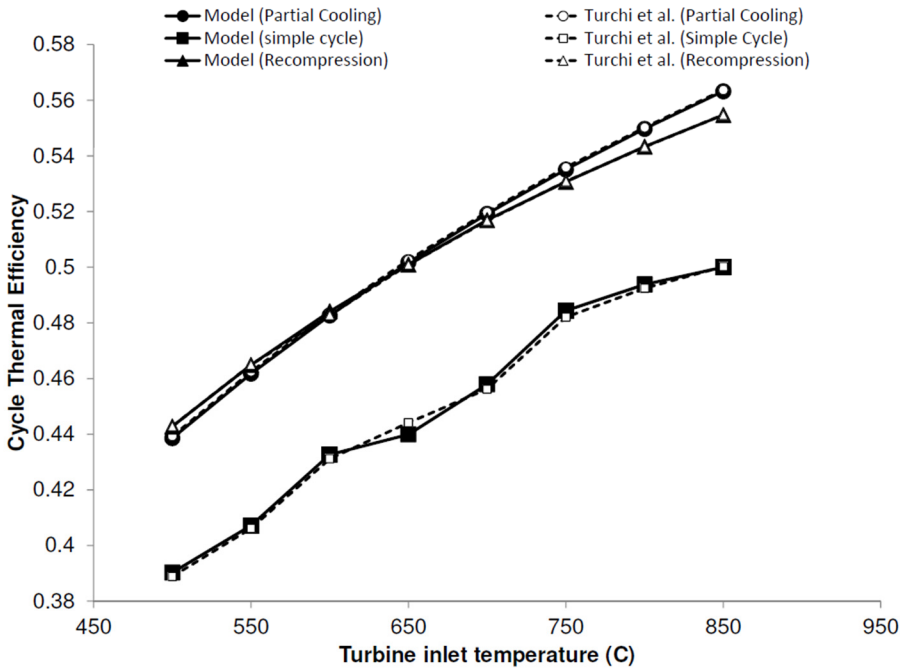


Figure 5-8 Validating the model by comparing with the data from Turchi et al. [20]

conditions are 40.40% and 40.43%, respectively. The maximum cycle efficiencies at different turbine inlet temperatures for the three configurations are shown and compared with those given by Turchi et al. [20] in Figure 5-8. The cycle pressure ratio for the simple and the recompression cycles are found by parametric optimization. The partial cooling configuration has two design variables, which need to be optimally defined, i.e. the cycle pressure ratio ($\frac{P_5}{P_6}$) and the intermediate pressure ratio ($\frac{P_5}{P_{10}}$). A MATLAB code is developed based on genetic algorithms to handle all the required optimization tasks in this study [87].

As can be seen from Figure 5-8, the model can accurately predict the efficiency values given by Turchi et al. [20]. It is noteworthy that the turbine efficiency of the recompression cycle was 90% while in other cycles 93% turbine efficiency was used. These are the values used by Turchi et al. [20] for modeling the cycles. The larger difference between the partial cooling and recompression cycles at high turbine inlet temperatures is due to this assumption.

Although the efficiency of the s-$CO_2$ Brayton cycle is high, it might be further improved by considering an appropriate bottoming cycle utilizing waste heat from the top s-$CO_2$ cycle. ORC is one of the alternatives which is extensively used when the heat source temperature is below 370 ℃ [88]. However, the cycle performance is substantially affected by the selection of the working fluid. Chacartegui et al. [89] studied the performance of combined s-$CO_2$-ORC cycle with different working fluids under different operating conditions. The results showed that the efficiency of the s-$CO_2$ was improved by 7-12 percentage points, depending on the turbine inlet temperature. It is noteworthy that the simple s-$CO_2$ configuration was considered for that study. In another study, Sanchez et al. [90] investigated the performance of a combined s-$CO_2$-ORC cycle using mixtures of hydrocarbons in the bottoming cycle. The results showed that the performance of the cycle is directly affected by the mixture's composition. It was concluded that doping the optimum pure fluid with a heavier fluid enhances the performance at higher temperatures, whereas doping with lighter fluid is more appropriate at lower temperatures. In that study also the simple s-$CO_2$ configuration was considered as the top cycle.

In this dissertation, three different configurations of s-$CO_2$ Brayton cycle, i.e. simple, recompression, and partial cooling, are considered as the top cycles providing heat for an organic Rankine bottoming cycle. Different working fluids are examined for the ORC for each configuration, and the operating conditions are optimized. The combined cycle energy efficiencies and turbine expansion ratios are compared to find the appropriate working fluids for each configuration.

### 5.5 Combined S-$CO_2$ - ORC Cycle

In this section an ORC is included with each configuration as a bottoming cycle to utilize the waste heat from the s-$CO_2$ cycle and generate power. The ORC uses organic working fluids with low boiling points to recover heat from low temperature heat sources. The performance of the ORC is

substantially affected by the selection of the working fluid. The organic working fluids are generally divided into three categories depending on the slope of the saturation curve in the T-s diagram, i.e. wet (e.g. water with negative slope), isentropic (e.g. R11 with vertical slope), and dry (e.g. isopentane with positive slope). The wet fluids usually need to be superheated in order to avoid liquid droplets impingent in the turbine blades during the expansion [91]. In this study only dry fluids are considered for the ORC cycle and in all cases the working fluid enters the turbine in saturated vapor state. Environmental impact of using the organic fluids also needs to be taken into consideration. The main concerns are the ozone depletion potential (ODP), global warming potential (GWP), and the atmospheric lifetime (ALT). Considering these parameters some working fluids have already been phased out such as R-11 and R-115, and others such as R141b and R142b are planned to be phased out soon. These working fluids are not considered in this study. Although many of the working fluids considered are flammable, this is not a problem as long as proper precautions are taken. Moreover, auto ignition is not a concern in this study, as the maximum operating temperatures of the working fluids are relatively low.

Table 5-1 provides a list of the working fluids considered in this study along with their critical properties and a parameter, $T_{tmax}$, which is the maximum operating temperature limit for each. The reason this value is determined is that at temperatures close to the critical point the fluid is unstable; therefore, there should be a reasonable distance between the high temperature limit of the cycle and the critical temperature. However, there is not a single interpretation of the reasonable distance in the literature. In this study, the method proposed by Rayegan and Tao [92] is used. In this method, the highest temperature of the cycle is first limited to a point on saturation curve where the s slope of the T-s diagram is infinity (point A in Figure 5-9). Then, this temperature is increased up to

Table 5-1 Properties of the working fluids used in this study

| Working Fluid | $T_{cr}$(℃) | $P_{cr}(MPa)$ | $T_{t\max}$(℃) |
|---|---|---|---|
| R-123 | 183.68 | 3.66 | 166.05 |
| R-124 | 122.28 | 3.62 | 102.78 |
| R-227ea | 102.8 | 3 | 91.09 |
| R-236ea | 139.29 | 3.5 | 132.69 |
| R-245ca | 174.42 | 3.93 | 158.13 |
| R-245fa | 154.05 | 3.64 | 139.38 |
| R-C318 | 115.23 | 2.78 | 106.54 |
| R-365mfc | 186.85 | 3.266 | 177.21 |
| Benzene | 288.87 | 4.906 | 273.35 |
| Butane | 151.98 | 3.8 | 137.36 |
| Butene | 146.14 | 4.005 | 126.01 |
| C4F10 | 113.18 | 2.32 | 107.14 |
| C5F12 | 147.41 | 2.05 | 144.21 |
| Cis-butene | 162.6 | 4.225 | 140.46 |
| Cyclohexane | 280.45 | 4.075 | 274.50 |
| Decane | 344.55 | 2.103 | 340.10 |
| Heptane | 266.98 | 2.736 | 261.56 |
| Isobutane | 134.66 | 3.63 | 120.32 |
| Isobutene | 144.94 | 4.009 | 126.05 |
| Isohexane | 224.55 | 3.04 | 216.88 |
| Isopentane | 187.25 | 3.37 | 177.87 |
| neopentane | 160.59 | 3.196 | 152.27 |
| Nonane | 321.4 | 2.281 | 316.43 |
| Octane | 296.17 | 2.497 | 290.50 |
| Pentane | 196.55 | 3.37 | 186.82 |
| Toluene | 318.6 | 4.13 | 307.46 |

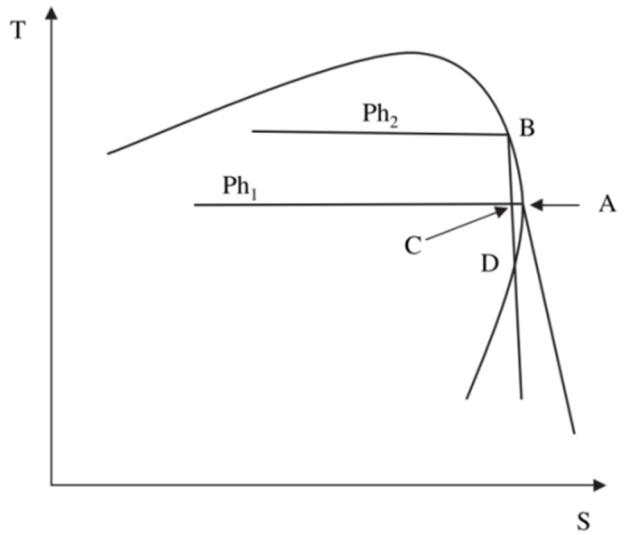


Figure 5-9 High temperature limit of the ORC cycle [92]

Table 5-2 Input parameters to the combined s-$CO_2$-ORC cycle model

| | |
|---|---|
| Maximum pressure | 25 MPa |
| Maximum temperature of $CO_2$ cycle | 800 ℃ |
| Minimum temperature of ORC and $CO_2$ cycles | 55 ℃ |
| Mass flow rate of the s-$CO_2$ Cycle | 1 kg/s |
| Heat exchanger effectiveness | 0.95 |
| Total hot stream effectiveness | 0.95 |
| Pinch Point | 5 ℃ |
| $CO_2$ turbine efficiency | 0.90 |
| Compressor efficiency | 0.89 |
| ORC turbine efficiency | 0.87 |
| ORC pump efficiency | 0.85 |

a point "B" where further increasing the temperature causes the quality of the working fluid to drop to less than 99% during the expansion process.

In Figure 5-9, the maximum mass fraction of the liquid is at point C, which is assumed to be less than one percent. It is noteworthy that assuming 99% dryness is more than necessary and the cycle can still operate with lower values without any problem. However, decreasing this value to 90% does not affect the efficiency very much; therefore, the 99% dryness constraint is applied to calculate $T_{tmax}$ in Table 5-1. Refprop [84] is used to find the properties of the organic fluids.

The input parameters to the model of the combined cycle are given in Table 5-2. It is assumed that the combined cycle operates in a SPT plant. The maximum temperature of the s-$CO_2$ cycle in this study is fixed at 800℃, which is achievable in SPT plants, though higher temperatures can be reached depending on the design of the receiver. The main challenge in the receiver design for the s-$CO_2$ cycle is the high operating pressure. The maximum pressure of the $CO_2$ cycle is set at 25MPa, considering piping availability and flange seal needs. CSP plants are usually located in the areas where water resources are limited; therefore, dry cooling may be preferred over wet cooling. A dry bulb temperature of 41 ℃ represents the $99.8^{th}$ percentile of the annual temperature distribution

in Daggett, CA, therefore, the minimum temperature of both $CO_2$ and ORC cycles are set to 55 ℃ [20]. In the modeling of the recuperators in recompression and partial cooling cycles, the effectiveness of the HTR and the total hot stream are set at 0.95, and the effectiveness of the LTR is found accordingly. The temperature profiles of the hot and cold streams in all the heat exchangers are checked to make sure the pinch point constraint is not violated.

It is important to mention that the range of the pressure ratio considered for the combined cycles during optimization is larger than the stand-alone cycles. In other words, the s-$CO_2$ turbine is allowed to expand to subcritical pressure with supercritical temperature for all the configurations, yielding trans-critical carbon dioxide cycles [89]. The maximum pressure ratio for the simple and recompression configurations is limited to 5 while it is extended to 7 for the partial cooling cycle.

### 5.5.1 Combined Simple S-$CO_2$-ORC Cycle

The combined cycle configuration is shown in Figure 5-10. The s-$CO_2$ goes through the heat recovery unit and provides heat for the ORC cycle before entering the cooler. The maximum mass flow rate of the ORC is found by setting the minimum temperature difference between the hot and cold streams in the heat recovery unit at 5℃. The s-$CO_2$ cycle pressure ratio ($r_p$) and the turbine inlet temperature of the ORC cycle ($T_{3R}$) are the parameters that need to be optimally determined by maximizing the combined cycle efficiency. This is done for every working fluid listed in Table 5-1. Different parameters can be used as the decision criteria for the selection of the working fluids, from which combined cycle efficiency ($\eta_{combined}$) and expansion ratio of the ORC turbine ($\phi$) are considered in this study which are defined as:

$$\eta_{combined} = \frac{W_{net,CO_2} + W_{net,ORC}}{Q_{in}} \tag{5-2}$$

$$\phi = \frac{\dot{V}_{4R}}{\dot{V}_{3R}} \tag{5-3}$$

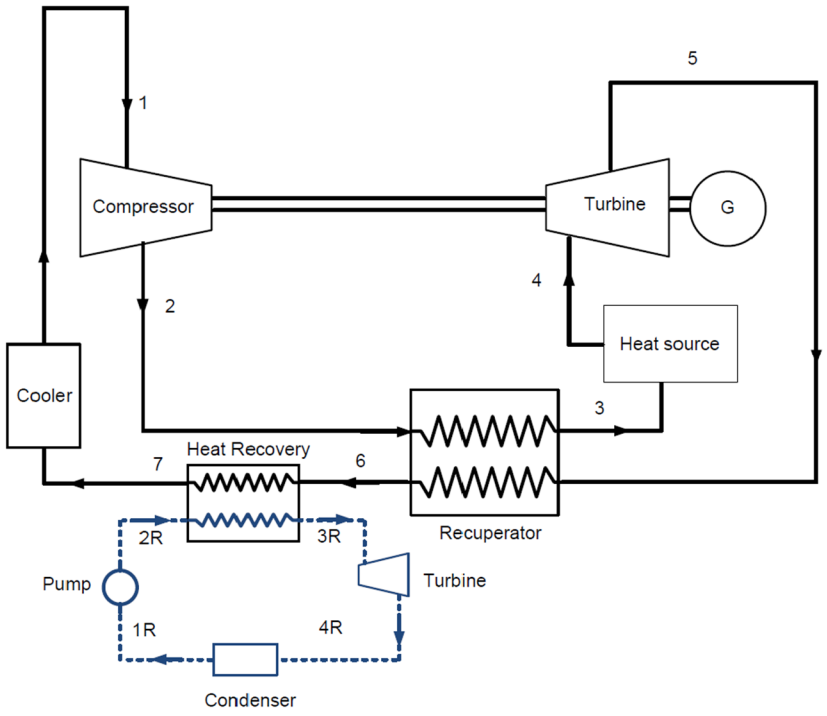


Figure 5-10 Combined simple s-$CO_2$ –ORC cycle. The ORC cycle is shown with dashed lines

where $\dot{V}$ represents the volumetric flow rate ($m^3/s$). For the design of the ORC turbine, the organic fluids with high expansion ratios are not recommended because of supersonic flow problems, larger turbine size or greater number of stages [92]. Figure 5-11 compares the performance of the combined cycle for different organic fluids.

As can be seen, the maximum efficiency is obtained by using Isopentane as the ORC fluid, i.e. 0.5216. On the other hand, the ORC turbine expansion ratio for this fluid is very high, i.e. 20.29, which makes it unsuitable for the design of the turbine. The same problem exists for some other working fluids where the high efficiency is accompanied by a high expansion ratio. The lowest expansion ratio, 3.53, is obtained by R227ea and has a thermal efficiency of 0.4835. Considering both thermal efficiency and expansion ratio as the decision criteria, R236ea, R245fa, Butane, Butene, Cis-butene, and Isobutene are shortlisted for further consideration. A comparative analysis

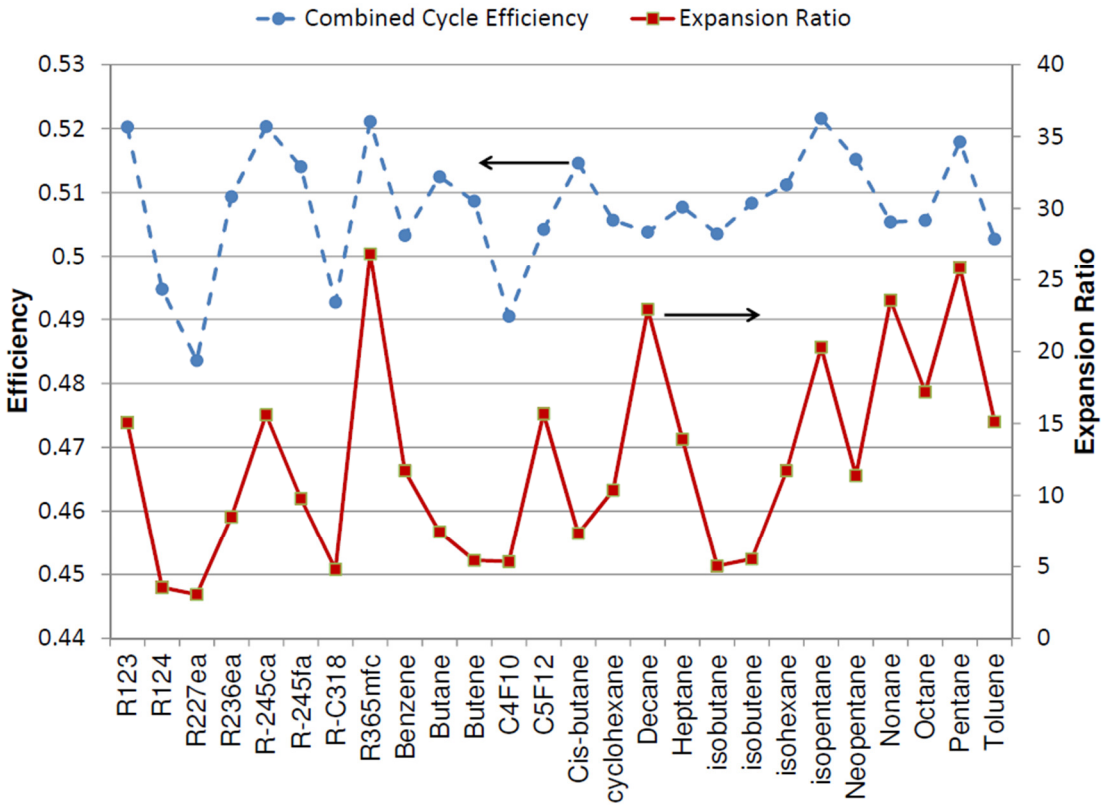


Figure 5-11 Performance evaluation of the combined simple s-$CO_2$-ORC cycle

of these candidates is used for final selection, e.g. while R245fa has a combined thermal efficiency of 0.5140 and expansion ratio of 9.78, it is less advantageous in comparison to Cis-butene with a thermal efficiency of 0.5146 and expansion ratio of 7.32. Finally, Butene and Cis-butene are selected as the only working fluids that cannot be out-performed by others.

Table 5-3 summarizes the optimal operating conditions for these working fluids. As might be expected, the turbine inlet temperature of the ORC cycle for both fluids is equal to their maximum operating temperature limit, $T_{tmax}$, that is given in Table 5-1. Maximum pressure of the ORC cycle

Table 5-3 Selected working fluids for simple s-$CO_2$-ORC cycle

| Working fluid | $r_p$ | $T_{3R}$ | $P_{max}$ | $m_{ORC}$ | $\eta_{combined}$ | $\phi$ |
|---|---|---|---|---|---|---|
| Butene | 4.22 | 126.01 | 2.85 | 0.448 | 0.5086 | 5.43 |
| Cis-butene | 4.52 | 140.46 | 2.96 | 0.395 | 0.5146 | 7.32 |

($P_{max}$) for each working fluid is also given in the table. Higher pressures require thicker pipes and more expensive heat exchangers. The efficiency of the simple s-$CO_2$ configuration without the bottoming cycle under same operating condition is obtained as 0.4507.

### 5.5.2 Combined Recompression S-$CO_2$-ORC Cycle

The combined cycle configuration for the recompression cycle is shown in Figure 5-12. As can be seen, a heat recovery unit is included before the cooler and the main compressor. Therefore, only a fraction of the total mass flow rate of s-$CO_2$ enters the heat recovery unit. Including the heat recovery before splitting the mass and right after the LTR reduces the temperature of the flow entering the recompression compressor. Consequently, the temperature at point 3 decreases which negatively affects the performance of the cycle.

Similar to the combined simple s-$CO_2$-ORC cycle, the recompression s-$CO_2$ cycle pressure ratio and the turbine inlet temperature of the ORC cycle are determined by maximizing the combined cycle efficiency. The performance of the combined cycle under optimal condition for each working

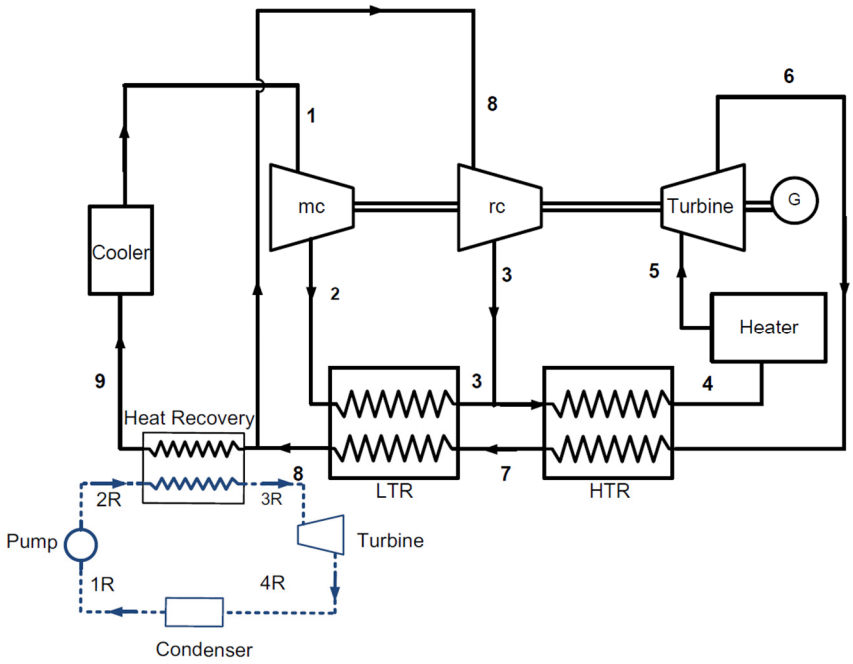


Figure 5-12 Combined recompression s-$CO_2$-ORC cycle

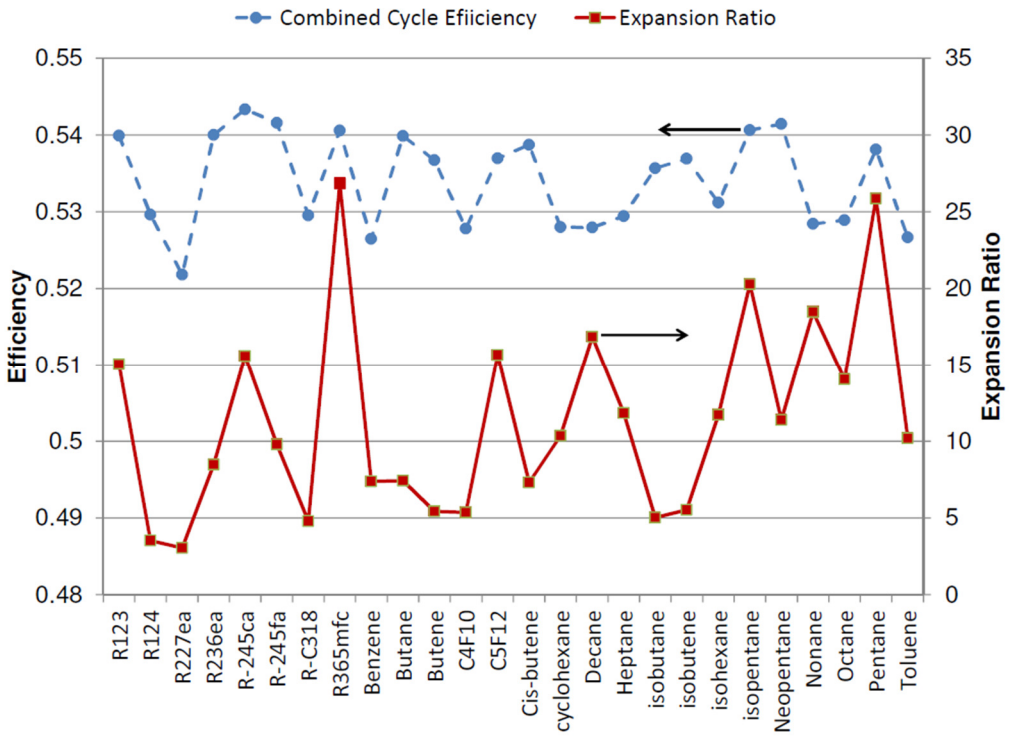


Figure 5-13 Performance evaluation of the combined recompression s-$CO_2$-ORC cycle

fluid is shown in Figure 5-13. The maximum efficiency is obtained by using R245ca, i.e. 0.5433, with an impractical expansion ratio of 29.58. The minimum expansion ratio is obtained by using R227ea, i.e. 3.05, where the maximized thermal efficiency is equal to 0.5218.

Following the same procedure as explained in the previous section, six working fluids are found as superior to the others, which are given in Table 5-4. The turbine inlet temperature of the ORC cycle for all the fluids is equal to their maximum operating temperature limit, $T_{t\max}$, which is

Table 5-4 Selected working fluids for recompression s-$CO_2$-ORC

| Working fluid | $r_p$ | $T_{3R}$ | $P_{max}$ | $m_{ORC}$ | $\eta_{combined}$ | $\phi$ |
|---|---|---|---|---|---|---|
| R236ea | 3.45 | 132.69 | 2.99 | 0.671 | 0.5400 | 8.48 |
| R245fa | 3.84 | 139.38 | 2.79 | 0.58 | 0.5416 | 9.78 |
| Butane | 3.84 | 137.36 | 2.98 | 0.299 | 0.5398 | 7.43 |
| Butene | 3.45 | 126.01 | 2.85 | 0.285 | 0.5367 | 5.42 |
| CisButene | 4.13 | 140.46 | 2.96 | 0.286 | 0.5387 | 7.32 |
| Isobutane | 3.26 | 120.32 | 2.85 | 0.280 | 0.5357 | 5.03 |

given in Table 5-1. The efficiency of the recompression s-$CO_2$ configuration without the bottoming cycle under same operating condition is obtained as 0.4932.

### 5.5.3 Combined Partial Cooling S-$CO_2$-ORC Cycle

The combined cycle layout is shown in Figure 5-14. After leaving the LTR, the low pressure s-$CO_2$ enters the heat recovery unit and provides heat for the bottoming cycle. There are three parameters that need to be optimally determined by maximizing the combined cycle efficiency, i.e. cycle pressure ratio ($r_p = \frac{P_5}{P_6}$), intermediate pressure ratio ($r_{pp} = \frac{P_5}{P_{10}}$), and the ORC turbine inlet temperature ($T_{3R}$).

The maximized thermal efficiency and the corresponding turbine expansion ratio of the combined cycle for each working fluid are shown in Figure 5-15. Similar to the recompression cycle, the maximum efficiency is obtained by using R245ca, i.e. 0.5256, with an expansion ratio of 15.61. The minimum expansion ratio, which is 3.05, is also obtained for R227ea with a maximized thermal

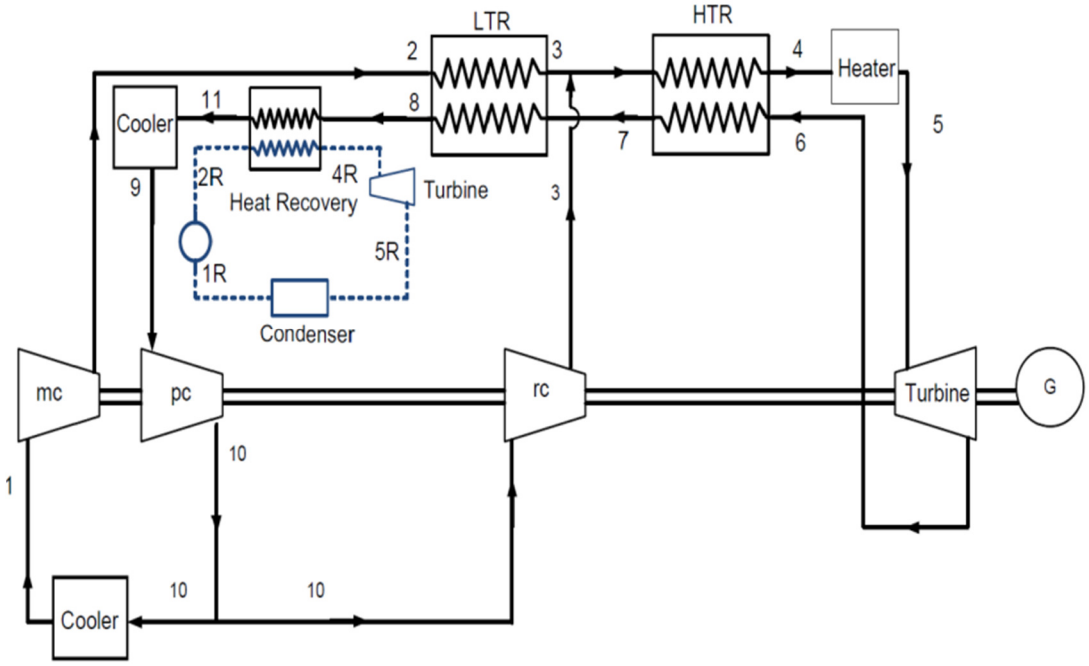


Figure 5-14 Combined partial cooling s-$CO_2$-ORC cycle

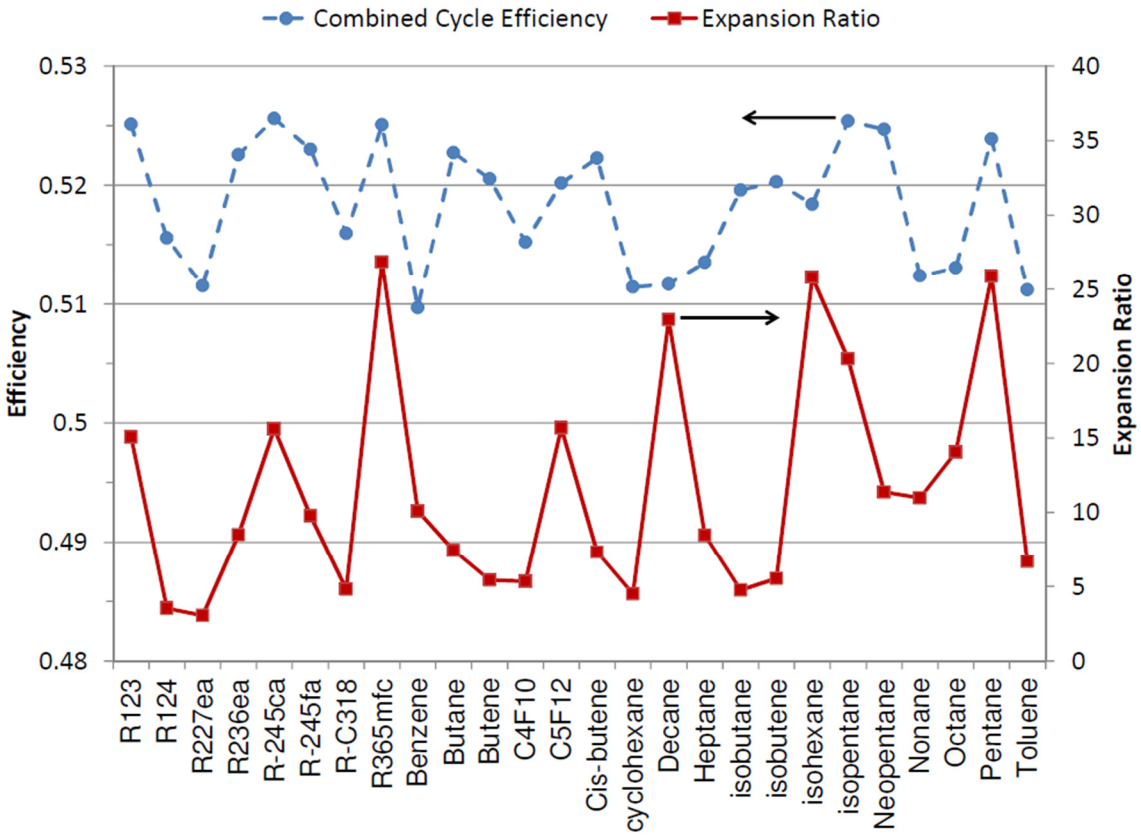


Figure 5-15 Performance evaluation of the combined partial cooling s-$CO_2$-ORC cycle

efficiency of 0.5115. The final recommended list of the working fluids for the combined partial cooling s-$CO_2$ –ORC cycle is given in Table 5-5. The maximum operating pressures for all the working fluids, except R124, are similar to those given in Table 5-4. The maximum pressure of R124 is 2.51 MPa. The efficiency of the partial cooling s-CO2 configuration without the bottoming cycle under same operating condition is obtained as 0.4959.

Table 5-5 Selected working fluids for partial cooling s-$CO_2$-ORC

| Working fluid | $r_p$ | $r_{pp}$ | $P_{max}$ | $m_{ORC}$ | $T_{3R}$ | $\eta_{combined}$ | $\phi$ |
|---|---|---|---|---|---|---|---|
| R124 | 5.39 | 2.95 | 2.51 | 0.81 | 102.78 | 0.5156 | 3.53 |
| R245fa | 6.52 | 4.08 | 2.79 | 0.71 | 139.38 | 0.5230 | 9.78 |
| Butane | 5.71 | 3.92 | 2.98 | 0.36 | 137.36 | 0.5228 | 7.43 |
| Butene | 5.87 | 3.59 | 2.86 | 0.35 | 126.01 | 0.5205 | 5.42 |
| Cis-butene | 6.19 | 4.24 | 2.96 | 0.35 | 140.46 | 0.5223 | 7.32 |
| Isobutane | 5.39 | 3.11 | 2.85 | 0.34 | 120.32 | 0.5196 | 4.76 |

### 5.6 Summary and Concluding Remarks

According to the results presented in the former sections, adding an appropriate bottoming cycle can increase the overall cycle efficiency by 3 to 7 percentage points under the specified conditions. The largest efficiency increase is achieved by using a simple s-$CO_2$ as the top cycle. However, this cycle is less efficient than the recompression and the partial cooling cycles. The maximum combined cycle efficiency is obtained by the recompression s-$CO_2$ -ORC cycle.

In order to make sure this conclusion is valid at other heat source temperatures also, the turbine inlet temperature is varied from 700℃ to 850℃. Performances of the s-$CO_2$ cycles (without bottoming cycles) and the combined cycles are optimized at each temperature. The organic working fluid used for each configuration is the one with maximum efficiency, which is given in the recommended lists (Table 5-3 to Table 5-5), i.e. Cis-butene for the simple cycle, R245fa for the recompression and the partial cooling cycles. The results are presented in Figure 5-16.

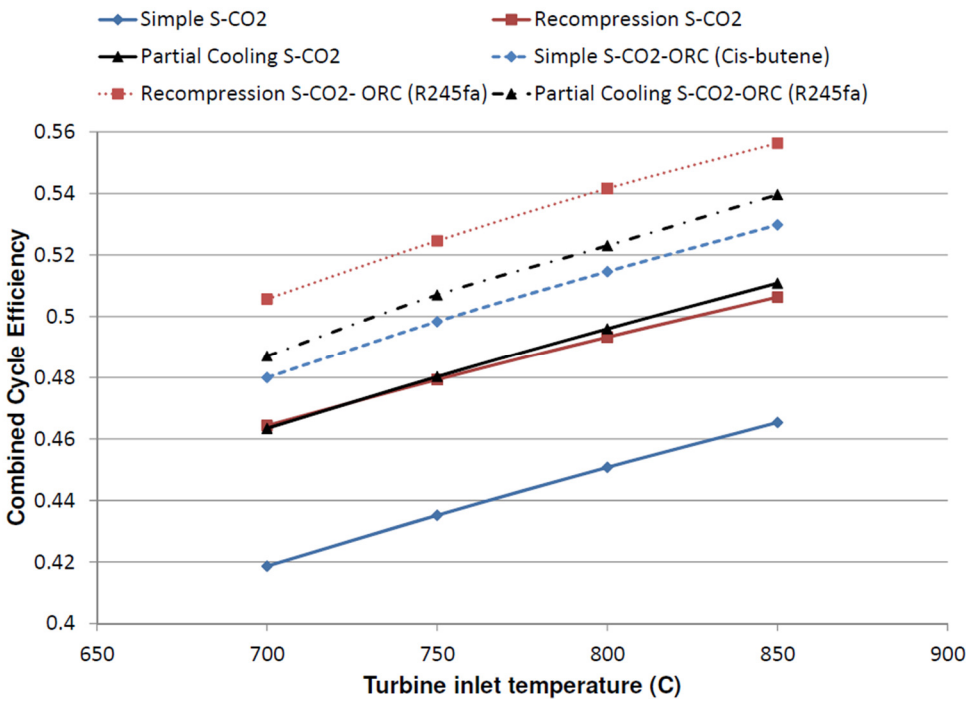


Figure 5-16 Performance comparison of the combined and the single cycles

The efficiencies of the partial cooling and the recompression cycles are almost equal at similar temperatures, however, the recompression cycle presents a higher overall potential when used as the top cycle in conjunction with an ORC. In addition, the recompression cycle operates at lower pressure ratios that can be considered as an advantage over the partial cooling cycle. Amongst the working fluids considered for the ORC, Butene and Cis-butene are found to be most appropriate for each of the combined cycle configurations on the basis of global efficiency and expansion ratio. Final selection of the working fluid, however, would necessarily include consideration of these factors and other relevant criteria that are outside the scope of this study, e.g., availability and cost of suitable turbomachinery, compromise between heat exchanger pressure rating and cost, operational issues (freezing point, negative condenser pressure, pump cavitation) fluid toxicity and tribological factors, etc.

# CHAPTER 6 DEVELOPING A DIRECT S-$CO_2$ SOLAR RECEIVER BASED ON COMPACT HEAT EXCHANGER TECHNOLOGY[4]

## 6.1 Introduction

Carbon dioxide is a non-toxic, abundant, inexpensive, non-flammable and highly stable compound with low critical properties which have recently been proposed to be used in CSP plants [17]. It has been demonstrated that supercritical carbon dioxide (s-$CO_2$) Brayton cycles are capable of achieving more than 50% efficiency at operating conditions that could be met in power tower type CSP systems [20] [93]. Moreover, using carbon dioxide as the heat transfer fluid (HTF) eliminates the existing problems with oil, molten salt, and steam. These problems can be summarized as maximum operating temperature limit, required freeze protection units, and complex control systems [19].

On the other hand, s-$CO_2$ power cycles operate at very high pressures (close to 20 MPa). Such a high pressure introduces some uncertainties about utilization of s-$CO_2$ as the HTF in the CSP plants. A major problem is to design a receiver which can tolerate the high pressure while maintaining good thermal performance. In the tubular receivers, thicker tubes are required, which results in a reduction in the heat transfer rate. Regular windowed receivers are also not suitable for this application since they must be thin for minimal radiation attenuation and cannot tolerate the high pressure. Therefore, an innovative design is required to guarantee the mechanical strength as well as the superior thermal performance. Since 2012, U.S. Department of Energy "SunShot Concentrating

[4] This chapter has been submitted to the Journal of Solar Energy Engineering for publication.

Solar Power R&D" program has funded new projects to develop solar receivers for s-CO2 cycles [83]. These projects are mainly in the first stages of development and no detailed document exists yet about the design and operation of these receivers.

Considering the limitations of the existing solar receivers, compact heat exchangers (CHE) are considered as promising candidates to be used in the future CSP plants [94]. CHEs are recognized as highly efficient, small size heat exchangers that have been extensively used in different areas such as automotive, aerospace, electronics, etc [95]. The main characteristics of these heat exchangers are the high heat transfer surface area per unit volume (over 700 $\frac{m^2}{m^3}$) and small hydraulic diameters (less than 6 mm) [96]. There are different types of CHEs, which are well-documented in [94] [95]. Depending on the type of the heat exchanger and manufacturing method, some types of CHEs are able to operate at very high pressures. According to [94], plate fin heat exchangers and printed circuit heat exchangers (PCHE) that are diffusion bonded can tolerate pressures as high as 60 MPa. Diffusion bonding is a joining process wherein the atoms of two solid integrate over time under elevated temperature and the interfaces between the joints are eliminated; Therefore, the strength of the base material is preserved and the heat exchanger can operate at high pressures [97]. Considering the operating pressure for s-$CO_2$ receivers (around 20 MPa), diffusion bonded CHEs seems to be a perfect candidate from mechanical as well as thermal point of view.

There have been few studies conducted on employing CHEs as the solar receivers in the CSP plants. Vrinat et al. [98][99] investigated using PCHE with semi-circular channels to heat air from 550℃ to 750℃ under average flux density of 600 $\frac{kW}{m^2}$. Grange et al. [100] studied the performance of a CHE with three rows each including 15 tubes made of Inconel 600 , which was immersed in a copper matrix. Each tube was equipped with a helical band made of Inconel 600 in order to enhance the heat transfer at the expense of pressure loss. Li et al. [101] investigated the performance of a

CHE under solar flux density of 170-470 $\frac{kW}{m^2}$ to heat air flowing inside twelve micro-channels with rectangular ribs and found heat transfer coefficient close to 750 $\frac{W}{m^2K}$.

In this chapter, a CHE is designed to heat s-$CO_2$ up to 700℃ using squared-shape channels. Inconel 625 is selected as the heat exchanger material because of its low corrosivity in s-$CO_2$ environment. First, the computational model of the heat exchanger is developed and validated against the available data in the literature. Then, the thermal as well as mechanical performance of the heat exchanger is evaluated by parametric analysis. Finally, a multi-objective optimization is carried out to find the optimal geometry of the system. The objective functions are defined as unit thermal resistance of the CHE and pressure drop across the channels, to be minimized. The mechanical strength of the CHE is defined as a constraint in the optimization code, which is evaluated using ASME code for pressure vessels.

## 6.2 Computational Model

It is first necessary to develop heat transfer as well as pressure drop models in order to design and optimize the CHE. The heat transfer model developed by Lei et al. [102] [103] is employed in this study. The detailed explanation of the model is given in [103], however, a brief description is provided in the following section.

### 6.2.1 Heat Transfer Model

A three dimensional thermal resistance network is developed to find the bulk flow temperature inside the channels as well as the surface temperature profile. Figure 6-1 depicts the geometric configuration and the resistance network model. Two heat transfer mechanisms, i.e. conduction through the solid matrix and convection to the fluid, are taken into account using the resistance network model. It is assumed that a constant heat flux is applied to the top surface.

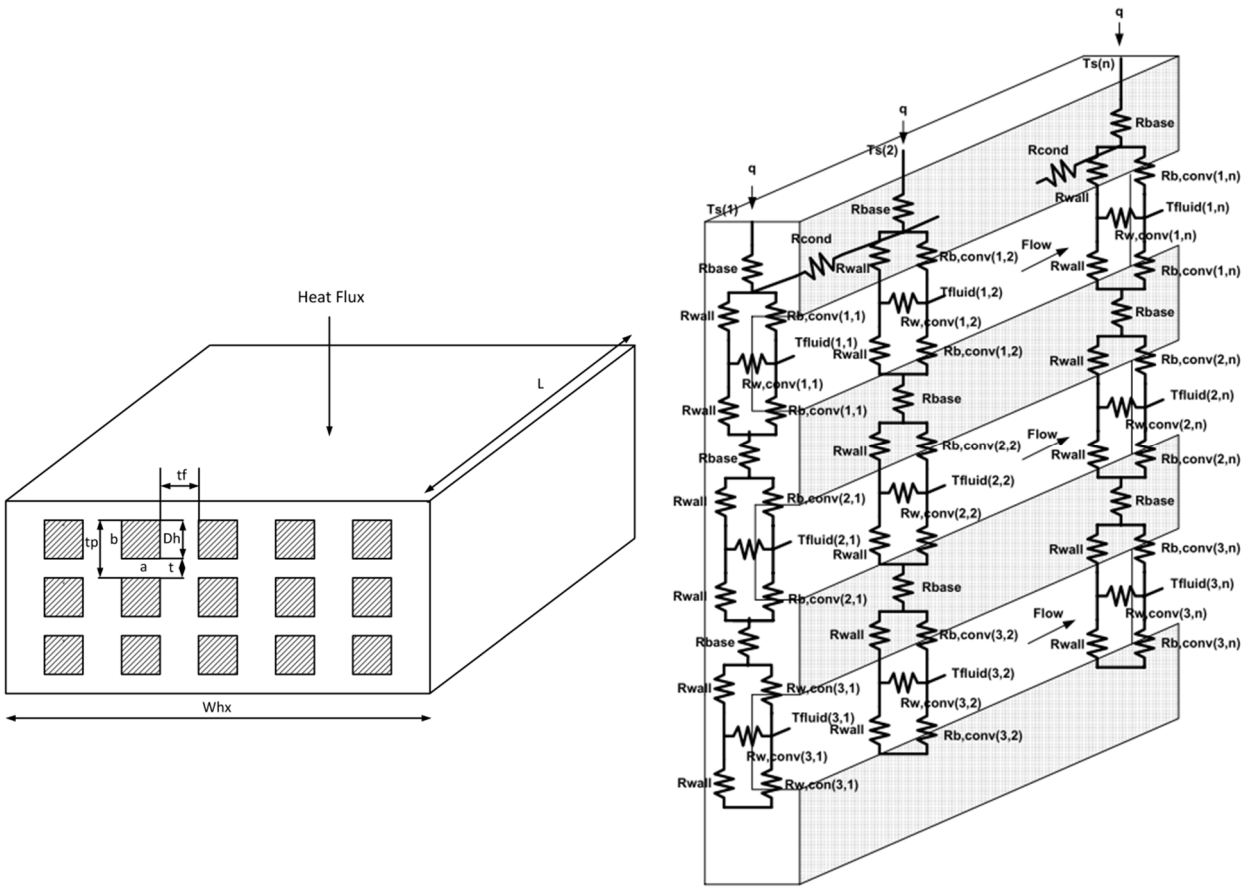


Figure 6-1 Left) Geometric configuration of CHE. Right) Thermal resistance network [102]

Due to the symmetry of the system, only half of the channels and walls are considered and the remaining surfaces are assumed adiabatic. The heat exchanger is divided into $n$ unit grids along the axial direction.

The base resistance is calculated as:

$$R_{base} = \frac{t}{k_s \times \frac{1}{2}(t_f + a) \times l_n} \tag{6-1}$$

where $l_n = L/n$. Conduction resistance through the side walls are given as:

$$R_{wall} = \frac{b}{k_s \times t_f \times l_n} \tag{6-2}$$

The conduction resistance along the axial direction can be found by:

$$R_{cond} = \frac{l_n}{k_s A_{equi}} \tag{6-3}$$

where $A_{equi}$ is the conduction equivalent area. The heat is transferred to the fluid through the side and base walls. The convection resistance from the side wall is given as:

$$R_{w,conv} = \frac{1}{h_c \times b \times l_n} \tag{6-4}$$

The convection resistance from base wall is given as:

$$R_{b,conv} = \frac{2}{h_c \times a \times l_n} \tag{6-5}$$

The convective resistances are dependent on the heat transfer coefficient, which varies along the channels; therefore, they need to be calculated grid by grid.

The heat flux to each channel is different and depends on the local wall temperature, local heat transfer coefficient, and bulk fluid temperature. The heat flux entering each channel can be found using mesh current analysis [102]. Once the heat flux for each channel is calculated, the bulk fluid temperature can be found as:

$$T_{bulk,f}(l,k) = T_{f,in} + \frac{m}{\dot{m} \times C_p} \sum_{i=1}^{k} q(l,i) \tag{6-6}$$

where $l$ represent the row number and $k$ is the grid number in the axial direction. Having the bulk fluid temperature, the equivalent thermal resistance from the junction to the fluid can be calculated as:

$$R_{eq}(l,k) = \frac{T_j(k) - T_{bulk,f}(l,k)}{q(l,k)} \tag{6-7}$$

Writing energy balance around grid $k$ and putting all junction temperatures on one side lead to:

$$-T_j(k-1)+\left[2+R_{cond}\sum_{l=1}^{m}\frac{1}{R_{eq}(l,k)}\right]T_j(k)-T_j(k+1)=R_{cond}\left[q+\sum_{l=1}^{m}\frac{T_{bulk,f}(l,k)}{R_{eq}(l,k)}\right] \quad (6\text{-}8)$$

Therefore, a system of linear equations is obtained for $n$ unknown junction temperatures which need to be solved by enforcing adiabatic boundary conditions at the front and back surfaces of the heat exchanger. As the surface temperature distribution and heat flux to the channels are coupled variables, an iteration loop is required for solution to converge.

For fully developed laminar flow inside the rectangular channel ($Re$<2300), Hesselgreaves [95] recommends the following correlation for calculating Nusselt number:

$$Nu = 8.235\,(1-2.0421\alpha_a+3.0853{\alpha_a}^2-2.4765{\alpha_a}^3+1.0578{\alpha_a}^4-0.1861{\alpha_a}^5)$$

where $\alpha_a$is the aspect ratio and is 1 for square-shaped channels.

Nusselt number in turbulent region ($Re > 5000$) is found using Gnielinski correlation [104]:

$$Nu=\frac{\frac{f_c}{8}\,(Re-1000)Pr}{1+12.7\,(Pr^{2/3}-1)\sqrt{\frac{f_c}{8}}} \quad (6\text{-}10)$$

where $Pr$ is the Prandtl number and $f_c$ is given as:

$$f_c=\left(\frac{1}{1.8\log Re-1.5}\right)^2 \quad (6\text{-}11)$$

This equation is valid for Prandtl numbers ranging from 0.5 to 2000, and Reynolds numbers up to $5\times10^6$. For the range of Reynolds numbers between 2300 to 5000, which is known as the transitional region, linear interpolation is used to find the Nusselt numbers [85]:

$$Nu=Nu_{laminar,2300}+\frac{Nu_{turbulent,5000}-Nu_{laminar,2300}}{5000-2300}\,(Re-2300) \quad (6\text{-}12)$$

Having the Nusselt numbers from these equations, the temperature of the fluid inside the channels and temperature profile of the heated surface can be found using the iteration technique.

6.2.2 Pressure Drop Model

The pressure drop inside the CHE is due to entrance loss, friction loss, and exit loss. The gravitational loss is not taken into account. The entrance and exit losses can be estimated by:

$$\Delta P = C\rho\frac{V^2}{2}\ /1000 \tag{6-13}$$

where $C$ is the loss coefficient, which is assumed 0.5 for the entrance and 1.0 for the exit [85], $\rho$ is the local fluid density ($\frac{kg}{m^3}$) and $V$ is the local fluid velocity ($\frac{m}{s}$).

The pressure drop due to friction loss is calculated by:

$$\Delta P = (f\frac{L}{D_h}\rho\frac{V^2}{2})/1000 \tag{6-14}$$

where $D_h$ is the hydraulic diameter, $L$ is the length, and $f$ is the friction factor which has to be determined from correlations. The friction factor correlations are given in [105] for different ranges of Reynolds number and relative roughness, i.e. surface roughness over hydraulic diameter. In this research, the surface roughness is taken as $10^{-5}m$ in all calculations.

According to [105], the Reynolds number at which the curve of friction factor departs from the Hagen-Poiseuille law is determined by:

$$Re_0 = 754\exp\left(\frac{0.0065}{\bar{\Delta}}\right) \tag{6-15}$$

where $\bar{\Delta}$ is the relative roughness and this equation is valid when $\bar{\Delta} > 0.007$. For $\bar{\Delta} \leq 0.007$, the departure Reynolds number is 2000. For laminar flows, i.e. Reynolds number less than $Re_0$ , the friction factor is determined by:

$$f = \frac{64}{Re} \tag{6-16}$$

The boundaries of the transition region at which the friction factor increases continuously are determined by:

$$Re_1 = 1160 \left(\frac{1}{\bar{\Delta}}\right)^{0.11} \tag{6-17}$$

$$Re_2 = 2090 \left(\frac{1}{\bar{\Delta}}\right)^{0.0635} \tag{6-18}$$

For $\bar{\Delta} \leq 0.007$, $Re_1 = 2000$. For the range of $Re_0 < Re < Re_1$, the friction factor is evaluated as:

$$f = 4.4\, Re^{-0.595} \exp\left(-\frac{0.00275}{\bar{\Delta}}\right) \tag{6-19}$$

For the range of $Re_1 < Re < Re_2$, the friction factor is given as:

$$f = (f_2 - f^*) \exp\{-[0.0017\ (Re_2 - Re)]^2\} + f^* \tag{6-20}$$

where at $\bar{\Delta} \leq 0.007$, $f^* = f_1$, and $f^* = f_1 - 0.0017$ for $\bar{\Delta} > 0.007$. The factor $f_1$ is given as:

$$f_1 = 0.032 \qquad \text{for } \bar{\Delta} \leq 0.007 \tag{6-21}$$

$$f_1 = 0.075 - \frac{0.0109}{\bar{\Delta}^{0.286}} \quad \text{for } \bar{\Delta} > 0.007 \tag{6-22}$$

Dostal suggested that $f_2$ can be calculated from the Colebrook-White correlation, as shown in the following paragraph, by substituting $Re_2$ for the Reynolds number.

Finally, the friction factor in the turbulent region can be calculated using Colebrook-White correlation as:

$$f = \frac{1}{\left[2 \log_{10}\left(\frac{2.51}{Re\sqrt{f}} + \frac{\bar{\Delta}}{3.7}\right)\right]^2} \tag{6-23}$$

There is a small difference in pressure drop between the channels, therefore, the overall pressure drop is found by averaging the pressure drops in all the channels.

### 6.2.3 Computational Algorithm

In this study, the fluid inside the channels is gas; therefore, the pressure and temperature are coupled and need to be found simultaneously. The algorithm that is used to find the bulk fluid temperature and top surface temperature profile are shown in Figure 6-2. The program is developed

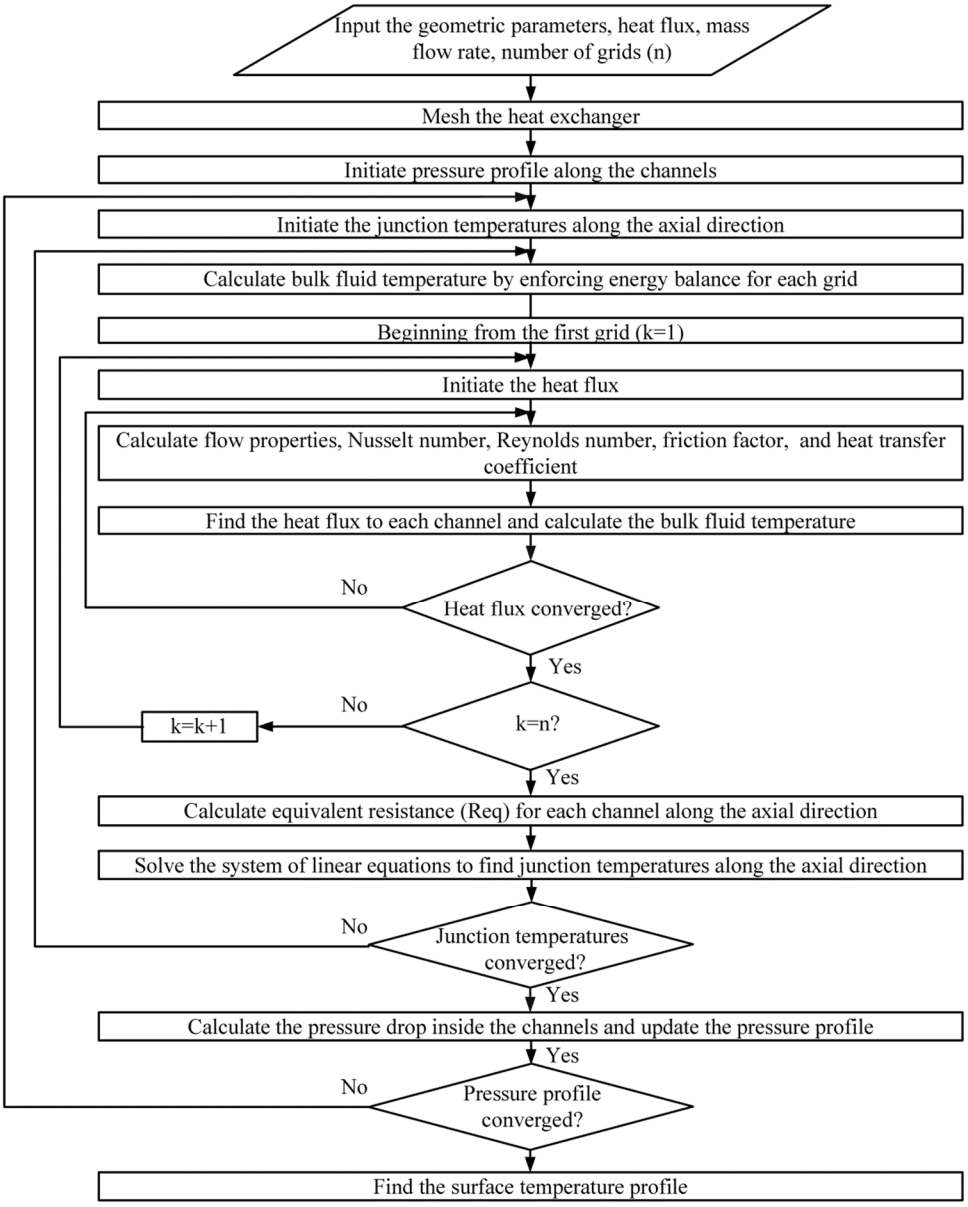


Figure 6-2 Flowchart for calculating the bulk fluid and top surface temperatures

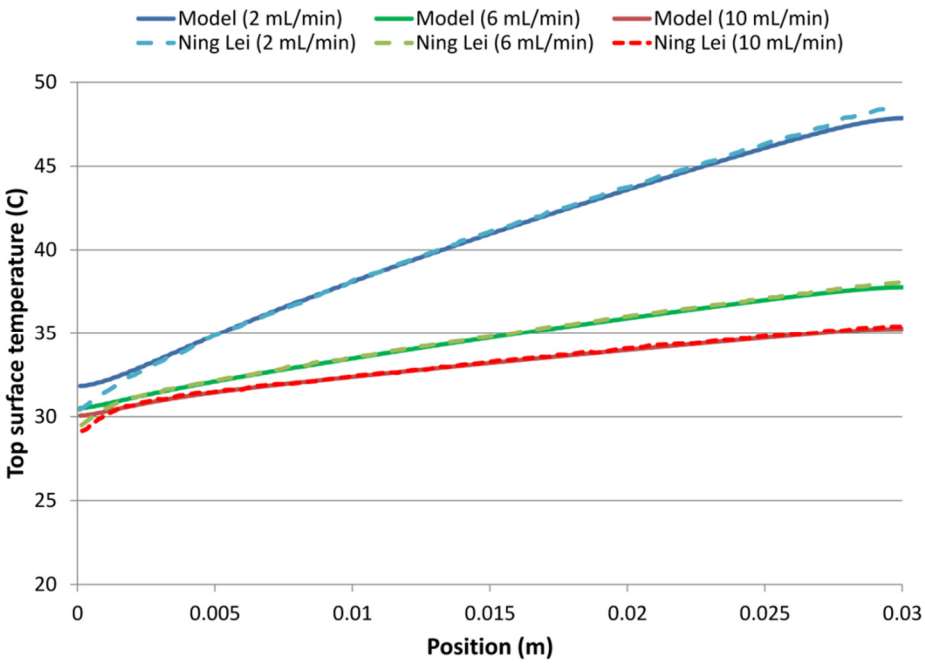


Figure 6-3 Comparison of top surface temperature with Ning Lei [103]

in MATLAB [58] and Refprop [84] is used to find the thermo-physical properties at different temperatures and pressures. In order to validate the model, the predictions of the model are compared with the results given by [103]. Figure 6-3 compares the temperature distributions on the top surface of a CHE with three parallel channels for different volumetric flow rates of water. The CHE is made of SiC with the heat conductivity of 15 $\frac{W}{mK}$. A total 2 Watts of uniform heat flux is applied to the top surface.

As can be clearly seen from the figure, the model is able to predict accurate values. The small difference at inlet of the channel is due to the entrance effect. It is noteworthy that the results given by [103] were already validated against experimental data.

### 6.3 Developing a CHE Solar Receiver for S-$CO_2$

There are different configurations of s-$CO_2$ Brayton cycle that are proposed for solar thermal power plants. A detailed description about these configurations and their potentials to be used with a

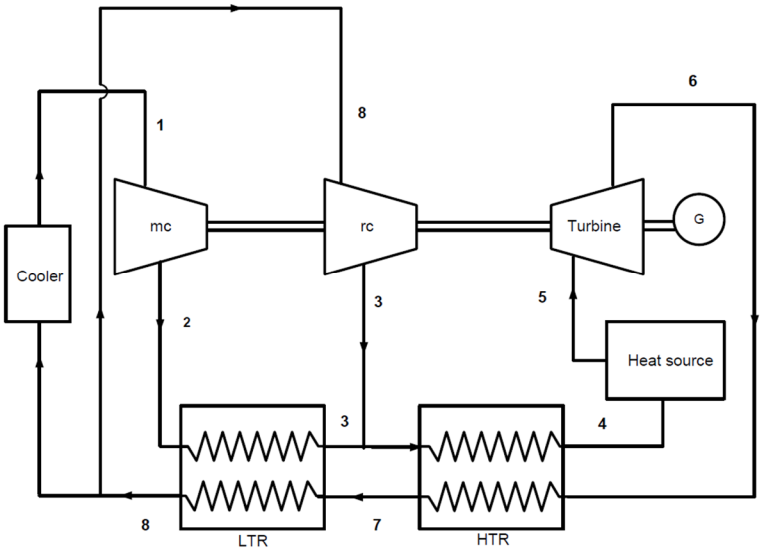


Figure 6-4 Schematic of a recompression s-$CO_2$ Brayton cycle

bottoming cycle for CSP applications is given in chapter 1. In this study, a recompression s-$CO_2$ Brayton cycle is considered. As can be seen from Figure 6-4, after expanding in the turbine the flow is directed into high temperature recuperator (HTR) and low temperature recuperator (LTR) to preheat the high pressure stream. After leaving the low temperature recuperator (LTR) the flow is divided into two streams. A fraction of the flow rejects heat to the cold sink and exits to the main compressor (mc) while the other fraction is pressurized in a recompression compressor (rc). The two streams are mixed at point 3, and the mixed stream enters a high temperature recuperator (HTR) and a heater, where thermal energy is added to achieve the required turbine inlet temperature. In this study the heat source is replaced by a solar receiver. The maximum temperature and pressure of the cycle, i.e. turbine inlet condition, are set at 700 ℃ and 20 MPa, respectively. Running the cycle under optimized pressure ratio when the cooler exit temperature is 35℃, the temperature entering the solar receiver is obtained as 530 ℃. In other words, the flow needs to be heated from 530℃ to 700 ℃ inside the solar receiver. The detailed description of the cycle thermodynamic analysis is given in [93].

Selection of the appropriate material for the CHE is also of great importance and both thermal performance and corrosively in s-$CO_2$ environment need to be taken into account. Corrosion of different engineering alloys in the presence of s-$CO_2$ is investigated in the literature [106][107][108] and Inconel 625, which is a nickel-based alloy, has shown good corrosion resistance. The detailed engineering properties of this material can be found in [109]. The thermal conductivity of the material is taken as 20.8 $\frac{W}{m\,℃}$ and the maximum operating temperature limit is 982°C [110].

6.3.1 Parametric Study

According to [85], the maximum plate width and length that are currently available are 600 mm and 1500 mm. In the parametric study the width and length are fixed at 600 mm and 500 mm, respectively. The plate thickness is also set at 3 mm. It is assumed that s-$CO_2$ enters the CHE and removes heat from the top surface where a solar flux density of 500 $\frac{kW}{m^2}$ is applied.

Thermal performance of the receiver is evaluated by defining unit thermal resistance as [102]:

$$RR = \left(\frac{\overline{T_s} - T_{f,in}}{q^{"}}\right) \times 10000 \qquad (6\text{-}24)$$

where $\overline{T_s}$ is the mean surface temperature. As it is expected, lower unit thermal resistance represents better thermal performance of the receiver. In this study, the influences of varying hydraulic diameter, number of layers, and distance between the channels on unit thermal resistance and pressure drop are studied.

*6.3.1.1 Effect of Hydraulic Diameter*

Figure 6-5 shows the variations of unit thermal resistance with respect to the hydraulic diameter for different mass flow rates. It is noteworthy that squared-shape channels are only

considered in this study where the hydraulic diameter is equal to the side of the channel. There are three layers of channels and the distance between the channels are set at 2.4 $mm$. As can be clearly seen, the unit thermal resistance increases by having larger channels. In other words, the thermal performance deteriorates by increasing the hydraulic diameter. Moreover, having higher mass flow rates is more appropriate from thermal point of view. On the other hand, increasing mass flow rate is accompanied by the higher pressure drop, as shown in Figure 6-6. In addition, pressure drop

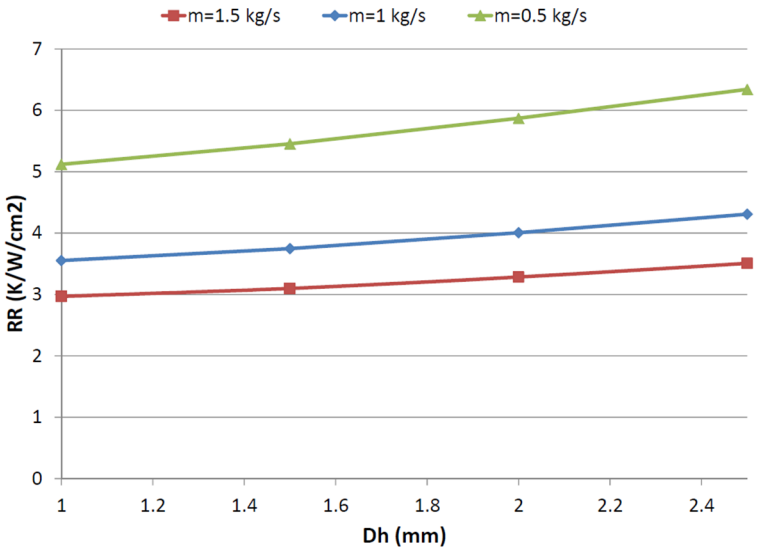


Figure 6-5 Variations of unit thermal resistance with hydraulic diameter

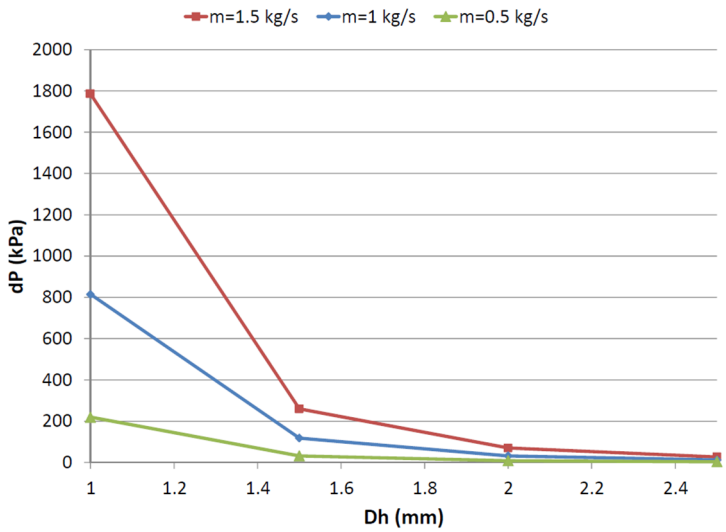


Figure 6-6 Variation of pressure drop with hydraulic diameter

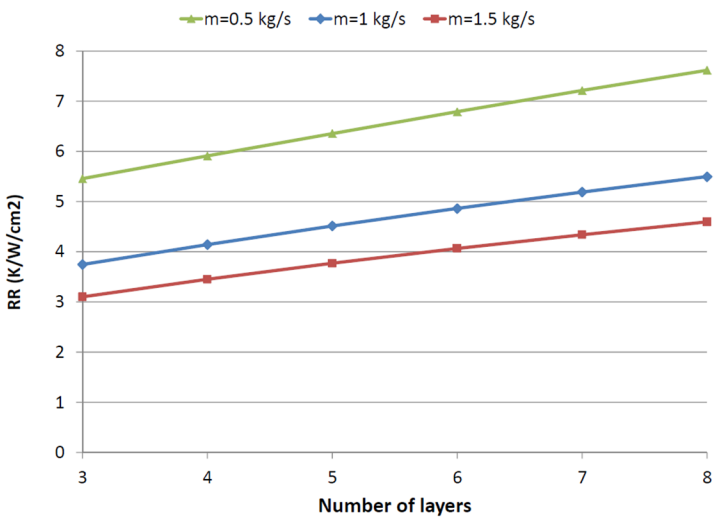


Figure 6-7 Variations of unit thermal resistance with number of layers

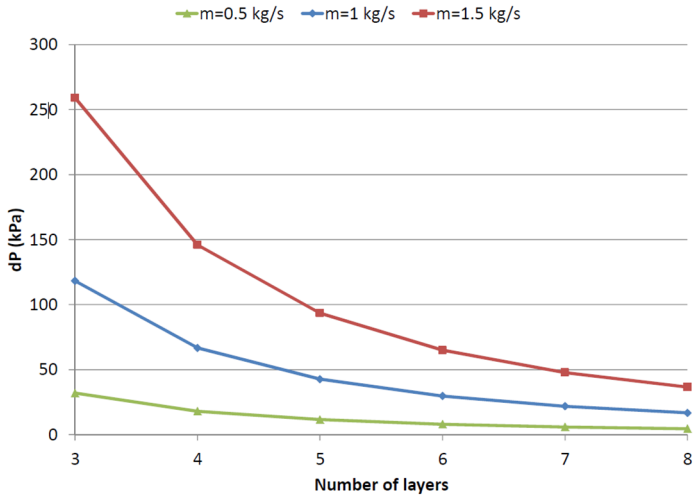


Figure 6-8 Variations of pressure drop with number of layers

decreases by having larger channels. Therefore, there is a conflict between thermal and mechanical performances with respect to the channel size, where increasing one of them leads to the deterioration of the other.

*6.3.1.2 Effect of Number of Layers*

The influence of number of layers on unit thermal resistance is shown in Figure 6-7. The hydraulic diameter and distance between the channels are taken as 1.5 mm and 2.4 mm,

respectively. According to the figure, by increasing the number of layers the unit thermal resistance increases, which is mainly due to the conductive resistance between the layers. On the other hand, increasing the number of layers leads to the reduction of pressure drop inside the channels (Figure 6-8). The main reason is that increasing the number of layers results in increasing the number of channels, which consequently leads to lower mass flow per channel. Therefore, there exists again a conflict between thermal and mechanical performances of the system.

*6.3.1.3 Effect of Distance Between the Channels*

As the width of the CHE is fixed, the number of channels in a layer varies with changing the distance between them, i.e. less number of channels are obtained by increasing the distance and vice versa. The influence of this parameter on the unit thermal resistance and pressure drop for different mass flow rates are shown in Figure 6-9 and Figure 6-10. As it is expected the unit thermal resistance does not vary much by increasing $t_f$, however, the pressure drop increases continuously. The presented parametric study shows that the thermal and mechanical performances of the CHE are in conflict with each other. In other words, improving one result in the deterioration of the other; therefore, a multi-objective optimization is required.

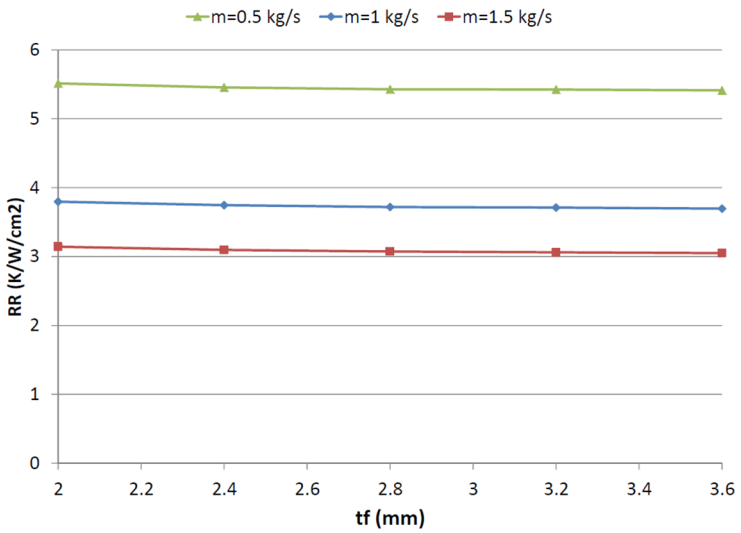


Figure 6-9 Variations of unit thermal resistance with the distance between the channels

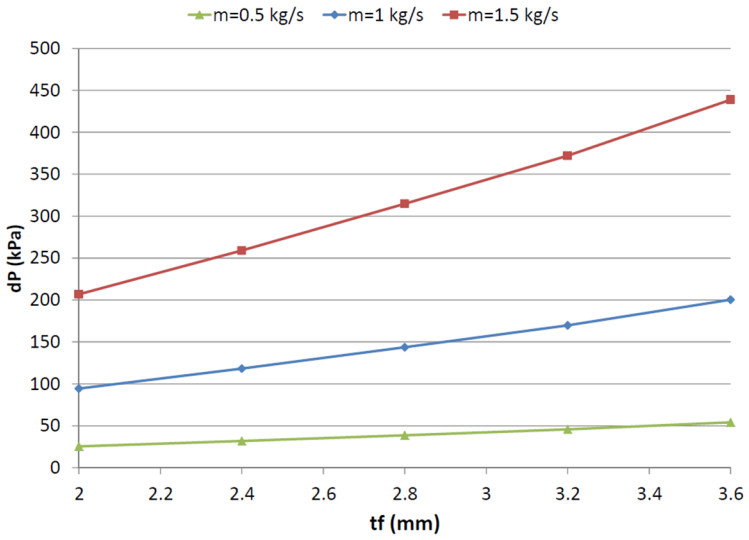


Figure 6-10 Variations of pressure drop with the distance between the channels

### 6.3.2 Multi-objective Optimization of the CHE

Two output parameters, namely unit thermal resistance and pressure drop, are considered as the objective functions. Clearly, it is expected that both objective functions to be minimized simultaneously. The design variables are defined as hydraulic diameter, number of layers, and distance between the channels in a single layer, which has to be optimally determined based on multi-objective Pareto approach.

The main constraint that needs to be incorporated into the program is the mechanical strength of the CHE. The optimization program can lead to a design which may not be viable from mechanical strength point of view. According to [111], ASME boiler and pressure vessel code [112] can be safely used to examine if the design meet the mechanical strength requirements. It is always essential to maintain:

$$S_m < S \times E \tag{6-25}$$

and

$$S_T < 1.5 \times S \times E \tag{6-26}$$

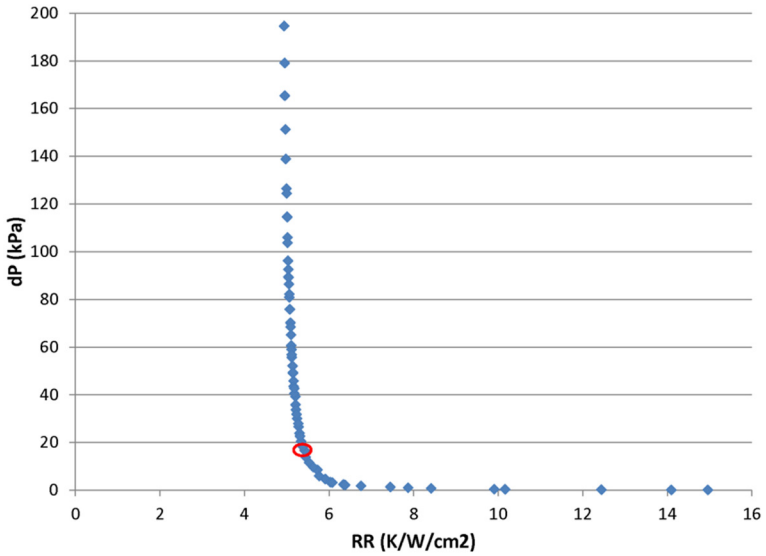


Figure 6-11 Pareto front of pressure drop and unit thermal resistance

where $S_m$ is the membrane stress, $S$ is the design stress, $S_T$ is the total stress, and $E$ is the joint factor which is given as 0.7 for the diffusion bonded blocks [111]. The detailed equations for calculating the membrane and total stresses at different parts of the channels are given in [111] and [112]. The design stress for Inconel 625 is taken as 107 ksi [109]. The side margin thickness, which is the distance between the side wall and the first channel, and the plate thickness are taken as 5 mm. Other parameters are the same as those given in the parametric study section. It is noteworthy that the length of the CHE is set as 0.5 $m$ during the optimization. However, this may not be enough to reach the required outlet temperature (700℃); therefore, the length of the receiver is updated later to meet the design criteria.

The evolutionary process of optimum selection of the design variables vector to obtain the Pareto front of those objective functions is accomplished with a population size of 60 with crossover probability, Pc, and mutation probability, Pm, of 0.9 and 0.1, respectively. The range of variations for $D_h$, $m$, and $t_f$ are 0.5-3 $mm$, 3-10 , 1-5 $mm$, respectively, Apparently, the number of layers, $m$ , has to be an integer number.

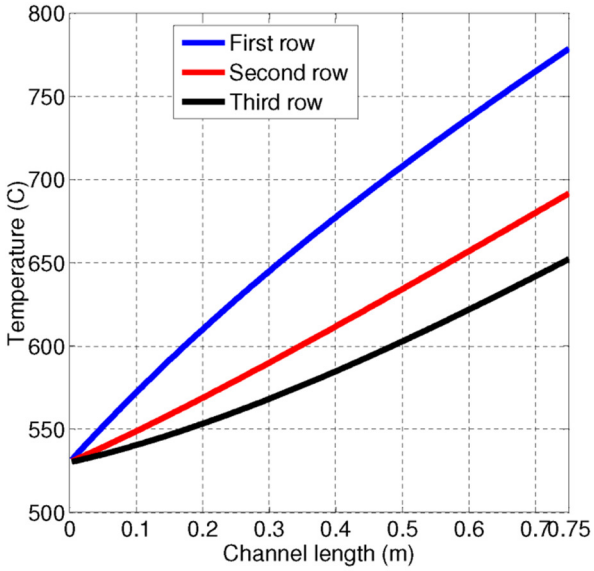


Figure 6-12 Temperature profile of flow in the channels of the optimized CHE

Non-dominated optimum design points for the unit thermal resistance and pressure drop are shown in Figure 6-11. The maximum pressure drop in this figure is 200 $kPa$, which is 1% of the inlet pressure. As can be observed from the figure improving one objective function leads to deterioration of the other. Having a trade-off between the functions, the point that is shown with the circle can be considered as an appropriate design point. At this point hydraulic diameter, number of layers, and distance between the channels are given as 2.8 $mm$, 3, 5 $mm$, respectively.

As it is already explained, the length of the CHE needs to be updated to make sure the desired output temperature is achieved. This can be done by running a simple iterative program until the average temperature of the flow leaving the channels reaches 700℃. Accordingly, the length of the CHE is updated to 0.75 m.

Figure 6-12 depicts the temperature profiles in three layers of the optimized CHE. As it is expected, the temperature variation in the first row is the largest and continuously decreases in the adjacent rows. However, the average temperature of the flow leaving the CHE is 707℃. Temperature profile of the top surface, where the heat flux is applied, is shown in Figure 6-13.

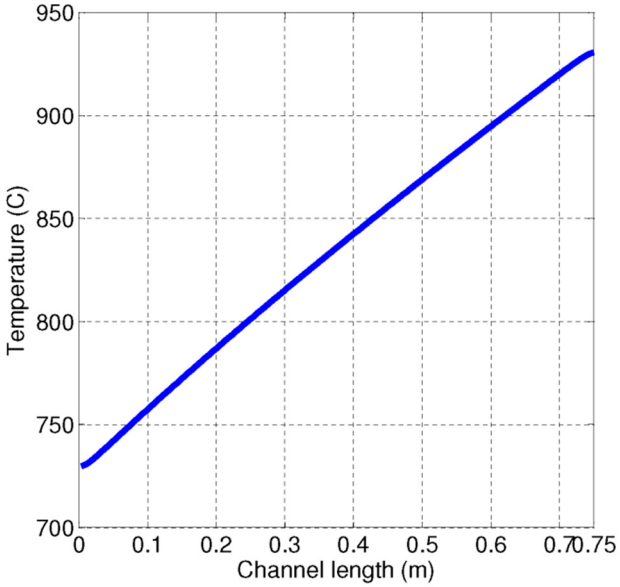


Figure 6-13 Temperature profile of the surface receiving the heat flux

According to the figure, the temperature continuously increases from 730℃ to 930℃. Therefore, not only the heat from the surface is efficiently removed, but also the surface temperature is remained below the maximum operating temperature limit of Inconel 625, which is 982℃ [110].

**6.4 Summary and Concluding Remarks**

A solar receiver based on the compact heat exchanger technology was developed for a recompression Brayton cycle. The heat transfer and pressure drop models were presented and validated against the published data. Inconel 625 was selected as the base material because of its low potential for corrosion in s-$CO_2$ environment. Based on the thermodynamic analysis it was determined that the receiver needs to heat up 1 $\frac{kg}{s}$ of s-$CO_2$ from 530 ℃ to 700 ℃. A parametric study was carried out to assess the influences of hydraulic diameter, number of layers, and distance between the adjacent channels on the unit thermal resistance and pressure drop. The parametric analysis revealed the existence of conflict among the output parameters. Therefore, a multi-objective optimization was performed using genetic algorithm to find the Pareto front of unit thermal

resistance and pressure drop. The mechanical strength of the CHE was evaluated using ASME code for the pressure vessels. With the aid of the Pareto front, an optimal geometry was proposed for the receiver. It was shown that s-$CO_2$ can be heated up inside the receiver under flux density of 500 $kW/m^2$ from 530 ℃ to 700 ℃ while the surface temperature is remained below the maximum temperature limit of Inconel 625.

# CHAPTER 7 PERFORMANCE EVALUATION OF A 3 $MW_{th}$ S-$CO_2$ RECEIVER

## 7.1 Introduction

Models for the sub-systems of a solar power tower plant were developed in the previous sections. In this chapter, all those models are integrated together to assess the performance of a $3MW_{th}$ direct s-$CO_2$ thermal receiver in Daggett, California. First, a recompression Brayton cycle is simulated and optimized based on the information provided in chapter 5. Second, size and configuration of the thermal cavity receiver is determined with the aid of the results presented in chapter 6. Then, the heliostat field is designed using the method developed in chapter 2. Next, the heat flux distribution on the receiver surface is determined by employing the methods described in chapter 3. Finally, the thermal performance of the receiver is evaluated using the radiative and convective heat transfer models presented in chapter 4, and the receiver model in chapter 6.

## 7.2 Power Cycle

A recompression Brayton cycle (Figure 5-6) is selected as the power cycle to convert heat from the thermal receiver to electricity. The input parameters to the power cycle model are provided in Table 7-1. Optimizing the cycle performance leads to a turbine pressure ratio of 2.8 and thermal efficiency of 48.6%. The enthalpy difference between the inlet and outlet of the heat source is obtained as 214.39 kJ/kg, which needs to be provided by the thermal receiver. The temperature at the inlet of the heat source is about 530℃.

Table 7-1 Input parameters to the recompression Brayton cycle model

| | |
|---|---|
| Maximum pressure | 20 MPa |
| Maximum temperature of the cycle | 700 ℃ |
| Minimum temperature of the cycle | 35 ℃ |
| Mass flow rate of the S-$CO_2$ Cycle | 1 kg/s |
| Heat exchanger effectiveness | 0.95 |
| Total hot stream effectiveness | 0.95 |
| Pinch Point | 5 ℃ |
| Turbine efficiency | 0.90 |
| Compressor efficiency | 0.89 |

### 7.3 Cavity Receiver Size and Geometry

According to the optimization results presented in chapter 6, a CHE receiver with 0.6 m width and 0.75 length can heat 1 kg/s of s-$CO_2$ from 530℃ to 700℃ under uniform heat flux density of 500 $kW/m^2$. The optimized hydraulic diameter, number of layers, and the distance between the channels were obtained as 2.8 mm, 3, and 5 mm, respectively.

On the other hand, according to the previous section, the heat duty that needs to be provided by the thermal receiver for 1 kg/s of s-$CO_2$ is 214.39 kJ/kg. Therefore, the total number of panels required for a 3$MW_{th}$ receiver is obtained as:

$$n_{panels} = \frac{3000}{214.39} \cong 14 \tag{7-1}$$

Despite using aiming strategies to distribute the heat flux uniformly on the entire surface of a cavity receiver, the panels located at the corners are expected to receive lower heat flux; therefore, larger panels are required to reach the desired temperature, i.e. 700 ℃.

Figure 7-1 depicts the cavity receiver geometry. As can be seen, the panels that are located at the center are shorter with respect to the others. However, the width of all panels is the same, i.e. 0.6 m. The receiver is tilted 35 degree in order to receive higher heat flux from the heliostat field.

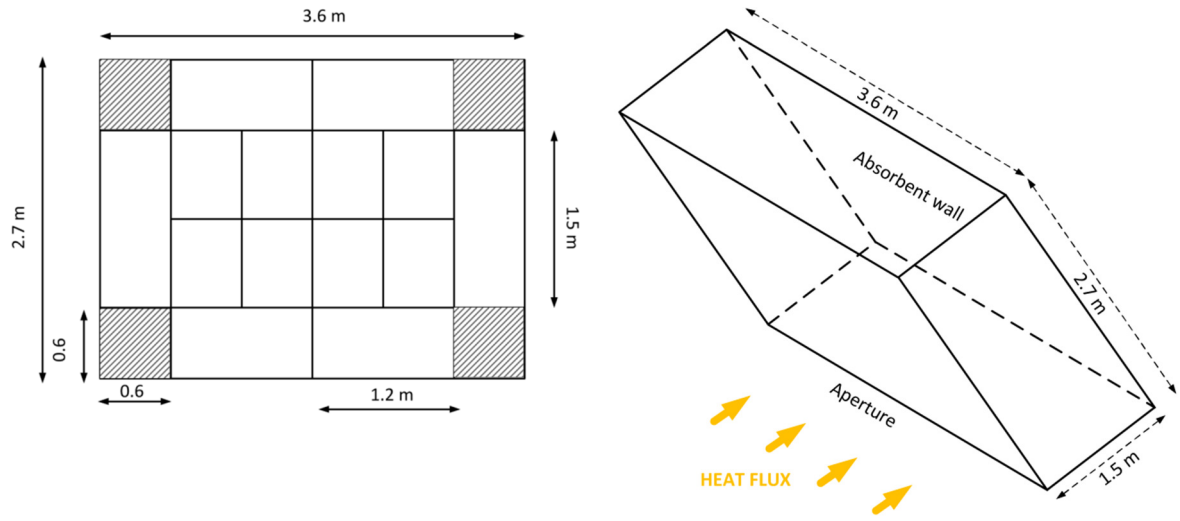


Figure 7-1 Cavity receiver geometry

### 7.4 Heliostat Field Design

A heliostat field is designed for a $3MW_{th}$ solar power tower plant in Daggett, CA using the method presented in chapter 2. The field layout is shown in Figure 7-2, which consists of 92 heliostats with 8.84 m width and 7.37 m height. Other field parameters are given in Table 7-2.

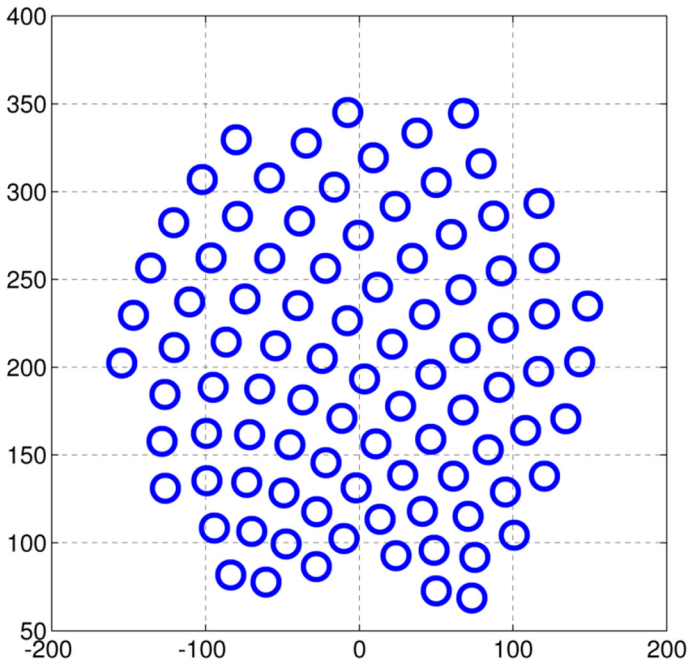


Figure 7-2 Heliostat field layout for a $3MW_{th}$ power plant in Daggett, CA

Table 7-2 Solar field parameters

| | |
|---|---|
| *Heliostats* | |
| Number of heliostats | 92 |
| Width | 8.84 m |
| Height | 7.34 m |
| Reflectivity | 0.88 |
| | |
| *Receiver* | |
| Tower height | 115 m |
| Tilt angle of the aperture | 35 $^{\circ}$ |
| Aperture width | 3.6 m |
| Aperture height | 2.7 m |

### 7.5 Heat Flux Distribution on the Receiver Surface

Heat flux distribution on the receiver surface is obtained using the analytical HFLCAL method [44], which is described in chapter 3. The slope error is taken as 1 mrad. Figure 7-3 shows the flux density distribution on March 21$^{st}$ at noon when all the heliostats are aimed at the center. The direct normal radiation in Daggett at this time of the year is given as 0.926 $\frac{\mathrm{kW}}{\mathrm{m}^2}$ by ASHRAE handbook [27]. As can be seen from the figure, the maximum and minimum heat flux densities are about 1200 $\mathrm{kW/m^2}$ and 39 $\mathrm{kW/m^2}$, respectively.

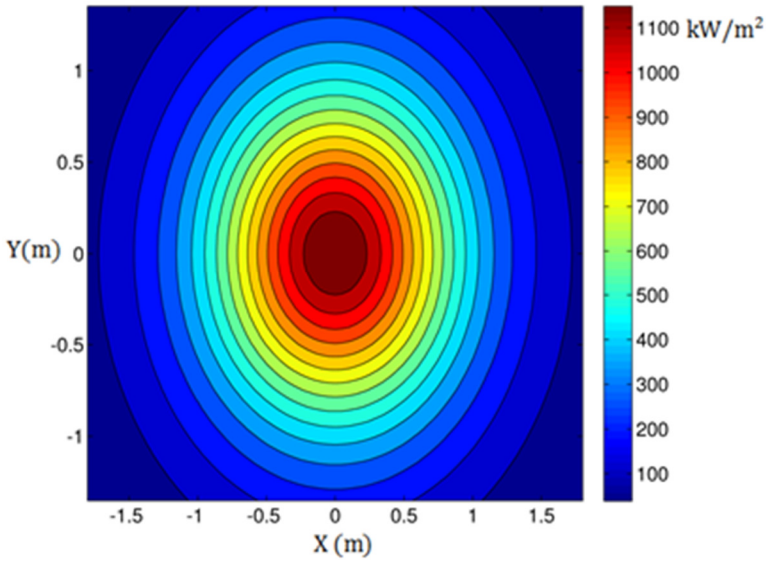


Figure 7-3 Heat flux distribution on the receiver surface on March 21$^{st}$ at noon

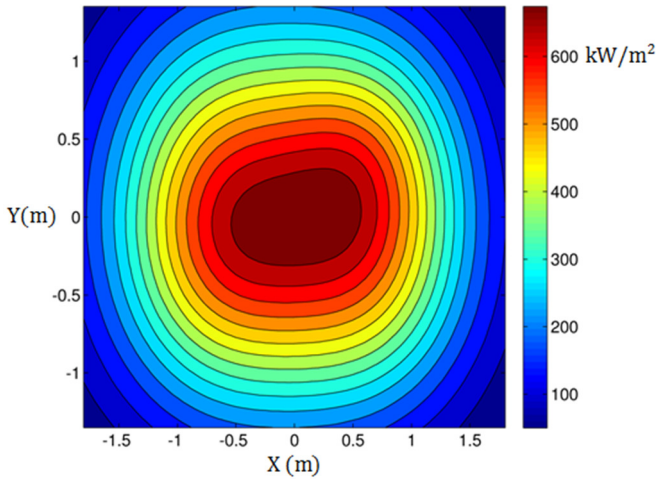


Figure 7-4 Flux distribution on March 21st at noon after employing the aiming strategy

In the next step, the optimization algorithm described in chapter 3 is employed to find the best aiming strategy. The objective function is:

$$Objective\ function = \sqrt{\frac{\sum_{i=1}^{N}(Flux(i) - 500)^2}{N}} \tag{7-2}$$

where *N* represents the number of points on which the flux density is measured.

It is intended to make mean flux density as close as possible to 500 $kW/m^2$, which is the value that was used for the design of the CHE receiver. There are 25 aiming points that are uniformly distributed on a rectangle with 1.5 m width, and 1 m height, similar to Figure 3-11. The heat flux density distribution after employing the optimization algorithm is shown in Figure 7-4. As can be clearly seen, the maximum heat flux density is reduced to about 715 $kW/m^2$ , and is more uniformly distributed along the surface.

**7.6 Computational Algorithm**

The radiative and convective heat transfer models described in Chapter 4 are employed to find the heat loss from the receiver. There are three types of surfaces inside the cavity,i.e. “active”, “inactive”, and “cornered”.

Active surfaces are those receiving solar radiation directly from the solar field and transferring energy to s-$CO_2$ using CHE technology. Energy balance for the active surfaces can be written as:

$$Flux_i\, A_i = Q_{HTF,i} + Q_{conv,loss,i} + Q_{rad,loss,i} \tag{7-3}$$

On the other hand, "inactive" surfaces are the cavity walls that do not receive direct solar radiation from the solar field. For these surfaces the energy balance is given as:

$$0 = 0 + Q_{conv,loss,i} + Q_{rad,loss,i} \tag{7-4}$$

The last term can be re-written as:

$$Q_{rad,loss,i} = A_i \sum_{j=1}^{N} \left[h_{rad,therm,i,j}\,(T_i - T_j)\right] + Q_{rad,solar,i} \tag{7-5}$$

This equation consists of the thermal as well as solar radiative heat transfer terms, as described in Chapter 4. Temperature of the surface $i$ can be found by replacing $Q_{rad,loss,i}$ in equation (7-4) (7-4) as:

$$T_i = \frac{A_i \sum_{j=1}^{N}\left[h_{rad,therm,i,j} T_j\right] - Q_{rad,solar,i} + A_i h_{c,i} T_{bulk}}{A_i \sum_{j=1}^{N}(h_{rad,therm,i,j}) + A_i h_{c,i}} \tag{7-6}$$

where $h_{conv,mix,i}$ is the convective heat transfer coefficient for surface $i$ by taking both natural and forced convection into account.

"Cornered" surfaces are located at the corners of the absorber wall and receive low level of direct of solar radiation, but do not directly contribute in heating s-$CO_2$ (hatched surfaces in Figure 7-1). Energy balances for these surfaces can be written as:

$$Flux_i\, A_i = 0 + Q_{conv,loss,i} + Q_{rad,loss,i} \tag{7-7}$$

The temperature of each surface can be found by:

$$T_i = \frac{Flux_i\, A_i + A_i \sum_{j=1}^{N}\left[h_{rad,therm,i,j} T_j\right] - \dot{Q}_{rad,solar,i} + A_i h_{c,i} T_{bulk}}{A_i \sum_{j=1}^{N}(h_{rad,therm,i,j}) + A_i h_{c,i}} \tag{7-8}$$

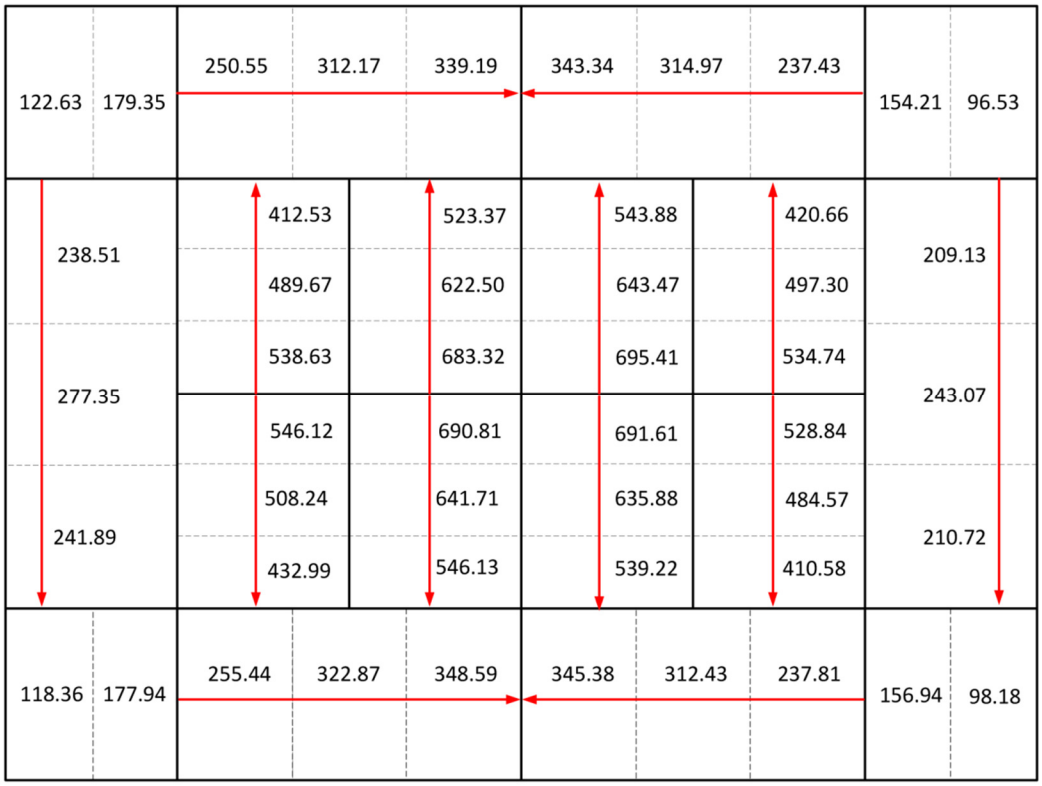


Figure 7-5 Heat flux density distribution on each panel ($kW/m^2$)

There are some parameters that need to be determined before starting the simulation, i.e. heat flux received by each active and cornered surfaces, and $\hat{F}$ factors. Therefore, an independent program is written to read the flux data shown in Figure 7-4 and transforms them into a more useful basis (Figure 7-5). The surface of each panel is divided into three equal sections and each number represents the mean value in the corresponding section. Direction of s-$CO_2$ in each panel is displayed with a red arrow. In addition, the receiver corners are divided into two sections. It can be clearly seen that the eight panels located at the center of absorber wall receive higher fluxes, however, they are shorter in length compared to other panels.

$\hat{F}$ factors can be determined by the equation presented in chapter 4:

$$\hat{F}_{ij,\lambda} = F_{ij} + \sum_{k=1}^{n} F_{ik}\,\rho_{k,\lambda}\,\hat{F}_{kj,\lambda} \tag{7-9}$$

As can be seen from the equation, one has to know the view factors between all the surfaces as well as optical properties before finding the $\hat{F}$ factors. The view factors can be determined by the analytical method described in chaper 4. Moreover, the emisivity in solar band is taken as 0.95 while it is equal to 0.1 in the thermal band. The $\lambda_{step}$ is taken as $3\mu m$. Equation (4-26) can be solved using successive substitution method [113].

Once the flux data and $\hat{F}$ factors are determined, the thermal performance of the receiver can be simulated using a program developed in MALAB. The computational algorithm of this program is shown in Figure 7-6. The program reads the flux data and $\hat{F}$ factors, and initiates the temperatures for 54 surfaces (50 surfaces shown in Figure 7-5 as well as top, bottom, and sides of the cavity). With the aid of equation (7-3), $Q_{HTF}$ is determined for each active surface, which is then used as an input for the CHE subroutine developed in chapter 6. This subroutine follows the algorithm presented in Figure 6-2 and finds out the mean surface temperature. For inactive and cornered surfaces, the new surface temperatures can be found by equations (7-6) and (7-8). Once all the surface temperatures are determined, they are compared with the previous iteration and this continues until the error reduces to less than a predetermined value, i.e. 0.01. Then, the temperature of s-$CO_2$ exiting the cavity receiver is obtained by averaging the bulk fluid temperatures leaving all the panels. Finally, the receiver thermal efficiency is determined by:

$$\eta_{rec} = \frac{Q_{transfered\ to\ the\ fluid}}{Q_{received\ by\ the\ receiver}} \times 100 \tag{7-10}$$

where

$$Q_{transfered\ to\ the\ fluid} = \dot{m}\ (h_{exit} - h_{in}) \tag{7-11}$$

and

$$Q_{received\ by\ the\ receive} = \sum_{i=1}^{50} A_i Flux_i \tag{7-12}$$

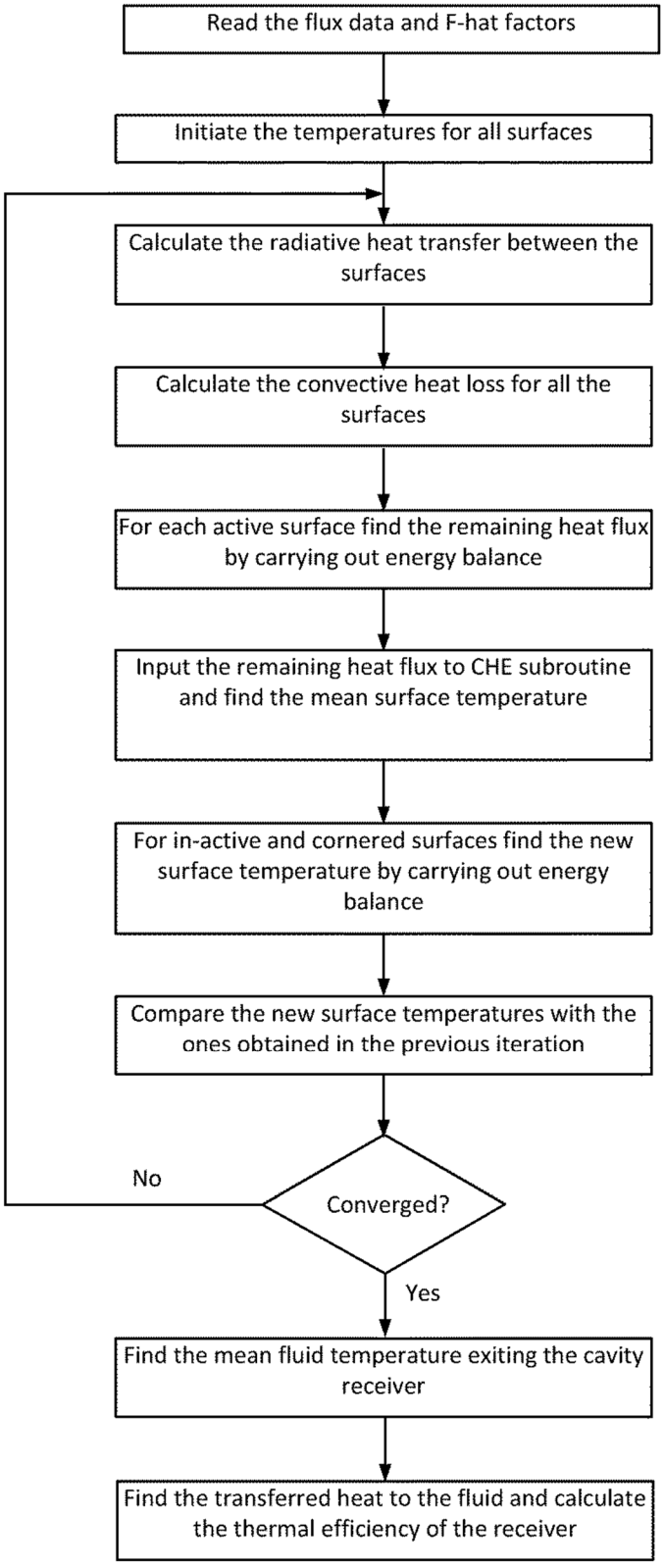


Figure 7-6 Flowchart of the program for evaluating the thermal performance

It is noteworthy that the convective heat loss is directly dependent on the wind speed. The wind speed data for Daggett, CA is taken from TMY3 data available in Systems Advisor Model (SAM)[114]. However, this data was measured at a height of 10 m, and needs to be updated to account for the increasing wind velocity at the height of the tower. Therefore, the data is updated using the following correlation which was presented by [115]:

$$\frac{V_1}{V_2} = \left(\frac{z_1}{z_2}\right)^{0.14} \tag{7-13}$$

where $V$ and $z$ represent the wind speed and height respectively.

Figure 7-7 presents the cumulative distribution functions (CDFs) of wind speed at 10 m and height of the tower (115 m) for Daggett. As can be seen, CDF is equal to 80% when the wind speed is 10 m/s at the tower. In other words, for 80% of the year the wind speed at this height is less than 10 m/s. Therefore, it can be considered as a reasonable assumption for the wind speed, which affects the convective heat loss from the cavity.

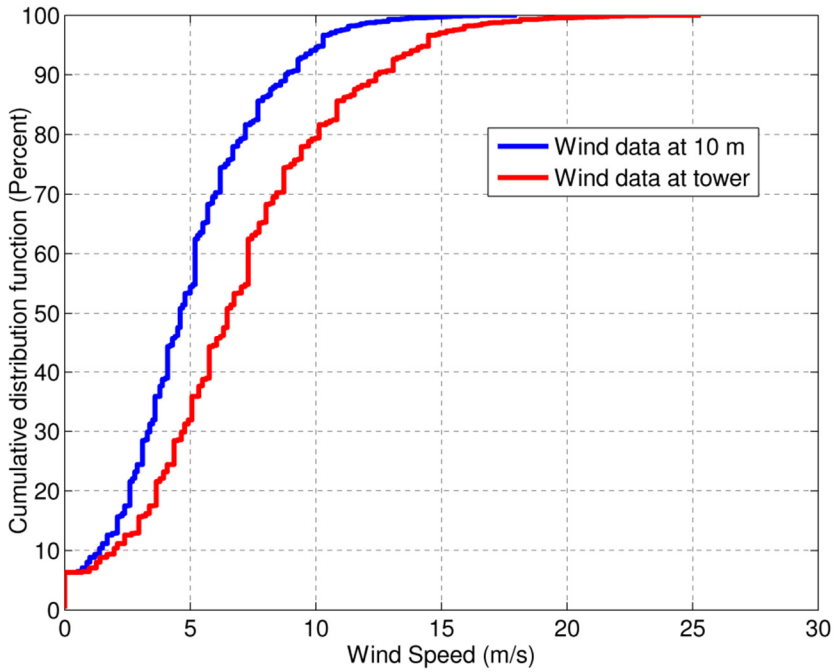


Figure 7-7 Cumulative distribution functions of wind speed for Daggett, CA [114]

### 7.7 Results

The computational algorithm described in the previous section is employed to find the bulk fluid temperature leaving the cavity receiver, as well as the surface temperatures. Figure 7-8 presents the active and cornered surface temperatures, which are shown with black numbers. The maximum surface temperature is 901℃, which is well below the maximum temperature limit of Inconel 625, i.e. 982 ℃.

In Figure 7-8, temperature of s-$CO_2$ is shown with red numbers. As it is expected, the temperature of the fluid leaving the panels that are located at the center of the cavity is higher than the target temperature, i.e. 700℃. On the other hand, s-$CO_2$ temperatures leaving other panels are less than 700℃. The average temperature between the fourteen panels is 690℃, which is close to the target temperature.

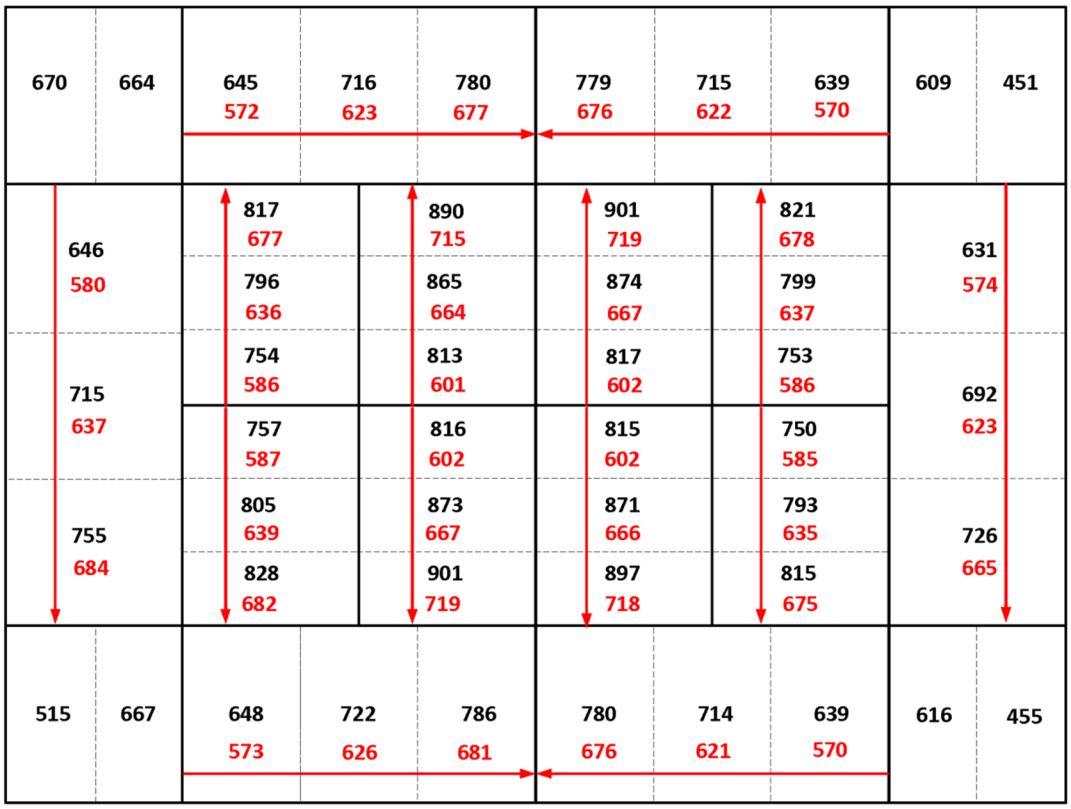


Figure 7-8 Surface (Black) and s-$CO_2$ (red) temperatures

Using equation (7-10), the receiver efficiency is obtained as 80%, which is very promising. It is noteworthy that such high efficiency is achieved even without optimizing the cavity geometry. In other words, the efficiency can be further improved with optimization.

**7.8 Summary and Concluding Remarks**

A $3MW_{th}$ cavity receiver was designed based on the principles of CHEs using 14 panels. The heliostat field was designed, and the corresponding flux distribution on the receiver surface was obtained for March 21$^{st}$ at noon. Next, the radiative and convective heat transfer models were developed, and the bulk fluid and surface temperatures were obtained. The results showed that the s-$CO_2$ reaches the design temperature while the surface temperatures remain below the maximum temperature limit of Inconel 625. The receiver efficiency was obtained as 80%, which is highly promising. The efficiency can be further improved by optimizing the geometry of the cavity receiver. Considering the appropriate thermal and mechanical performance of the CHEs, they can be seriously considered for the next generation of high temperature pressurized solar receivers.

## CHAPTER 8 SUMMARY, CONCLUSIONS AND RECOMMENDATIONS

This work investigates the application of s-$CO_2$ power cycles in solar power tower plants. The motivation for this research was to increase the overall efficiency of the power plant by replacing the conventional working and heat transfer fluids with s-$CO_2$. In order to have a full evaluation, all the main components of the power tower plant were individually simulated.

In chapter 2, the procedures for designing and modeling the heliostat field were presented. A simple method was proposed to identify the heliostats with high potential for shadowing and blocking the neighboring heliostats. It is expected that the computational time to be improved by eliminating unnecessary calculations for heliostats that are incapable of shading or blocking. Then, a 50$MW_{th}$ heliostat field was designed for Daggett, CA using the given novel optimization approach.

In chapter 3, an optimization algorithm was introduced to distribute heat flux uniformly on the receiver surface of a power tower plant. An analytical method called HFLCAL was employed to find the heat flux distribution of individual heliostats. The optimization algorithm was developed based on the principles of genetic algorithms. It was shown that the maximum flux density could be reduced by a factor of 10 using an optimization algorithm and finding the best aiming point for each heliostat. It was also demonstrated that the size of the aiming surface has a significant effect on interception efficiency and maximum flux density. Moreover, it was confirmed that increasing the number of aiming points would help to distribute the heat flux more uniformly on the receiver surface.

In chapter 4, a thermal model for a cavity type solar receiver was developed. The correlations for calculating natural and forced convective heat losses were introduced. Also, a detailed radiative heat transfer model was presented. The analytical and numerical methods for finding the view factors between the surfaces were explained and validated against the available data in the literature. Using the equations presented in this chapter, one can simulate the thermal performance of a receiver and find its thermal efficiency.

In chapter 5, different configurations of s-$CO_2$ power cycles were introduced. Then, organic Rankine cycle was employed as a bottoming cycle to improve the efficiency. Different working fluids were examined for the ORC, and the operating conditions were optimized. The combined cycle efficiencies and turbine expansion ratios were compared to find the appropriate working fluids for each s-$CO_2$ configuration. It was shown that including an appropriate bottoming cycle can increase the overall cycle efficiency by 3–7% under the specified conditions. Recompression Brayton cycle showed higher potential to be used as a top cycle providing heat for an ORC bottoming cycle.

In chapter 6, a direct s-$CO_2$ receiver was developed based on the principles of compact heat exchanger technology. The thermal as well as mechanical performance of the receiver were evaluated. Inconel 625 was selected as the base material because of its low potential for corrosion in s-$CO_2$ environment. The receiver was expected to heat 1 kg/s of s-$CO_2$ from 530 ℃ to 700 ℃ under a solar flux density of 500 $kW/m^2$. The influences of different parameters on the performance of the receiver were evaluated by a parametric analysis. The parametric analysis revealed the existence of conflict among the output parameters. Subsequently, a multi-objective optimization was performed to determine the optimal geometry of the heat exchanger considering the trade-off between objective functions, such as unit thermal resistance and pressure drop. The design variables were hydraulic

diameter, number of layers, and distance between the channels. It was shown that s-$CO_2$ could reach the target temperature under optimized conditions while the maximum temperature of the surface remained below the material limit.

In chapter 7, all the models developed in the previous chapters were applied to assess the performance of a $3MW_{th}$ direct s-$CO_2$ receiver based on CHE technology. The heliostat field was designed, and the heat flux density profile on the receiver surface was obtained. The required size and geometry of the receiver were calculated, and convective and radiative heat transfer models were employed to calculate the bulk fluid and surface temperatures. It was shown that the target temperature for s-CO2 was achieved while the surface temperatures remained below the maximum temperature limits of the materials. The receiver efficiency was obtained as 80%, which is highly promising.

**8.1 Recommendations for Future Research**

The results presented in this dissertation show the high-potential of s-$CO_2$ to be used as the heat transfer and working fluids in a solar power tower plant. The recommendations for future research can be summarized as:

(1) The receiver efficiency can be further improved by optimizing the size and geometry of the cavity. For example, the top and bottom surfaces of the cavity can be designed in a trapezoidal shape to replace the inactive side walls with active panels. Moreover, the depth of the cavity can be optimized to minimize the heat loss. In addition, including a lip mounted on the top of the aperture can reduce the convective heat losses.

(2) Other types of alloys that have resistance to corrosion in the presence of s-$CO_2$ should be investigated for the receiver material and compared with Inconel 625 considered in this study.

(3) Thermal stress, fatigue, and creep analyses need to be done for the CHE receiver.

(4) Other channel shapes such as semi-circular and rectangular can be considered for the CHE and compared with the square-shaped channel considered in this study.

(5) Thermal storage for s-$CO_2$ and its effect on overall efficiency of the power plant is an important topic which requires extensive future studies.

(6) Potential of other bottoming cycles such as supercritical Rankine cycle to further improve the power cycle efficiency needs to be investigated.

## LIST OF REFERENCES


[1] *World energy outlook*. Paris: International Energy Agency, 2012.

[2] *Key world energy statistics*. International Energy Agency, 2012.

[3] "National oceanic and atmosphere administration." [Online]. Available: http://www.esrl.noaa.gov/gmd/ccgg/trends/.

[4] *World in transition towards sustainable energy systems*. German Advisory Council on Global Change (WBGU), 2003.

[5] "Torresol energy." [Online]. Available: http://www.torresolenergy.com/TORRESOL/image-library/en?initdate=&enddate=&categoria=cw4cb8173de9630.

[6] "Fresnel heat systems." [Online]. Available: http://fresnelheatsystems.com/.

[7] "DESERTEC-UK."[Online].Available: www.trec-uk.org.uk/resources/pictures/stills4.html.

[8] *Renewable energy technology characterizations*. Electric Power Research Institute, Inc. and U.S. Department of Energy, 1997.

[9] T. Tsoutsos, V. Gekas, and K. Marketaki, "Technical and economical evaluation of solar thermal power generation," *Renew. Energy*, vol. 28, no. 6, pp. 873–886, May 2003.

[10] I. Llorente García, J. L. Álvarez, and D. Blanco, "Performance model for parabolic trough solar thermal power plants with thermal storage: Comparison to operating plant data," *Sol. Energy*, vol. 85, no. 10, pp. 2443–2460, Oct. 2011.

[11] H. L. Zhang, J. Baeyens, J. Degrève, and G. Cacères, "Concentrated solar power plants: review and design methodology," *Renew. Sustain. Energy Rev.*, vol. 22, pp. 466–481, Jun. 2013.

[12] "Solar two power plant." [Online]. Available: http://www.global-greenhouse-warming.com/solar-central-power-towers.html.

[13] J. Pacheco, "Final test and evaluation results from the solar two project," Albuquerque, NM, 2002.

[14] M. Romero, R. Buck, and J. E. Pacheco, "An update on solar central receiver systems, projects, and technologies," *J. Sol. Energy Eng.*, vol. 124, no. 2, p. 98, 2002.

[15] H. Price, "Assessment of parabolic trough and power tower solar technology cost and performance forecasts," Golden, CO, 2003.

[16] C. Turchi, M. Mehos, C. K. Ho, and G. J. Kolb, "Current and future costs for parabolic trough and power tower systems in the US market," in *SolarPACES*, 2010.

[17] S. A. Wright, T. M. Conboy, and G. E. Rochau, "Overview of supercritical CO2 power cycle development at Sandia National Laboratories," in *Supercritical CO2 Power Cycle Symposium.*, 2011.

[18] G. Musgrove, A. M. Rimpel, and J. C. Wilkes, "Funamentals of supercritical CO2," in *ASME Turbo Expo*, 2013.

[19] C. S. Turchi, "Supercritical CO2 for application in concentrating solar power systems," in *Proceedings of SCCO2 Power Cycle Symposium*, 2009, pp. 1–5.

[20] C. S. Turchi, Z. Ma, T. Neises, and M. Wagner, "Thermodynamic study of advanced supercritical carbon dioxide power cycles for high performance concentrating solar power systems," in *Proceedings of the ASME 2012 6th International Conference on Energy Sustainability ES2012*, 2012.

[21] G. J. Kolb, S. A. Jones, M. W. Donnelly, D. Gorman, R. Thomas, R. Davenport, and R. Lumia, "Heliostat Cost Reduction Study," *SANDIA REPORT, SAND2007-3293*, 2007.

[22] P. Garcia, A. Ferriere, and J.-J. Bezian, "Codes for solar flux calculation dedicated to central receiver," *Sol. Energy*, vol. 82, pp. 189–197, 2008.

[23] B. Belhomme, R. Pitz-Paal, P. Schwarzbözl, and S. Ulmer, "A new fast ray tracing tool for high-precision simulation of heliostat fields," *J. Sol. Energy Eng.*, vol. 131, no. 3, p. 031002, 2009.

[24] C. J. Noone, T. Manuel, and A. Mitsos, "Heliostat field optimization: A new computationally efficient model and biomimetic layout," *Sol. Energy*, vol. 86, pp. 792–803, 2012.

[25] F. J. Collado and J. Gallar, "Campo :Generation of regular heliostat fields," *Renew. Energy*, vol. 46, pp. 49–59, 2012.

[26] D. Y. Goswami, F. Kreith, and J. F. Kreider, *Principles of solar engineering*. Philadelphia: Taylor & Francis, 2000.

[27] "Climatic design information," in *ASHRAE Hanbook of Fundamentals*, Atlanta: American Society of Heating, Refrigerating and Air Conditioning Engineer, 2009.

[28] M. J. Wagner, "Simulation and predictive performance modeling of utility-dcale central receiver system power plants," University of Wisconsin- Madison, 2008.

[29] R. W. H. William B. Stine, *Solar energy fundamentals and design : with computer applications*. Wiley-Interscience, 1985.

[30] M. Schmitz, P. Schwarzbözl, R. Buck, and R. Pitz-Paal, "Assessment of the potential improvement due to multiple apertures in central receiver systems with secondary concentrators," *Sol. Energy*, vol. 80, no. 1, pp. 111–120, Jan. 2006.

[31] F. J. Collado and J. A. Turegano, "Calculation of the annual thermal energy supplied by a defined heliostat field," *Sol. Energy*, vol. 42, no. 2, pp. 149–165, 1989.

[32] F. J. Colldado, A. Gomez, and J. A. Turegano, "An analytic function for the flux density due to sunlight reflected from a heliostat," *Sol. Energy*, vol. 37, no. 3, pp. 215–234, 1986.

[33] P. Schwarzbözl, M. Schmitz, and R. Pitz-paal, "Visual HFLCAL – A software tool for layout and optimization of heliostat fields," in *SolarPACES*, 2009.

[34] F. J. Collado, "One-point fitting of the flux density produced by a heliostat," *Sol. Energy*, vol. 84, pp. 673–684, 2010.

[35] G. Sassi, "Some notes on shadow and blockage effects," *Sol. Energy*, vol. 31, no. 3, pp. 331–333, 1983.

[36] R. Osuna, V. Fernandez, M. Romero, and M. J. Marcos, "PS10, a 10 MW solar tower power plant for southern Spain," in *SolarPACES*, 2000, pp. 13–18.

[37] L. L. Vant-Hull and M. E. Izgon, "Guideline to central receiver system heliostat field optimization," *Adv. Sol. energy*, vol. 15, pp. 1–42.

[38] X. Wei, Z. Lu, W. Yu, and Z. Wang, "A new code for the design and analysis of the heliostat field layout for power tower system," *Sol. Energy*, vol. 84, no. 4, pp. 685–690, Apr. 2010.

[39] H. Zhang, I. Juchlia, and D. Favrata, "Multi-objective thermo-economic optimisation of the design of heliostat field of solar tower power plants," in *Engineering for Sustainable Energy in Developing Countries*, 2007.

[40] B. L. Kistler, *A User's manual for DELSOL3: A computer code for calculating the optical performance and optimal system design for solar thermal central receiver plants*. Sandia National Labs, Albuquerque, NM. SAND86-8018, 1986.

[41] K. Atashkari, N. Nariman-Zadeh, A. Pilechi, A. Jamali, and X. Yao, "Thermodynamic Pareto optimization of turbojet engines using multi-objective genetic algorithms," *Int. J. Therm. Sci.*, vol. 44, pp. 1061–1071, 2005.

[42] C. Coello, G. Lamont, and D. Van Veldhuisen, *Evolutionary algorithms for solving multi-objective problems*. Springer, 2007.

[43] C. Winter, R. Sizmann, and L. Vant-Hull, *Solar power plants*. Berlin: Springer, 1991.

[44] A. Salomé, F. Chhel, G. Flamant, A. Ferrière, and F. Thiery, "Control of the flux distribution on a solar tower receiver using an optimized aiming point strategy: Application to THEMIS solar tower," *Sol. Energy*, Mar. 2013.

[45] F. J. GarcÍa-MartÍn, M. Berenguel, a. Valverde, and E. F. Camacho, "Heuristic knowledge-based heliostat field control for the optimization of the temperature distribution in a volumetric receiver," *Sol. Energy*, vol. 66, no. 5, pp. 355–369, Aug. 1999.

[46] G. Renner and A. Ekárt, "Genetic algorithms in computer aided design," *Comput. Des.*, vol. 35, no. 8, pp. 709–726, Jul. 2003.

[47] N. Sharma, Varun, and Siddhartha, "Stochastic techniques used for optimization in solar systems: A review," *Renew. Sustain. Energy Rev.*, vol. 16, no. 3, pp. 1399–1411, Apr. 2012.

[48] Varun and Siddhartha, "Thermal performance optimization of a flat plate solar air heater using genetic algorithm," *Appl. Energy*, vol. 87, no. 5, pp. 1793–1799, May 2010.

[49] M. Loomans and H. Visser, "Application of the genetic algorithm for optimisation of large solar hot water systems," *Sol. Energy*, vol. 72, no. 5, pp. 427–439, May 2002.

[50] A. A. Godarzi, M. Jalilian, J. Samimi, A. Jokar, and M. A. Vesaghi, "Design of a PCM storage system for a solar absorption chiller based on exergoeconomic analysis and genetic algorithm," *Int. J. Refrig.*, vol. 36, no. 1, pp. 88–101, Jan. 2013.

[51] S. a. Kalogirou, "Optimization of solar systems using artificial neural-networks and genetic algorithms," *Appl. Energy*, vol. 77, no. 4, pp. 383–405, Apr. 2004.

[52] a. Baghernejad and M. Yaghoubi, "Exergoeconomic analysis and optimization of an Integrated Solar Combined Cycle System (ISCCS) using genetic algorithm," *Energy Convers. Manag.*, vol. 52, no. 5, pp. 2193–2203, May 2011.

[53] M. H. Ahmadi, A. H. Mohammadi, S. Dehghani, and M. a. Barranco-Jiménez, "Multi-objective thermodynamic-based optimization of output power of Solar Dish-Stirling engine by implementing an evolutionary algorithm," *Energy Convers. Manag.*, vol. 75, pp. 438–445, Nov. 2013.

[54] J. M. Cabello, J. M. Cejudo, M. Luque, F. Ruiz, K. Deb, and R. Tewari, "Optimization of the size of a solar thermal electricity plant by means of genetic algorithms," *Renew. Energy*, vol. 36, no. 11, pp. 3146–3153, Nov. 2011.

[55] T. Wendelin, "SOLTRACE a new optical modeling tool for concentrating solar optics," in *International Solar Energy Conference*, 2003, pp. 253–260.

[56] E. A. Igel, R. L. Hughes, and S. Laboratories, "Optical analysis of solar facility heliostats," *Sol. Energy*, vol. 22, pp. 283–295, 1979.

[57] S. N. Sivanandam and S. N. Deepa, *Introduction to genetic algorithms*. Springer, 2007.

[58] *MATLAB*. The MathWorks Inc., 2012.

[59] C. K. Ho and B. D. Iverson, "Review of high-temperature central receiver designs for concentrating solar power," *Renew. Sustain. Energy Rev.*, vol. 29, pp. 835–846, Jan. 2014.

[60] A. M. Clausing, "An analysis of convective losses from cavity solar central receivers," *Sol. Energy*, vol. 27, no. 4, pp. 295–300, Jan. 1981.

[61] A. M. Clausing, "Convective losses from cavity receivers-comparisons between analytical predictions and experimental results," *Sol. energy Eng.*, vol. 105, pp. 29–33, 1983.

[62] S. H. Teichel, L. Feierabend, S. a. Klein, and D. T. Reindl, "An alternative method for calculation of semi-gray radiation heat transfer in solar central cavity receivers," *Sol. Energy*, vol. 86, no. 6, pp. 1899–1909, Jun. 2012.

[63] F. P. Incropera, *Fundamentals of heat and mass transfer*. John Wiley & Sons, 2011.

[64] D. L. Siebers and J. S. Kraabel, *Estimating convective energy losses from solar central receivers*. Livermore: Sandia National Laboratory, 1984.

[65] S. H. Teichel, "Modeling and calculation of heat transfer relationships for concentrated solar power receivers," University of Wisconsin-Madison, 2011.

[66] W. M. Kays and M. . Crawford, *Convective heat and mass transfer*, 2nd editio. McGraw-Hill, 1980.

[67] G. F. Nellis and S. A. Klein, *Heat transfer*. Cambridge University Press, 2009.

[68] S. A. Klein, *TRNSYS 17: a transient system simulation program*. Solar Energy Laboratory, University of Wisconsin, Madison, USA, 2010.

[69] J. R. Siegel, R., & Howell, *A catalog of radiation heat transfer configuration factors. In R. Siegel, & J. R. Howell, thermal radiation heat transfer*. New York: Taylor and Francis, 2001.

[70] U. Gross, M. Spindler, E. Hahne, and W. Germany, "Shape factor equations for radiation heat transfer between plane rectangular surfaces of arbitary position and size with parallel boundaries," *Lett. heat ad mass Transf.*, vol. 8, no. c, pp. 219–227, 1981.

[71] L. Feierabend, “Thermal model development and simulation of cavity-type solar central receiver systems,” University of Wisconsin-Madison, 2009.

[72] S. H. Teichel, “Modeling and calculation of heat transfer relationships for concentrated solar power receivers,” University of Wisconsin- Madison, 2011.

[73] R. Pitz-Paala, J. Morhenne, and M. Fiebig, “A new concept of a selective solar receiver for high temperature applications,” *Sol. energr Mater.*, vol. 24, no. 1, pp. 293–306, 1991.

[74] E. G. Feher, “Supercritical thermodynamic power cycle,” in *Proceeding of the IECEC, Florida*, 1967.

[75] G. Angelino, “Perspectives for the liquid phase compression gas turbine,” *J. Eng. Power*, vol. 89, no. Trans. ASME, pp. 229–237, 1967.

[76] G. Angelino, “Carbon dioxide condensation cycles for power production,” *J. Eng. Power*, vol. 90, pp. 287–295, 1968.

[77] G. Angelino, “Real gas effects in carbon dioxide cycles,” *ASME Pap. No. 69-GT-103,*, Jan. 1969.

[78] V. DOSTAL, P. HEJZLAR, and M. J. DRISCOLL, “The supercritical carbon dioxide power cycle : Comparison to other advanced power cycles,” *Nucl. Technol.*, vol. 154, no. 3, pp. 283–301.

[79] J. Sarkar, “Second law analysis of supercritical CO2 recompression Brayton cycle,” *Energy*, vol. 34, no. 9, pp. 1172–1178, Sep. 2009.

[80] J. Sarkar and S. Bhattacharyya, “Optimization of recompression S-CO2 power cycle with reheating,” *Energy Convers. Manag.*, vol. 50, no. 8, pp. 1939–1945, Aug. 2009.

[81] A. Moisseytsev and J. J. Sienicki, “Investigation of alternative layouts for the supercritical carbon dioxide Brayton cycle for a sodium-cooled fast reactor,” *Nucl. Eng. Des.*, vol. 239, no. 7, pp. 1362–1371, Jul. 2009.

[82] W. S. Jeong, J. I. Lee, and Y. H. Jeong, “Potential improvements of supercritical recompression CO2 Brayton cycle by mixing other gases for power conversion system of a SFR,” *Nucl. Eng. Des.*, vol. 241, no. 6, pp. 2128–2137, Jun. 2011.

[83] “SunShot Initiative - EERE - U.S. Department of Energy.” [Online]. Available: www1.eere.energy.gov/solar/sunshot/.

[84] E. W. Lemmon, M. O. Mclinden, and M. L. Huber, “NIST Reference Fluid Thermodynamic and Transport Properties — REFPROP, NIST standard reference database 23,” 2013.

[85] V. Dostal, “A supercritical carbon dioxide cycle for next generation nuclear reactors,” Massachusetts Institute of Technology (MIT), 2004.

[86] M. Kulhánek and V. Dostal, “Supercritical carbon dioxide cycles thermodynamic analysis and comparison,” in *Supercritical CO2 Power Cycle Symposium*, 2011.

[87] G. Demirkaya, S. Besarati, R. Vasquez Padilla, A. Ramos Archibold, D. Y. Goswami, M. M. Rahman, and E. L. Stefanakos, “Multi-objective optimization of a combined power and cooling cycle for low-grade and mid-grade heat sources,” *J. Energy Resour. Technol.*, vol. 134, no. 3, p. 032002, 2012.

[88] S. K. W. T. C. Hung, T. Y. Shai, “A review of organic Rankie cycles (ORCs) for the recovery of low-grade waste heat,” *Energy*, vol. 22, no. 7, pp. 661–667, 1997.

[89] R. Chacartegui, J. M. Muñoz de Escalona, D. Sánchez, B. Monje, and T. Sánchez, “Alternative cycles based on carbon dioxide for central receiver solar power plants,” *Appl. Therm. Eng.*, vol. 31, no. 5, pp. 872–879, Apr. 2011.

[90] D. Sánchez, B. M. Brenes, J. M. M. De Escalona, and R. Chacartegui, “Non-conventional combined cycle for intermediate temperature systems,” *Int. J. energy Res.*, 2012.

[91] H. Chen, D. Y. Goswami, and E. K. Stefanakos, “A review of thermodynamic cycles and working fluids for the conversion of low-grade heat,” *Renew. Sustain. Energy Rev.*, vol. 14, no. 9, pp. 3059–3067, Dec. 2010.

[92] R. Rayegan and Y. X. Tao, “A procedure to select working fluids for Solar Organic Rankine Cycles (ORCs),” *Renew. Energy*, vol. 36, no. 2, pp. 659–670, Feb. 2011.

[93] S. M. Besarati and D. Yogi Goswami, “Analysis of advanced supercritical carbon dioxide power cycles with a bottoming cycle for concentrating solar power applications,” *J. Sol. Energy Eng.*, vol. 136, no. 1, p. 011020, Nov. 2013.

[94] Q. Li, G. Flamant, X. Yuan, P. Neveu, and L. Luo, “Compact heat exchangers: A review and future applications for a new generation of high temperature solar receivers,” *Renew. Sustain. Energy Rev.*, vol. 15, no. 9, pp. 4855–4875, Dec. 2011.

[95] J. . Hesselgreaves, *Compact heat exchangers: Selection, Design and operation*. Access Online via Elsevier, 2001.

[96] R. K. Shah, A. D. Kraus, and D. C. Metzger, *Compact heat exchangers*. Hemisphere Publishing Corporation, 1990.

[97] D. M. Jacobson and G. Humpston, *Principles of brazing*. ASM International, 2005.

[98] M. Vrinat, “Development of a High Temperature Air Solar Receiver based on Compact Heat Exchanger Technology,” University of Perpignan, France, 2010.

[99] M. Vrinat, A. Ferrière, P. Mercier, and F. Pra, "Development of a high temperature air solar receiver based on compact heat exchanger technology," in *Proceedings of the 14th SolarPaces Symposium*, 2008.

[100] B. Grange, A. Ferrière, D. Bellard, M. Vrinat, R. Couturier, F. Pra, and Y. Fan, "Thermal performances of a high temperature air solar absorber based on compact heat exchange technology," *J. Sol. Energy Eng.*, vol. 133, no. 3, p. 031004, 2011.

[101] Q. Li, N. G. De Tourville, I. Yadroitsev, X. Yuan, and G. Flamant, "Micro-channel pressurized-air solar receiver based on compact heat exchanger concept," *Sol. Energy*, vol. 91, pp. 186–195, May 2013.

[102] N. Lei, A. Ortega, and R. Vaidyanathan, "Modeling and optimization of multilayer minichannel heat sinks in single-phase flow," in *ASME InterPACK conference*, 2007, pp. 29–43.

[103] N. Lei, "The thermal characteristics of multilayer minichannel heat sinks in single-phase and two-phase flow," The University of Arizona, 2006.

[104] V. Gnielinski, "New equations for heat and mass transfer in turbulent pipe and channel flow.pdf," *Int. Chem. Eng.*, vol. 16, no. 2, pp. 359–368, 1976.

[105] I. E. Idelchik, *Handbook of hydraulic resistance*. CRC Press, 1994.

[106] V. Firouzdor, K. Sridharan, G. Cao, M. Anderson, and T. R. Allen, "Corrosion of a stainless steel and nickel-based alloys in high temperature supercritical carbon dioxide environment," *Corros. Sci.*, vol. 69, pp. 281–291, Apr. 2013.

[107] J. P. Gibbs, "Corrosion of various engineering alloys in supercritical carbon dioxide," Massachusetts Institute of Technology, 2010.

[108] S. K. Mylavarapu and B. Tech, "Development of compact heat exchangers for very high tempeature gas cooled reactors," Ohio State University, 2008.

[109] J. L. Everhart, *Engineering properties of nickel and nickel alloys*. PLENUM Press, 1971.

[110] "Technical bulletin for Inconel 625." www.specialmetals.com.

[111] R. Le Pierres, D. Southall, and S. Osborne, "Impact of mechanical design issues on printed circuit heat exchangers," in *SCO2 Power Cycle Symposium*, 2011.

[112] "ASME Boiler & Pressure Vessel Code, Section III," 1998.

[113] M. B. Allen and E. L. Isaacson, *Numerical analysis for applied science*. John Wiley & Sons, 2011.

[114] "System Advisor Model V." National Renewable Energy Laboratory, Golden, CO.

[115] J. A. Duffie and W. A. Beckman, *Solar engineering of thermal processes*. John Wiley & Sons, 2013.

**APPENDICES**

## Appendix A. List of Symbols

***Abbreviations***

| | |
|---|---|
| $HTR$ | High temperature recuperator |
| $LTR$ | Low temperature recuperator |
| $mc$ | Main compressor |
| $Pc$ | Precompressor |
| $rc$ | Recompression compressor |

***Symbols***

| | |
|---|---|
| $A$ | Surface area ($m^2$) |
| $A_a$ | Aperture area ($m^2$) |
| $a$ | Channel width ($m$) |
| $a_s$ | Solar azimuth angle (degree) |
| $b$ | Channel height ($m$) |
| $C$ | Loss coefficient |
| $C_p$ | Specific heat ($\frac{J}{kg\ K}$) |
| $\cos rec$ | Incidence cosine of the reflected central ray from the Heliostat on the receiver surface |
| $D$ | Distance between heliostat and the aim point (m) |
| $D_h$ | Hydraulic diameter ($m$) |
| $DH$ | Diagonal of the heliostat (m) |
| $DM$ | Diagonal of the heliostat plus the separation distance (m) |
| $d$ | Square root of the heliostat area (m) |
| $dsep$ | Separation distance between the heliostats (m) |
| $E$ | Joint factor |
| $E_{b,reduced}$ | Reduced blackbody emissive power |
| $F$ | Flux density ($\frac{\mathrm{kW}}{\mathrm{m}^2}$) |
| $F_{ij}$ | View factor between surfaces $i$ and $j$ |
| $F_{max}$ | Maximum flux density ($\frac{\mathrm{kW}}{\mathrm{m}^2}$) |

| | |
|---|---|
| $F_{min}$ | Minimum flux density $(\frac{\mathrm{kW}}{\mathrm{m}^2})$ |
| $\hat{F}_{ij}$ | F-hat parameter between surfaces $i$ and $j$ |
| $f$ | Friction factor |
| $f_d$ | Focal distance (m) |
| $f_{0-\lambda_{step},T}$ | Fraction of radiation in a wavelength band from 0 to $\lambda_{step}$ |
| $H$ | heat exchanger height $(m)$ |
| $H_t$ | Image dimension in tangential plane (m) |
| $h$ | Enthalpy (kJ/kg) |
| $h_c$ | Convective heat transfer coefficient $(\frac{\mathrm{W}}{\mathrm{m}^2\mathrm{K}})$ |
| $h_{fc}$ | Forced convective heat transfer coefficient $(\frac{\mathrm{W}}{\mathrm{m}^2\mathrm{K}})$ |
| $h_{nc}$ | Natural convective heat transfer coefficient $(\frac{\mathrm{W}}{\mathrm{m}^2\mathrm{K}})$ |
| $h_{rad,therm,i,j}$ | Equivalent heat transfer coefficient for thermal radiation between surfaces $i$ and $j$ |
| $h_s$ | Hour angle (degree) |
| $h_{sr}$ | Sunrise hour angle (rad) |
| $h_{ss}$ | Sunset hour angle (rad) |
| $I$ | Extraterrestrial normal irradiance $(\frac{\mathrm{W}}{\mathrm{m}^2})$ |
| $I_{bN}$ | Beam normal radiation $(\frac{\mathrm{W}}{\mathrm{m}^2})$ |
| $I_{ref}$ | Direct solar radiation at noon, March 21 $(\frac{\mathrm{W}}{\mathrm{m}^2})$ |
| $k_s$ | Thermal conductivity $(\frac{\mathrm{W}}{\mathrm{m\,K}})$ |
| $L$ | Latitude (degree) |
| $L_H$ | Length of the heliostat (m) |
| $l_n$ | Unit grid length $(m)$ |
| $m_{ORC}$ | Mass flow rate of ORC (kg/s) |
| $\dot{m}$ | mass flow rate (kg/s) |
| $Nu$ | Nusselt number |
| $\vec{n}$ | The unit normal vector of the heliostat surface |
| $P$ | Pressure (MPa) |

| | |
|---|---|
| $P_c$ | Crossover probability |
| $P_{cr}$ | Critical pressure (MPa) |
| $P_m$ | Mutation probability |
| $P_{mm}$ | Second mutations probability |
| $Pr$ | Prandtl number |
| $Q_{aperture}$ | Convective energy leaving the aperture (W) |
| $Q_{conv}$ | Convective heat loss (W) |
| $Q_{HTF}$ | Thermal energy transfer to the heat transfer fluid (W) |
| $Q_{in}$ | Input heat to the top cycle (kJ/kg) |
| $Q_{rad,loss}$ | Energy lost by radiative heat transfer (W) |
| $Q_{therm,ij}$ | Thermal radiation from surface $i$ to surface $j$ (W) |
| $Q_{net,therm,ij}$ | Net thermal radiation from surface $i$ to surface $j$ (W) |
| $q$ | Heat flux $(W)$ |
| $q^{"}$ | Heat flux density $(\frac{W}{m^2})$ |
| $R_{base}$ | Base conduction thermal resistance (K/W) |
| $R_{b,conv}$ | Base convection thermal resistance (K/W) |
| $R_{cond}$ | Axial conduction thermal resistance (K/W) |
| $R_{wc}$ | Thermal resistance between air and stagnant zone (K/W) |
| $R_{tc}$ | Thermal resistance between air and tube surface (K/W) |
| $R_{w,conv}$ | Wall convection thermal resistance (K/W) |
| $R_{wc}$ | Thermal resistance between air and walls of cavity (K/W) |
| $R_{wall}$ | Wall conduction thermal resistance (K/W) |
| $RR$ | Unit thermal resistance $(\frac{\mathrm{K}}{\mathrm{W\ cm^2}})$ |
| $Re$ | Reynolds number |
| $r_k$ | Polar radius of the kth element of the spiral pattern (m) |
| $r_p$ | Cycle pressure ratio |
| $r_{pp}$ | Intermediate pressure ratio |
| $S$ | Design stress $(MPa)$ |
| $S_m$ | Membrane stress $(MPa)$ |

| | |
|---|---|
| $S_T$ | Total stress $(MPa)$ |
| $\vec{S}$ | The unit vector from the center of the heliostat pointing to the sun |
| $T$ | Temperature (℃) |
| $T_{bulk,f}$ | Bulk fluid temperature $(K)$ |
| $T_c$ | Temperature of the air leaving cavity (℃) |
| $T_w$ | Temperature of the wall (℃) |
| $T_{cr}$ | Critical temperature (℃) |
| $T_{f,in}$ | Inlet fluid temperature$(K)$ |
| $T_j$ | Junction temperature $(K)$ |
| $T_s$ | Surface temperature $(K)$ |
| $T_\infty$ | Ambient temperature (℃) |
| $\overline{T_s}$ | Average surface temperature $(K)$ |
| $T_{tmax}$ | Maximum operating temperature of the ORC (℃) |
| $T_{3R}$ | Maximum operating temperature of the ORC (℃) |
| $t$ | Base thickness $(m)$ |
| $t_p$ | Plate thickness (m) |
| $t_f$ | Distance between the adjacent channels $(m)$ |
| $\vec{t}$ | The unit vector from the center of the heliostat pointing to the tower |
| $V$ | Mean fluid velocity (m/s) |
| $V_a$ | Average velocity of mass flux (m/s) |
| $V_b$ | Characteristic velocity due to buoyancy (m/s) |
| $\dot{V}$ | Volumetric flow rate ($m^3$/s ) |
| $W_H$ | Width of the heliostat (m) |
| $W_{hx}$ | Heat exchanger width $(m)$ |
| $W_{net}$ | Net power generated (kJ/kg) |
| $W_s$ | Image dimension in Sagittal plane (m) |

***Greek letters***

| | |
|---|---|
| $\phi$ | ORC Turbine expansion ratio |

| | |
|---|---|
| $\varepsilon$ | Heat exchanger effectiveness |
| $\varepsilon_i$ | Emissivity of surface $i$ |
| $\alpha$ | Solar altitude angle (degree) |
| $\alpha_i$ | Absorptivity of surface $i$ |
| $\tau_i$ | Transmissivity of surface $i$ |
| $\rho_i$ | Reflectivity of surface $i$ |
| $\rho$ | fluid density $(\frac{kg}{m^3})$ |
| $\lambda$ | Wavelength $(\mu m)$ |
| $\eta$ | Instantaneous optical efficiency |
| $\varphi$ | Golden ratio $\frac{1+\sqrt{5}}{2} \approx 1.618$ |
| $\beta$ | Volumetric coefficient of expansion (1/K) |
| $\sigma$ | Stefan-Boltzmann constant $\left(\frac{W}{m^2K^4}\right)$ |
| $\eta_{cos}$ | Cosine efficiency |
| $\eta_{att}$ | Atmospheric attenuation efficiency |
| $\eta_{int}$ | Interception efficiency |
| $\eta_{s\&b}$ | Shading and blocking efficiency |
| $\eta_{ref}$ | Reflectivity |
| $\eta_{rec}$ | Receiver thermal efficiency |
| $\eta_{year,W}$ | Yearly insolation weighted efficiency |
| $\eta_{year}$ | Yearly unweighted efficiency |
| $\eta_{combined}$ | Thermal efficiency of the combined cycle |
| $\delta_s$ | Solar declination angle (degree) |
| $\sigma_{ast}$ | Dispersion due to astigmatic effect (mrad) |
| $\sigma_{bq}$ | Dispersion due to mirror slope error (mrad) |
| $\sigma_{HF}$ | Dispersion of the reflected beam (mrad) |
| $\sigma_{sun}$ | Dispersion of sunlight (mrad) |
| $\sigma_s$ | Mirror slope error (mrad) |
| $\sigma_t$ | Dispersion of tracking errors (mrad) |
| $\theta_k$ | Polar angle of the kth element of the spiral pattern (mrad) |

| | |
|---|---|
| $\bar{\Delta}$ | Relative roughness |
| $\alpha_a$ | Channel aspect ratio |

## Appendix B. Copyright Permissions

This is the copyright permission given by Elsevier for use of materials in Chapters 2, 3.

Saeb Besarati <sbesarati@mail.usf.edu>

**RE: Energy Conversion and Management Enquiry: Requesting permission**

**ECM-ELS** <ECM-ELS@elsevier.com> Thu, Jul 24, 2014 at 8:05 AM
To: Saeb Mostaghim Besarati <sbesarati@mail.usf.edu>

Dear Mr. Besarati,

Thank you for your e-mail. This is to inform you that you have permission to use your own article in your dissertation.

Authors can use their articles for a wide range of scholarly, non-commercial purposes. These rights apply for all Elsevier authors who publish their article as either a subscription article or an open access article. We require that all Elsevier authors always include a full acknowledgement and, if appropriate, a link to the final published version hosted on Science Direct.

For more information, please refer to http://www.elsevier.com/journal-authors/author-rights-and-responsibilities

Best regards,
Sumantha

Ms. Sumantha Alagarsamy
Journal Manager-Global Journals Production
Elsevier India (A division of Reed Elsevier India Pvt. Ltd.)
International Tech Park|Crest-12th Floor|Taramani|Chennai 600 113|India
Tel: +91 44 42994634|E-mail: s.alagarsamy@elsevier.com
Line manager E-mail: s.kurup@elsevier.com

-----Original Message-----
From: Elsevier [mailto:stjournalsjhtp@elsevier.com] On Behalf Of Saeb Mostaghim Besarati
Sent: Wednesday, July 23, 2014 6:58 PM
To: ECM-ELS
Subject: Energy Conversion and Management Enquiry: Requesting permission

The following enquiry was sent via the Elsevier website:

-- Sender --
First Name: Saeb
Last Name: Mostaghim Besarati
Email: sbesarati@mail.usf.edu

-- Message --
Dear Dr. Al-Nimr,
My name is Saeb M. Besarati and I am a Ph.D. candidate in the University of South Florida. I have published a paper entitled as “Optimal heliostat aiming strategy for uniform distribution of heat flux on the receiver of a solar power tower plant” in the Journal of Energy Conversion and Management. I am expecting to graduate soon and I am writing my dissertation. According to our university regulations, we can use a paper as a chapter in our dissertation if we have permission from the journal. The permission letter has to be presented in the dissertation. I would be very obliged if you could please provide me with such document. Please let me know if I need to do anything or provide any document.
Best regards
Saeb Besarati

This is the copyright permission given by American Society of Mechanical Engineering (ASME) for use of materials in Chapters 5.

USF

**Saeb Besarati <sbesarati@mail.usf.edu>**

**Requesting pemission**

**Beth Darchi** <DarchiB@asme.org> Fri, Jul 25, 2014 at 2:26 PM
To: Saeb Besarati <sbesarati@mail.usf.edu>

Dear Mr. Besarati:

It is our pleasure to grant you permission to use **all or any part** of the ASME paper "Analysis of Advanced Supercritical Carbon Dioxide Power Cycles With a Bottoming Cycle for Concentrating Solar Power Applications," by Saeb M. Besarati, D. Yogi Goswami, Journal of Solar Energy Engineering, Volume 136(1), 2014, as cited in your letter for inclusion in a dissertation entitled Analysis of advanced supercritical power cycles for concentrating solar power application to be published by University of South Florida.

Permission is granted for the specific use as stated herein and does not permit further use of the materials without proper authorization. Proper attribution must be made to the author(s) of the materials. **PLEASE NOTE:** if any or all of the figures and/or Tables are of another source, permission should be granted from that outside source or include the reference of the original source. ASME does not grant permission for outside source material that may be referenced in the ASME works.

As is customary, we request that you ensure full acknowledgment of this material, the author(s), source and ASME as original publisher. Acknowledgment must be retained on all pages printed and distributed.

Many thanks for your interest in ASME publications.

Sincerely,

ASME
SETTING THE STANDARD

**Beth Darchi**
Publishing Administrator
ASME
2 Park Avenue, 6th Floor
New York, NY 10016-5990
Tel 1.212.591.7700
darchib@asme.org

## ABOUT THE AUTHOR

Saeb M. Besarati was born in Rasht, Iran in September 1982. He earned his Bachelors and Masters Degrees from University of Guilan, Iran. Upon graduation, he started working as a lecturer in the Department of Mechanical Engineering, Azad University of Takestan. In May 2010, he began his doctoral studies in University of South Florida under the guidance of Dr. Yogi Goswami. His doctoral research focused on analysis of supercritical carbon dioxide power cycles for concentrated solar power applications. During his Ph.D. study, he contributed in writing two book chapters and ten technical papers. He has also served as a reviewer for many internationally well-known journals and conferences.